Metal-to-Ceramic Joining Methods To Support Development of Advanced Ceramic-Based CSP Components

Youyang Zhao,[1] Ulysses Alfaro,[1] Rushikesh Magdum,[2] Jeremy Watts,[2] David Lipke,[2] Mehdi Pishahang,[3] Aaron Wells,[4] Zhenzhen Yu[4]

1 National Renewable Energy Laboratory
2 Missouri University of Science and Technology
3 Massachusetts Institute of Technology
4 Colorado School of Mines

NREL is a national laboratory of the U.S. Department of Energy
Office of Energy Efficiency & Renewable Energy
Operated by the Alliance for Sustainable Energy, LLC

This report is available at no cost from the National Renewable Energy Laboratory (NREL) at www.nrel.gov/publications.

Contract No. DE-AC36-08GO28308

Technical Report
NREL/TP- 5700-91035
September 2024

Metal-to-Ceramic Joining Methods To Support Development of Advanced Ceramic-Based CSP Components

Youyang Zhao,[1] Ulysses Alfaro,[1] Rushikesh Magdum,[2] Jeremy Watts,[2] David Lipke,[2] Mehdi Pishahang,[3] Aaron Wells,[4] Zhenzhen Yu[4]

1 National Renewable Energy Laboratory
2 Missouri University of Science and Technology
3 Massachusetts Institute of Technology
4 Colorado School of Mines

Suggested Citation
Zhao, Youyang, Ulyssess Alfaro, Rushikesh Magdum, Jeremy Watts, David Lipke, Mehdi Pishahang, Aaron Wells, and Zhenzhen Yu. 2024. Metal-to-Ceramic Joining Methods To Support Development of Advanced Ceramic-Based CSP Components. Golden, CO: National Renewable Energy Laboratory. NREL/TP-5700-91035. https://www.nrel.gov/docs/fy24osti/91035.pdf.

NREL is a national laboratory of the U.S. Department of Energy
Office of Energy Efficiency & Renewable Energy
Operated by the Alliance for Sustainable Energy, LLC

This report is available at no cost from the National Renewable Energy Laboratory (NREL) at www.nrel.gov/publications.

Contract No. DE-AC36-08GO28308

Technical Report
NREL/TP- 5700-91035
September 2024

National Renewable Energy Laboratory
15013 Denver West Parkway
Golden, CO 80401
303-275-3000 • www.nrel.gov

NOTICE

This work was authored by the National Renewable Energy Laboratory, operated by Alliance for Sustainable Energy, LLC, for the U.S. Department of Energy (DOE) under Contract No. DE-AC36-08GO28308. Funding was provided by the Office of Energy Efficiency and Renewable Energy Solar Energy Technologies Office. The views expressed herein do not necessarily represent the views of the DOE or the U.S. Government.

Final Technical Report

Project Title:	Metal-to-Ceramic Joining Methods To Support Development of Advanced Ceramic-Based CSP Components
Project Period:	10/1/2021–8/31/2024
Submission Date:	9/30/2024
Recipient:	National Renewable Energy Laboratory (NREL)
Address:	15013 Denver West Parkway Golden, CO 80401-3305
Website:	www.nrel.gov/csp
Award Number:	38487
Project Team:	Missouri University of Science and Technology Massachusetts Institute of Technology Colorado School of Mines
Principal Investigator:	Youyang Zhao, Ph.D. Phone: (303) 275-4398 Email: Youyang.Zhao@nrel.gov
Business Contact:	Craig Turchi Phone: (303) 475-4668 Email: Craig.Turchi@nrel.gov
Technology Manager:	Kamala Raghavan
Project Officer:	Christine Bing

List of Acronyms

APS	Advanced Photon Source
BCC	body-centered cubic
C-SiC	carbon-fiber-reinforced silicon carbide
C2M	ceramic-to-metal
CARES	Ceramics Analysis and Reliability Evaluation of Structures
CFD	computational fluid dynamics
CMC	ceramic matrix composite
CSM	Colorado School of Mines
CSP	concentrating solar power
CTE	coefficient of thermal expansion
DOE	U.S. Department of Energy
DSC	differential scanning calorimetry
EDS	energy dispersive spectrometry
FCC	face-centered cubic
FEA	finite element analysis
FIB	focused ion beam
Gen3	Generation 3
HTF	heat transfer fluid
IPA	isopropyl alcohol
MIT	Massachusetts Institute of Technology
MMC	metal matrix composite
MOS	metal-oxide-semiconductor
MPEA	multi-principal element alloy
MS&T	Missouri University of Science and Technology
NB-SiC	nitride-bonded silicon carbide
NREL	National Renewable Energy Laboratory
PARC	Palo Alto Research Center
RE	rare earth
S-SiC	sintered silicon carbide
SiC_f-SiC	SiC-fiber-reinforced SiC
SAY	SiO_2-Al_2O_3-Y_2O_3 glass ceramic
sCO_2	supercritical carbon dioxide
SEM	scanning electron microscopy
SiC	silicon carbide
SNL	Sandia National Laboratories
SPS	spark plasma sintering
STEM	scanning transmission electron microscopy
TEM	transmission electron microscope
TiC	titanium carbide
UC Davis	University of California, Davis
WC	tungsten carbide
XRD	X-ray diffraction
XRF	X-ray fluorescence
YAG	$3Y_2O_3 \cdot 5Al_2O_3$
YAM	$2Y_2O_3 \cdot Al_2O_3$

YAP	$3Y_2O_3 \cdot 5Al_2O_3$

Executive Summary

Successful implementation of a ceramic-based CSP component aims to take advantage of the ceramic's superior materials properties in a harsh operating environment to avoid critical failure of a CSP plant. Achieving the synergy between using ceramic components and metal HTF transfer networks will rely heavily on the connecting points, where the mechanical, thermal, and chemical stabilities of the ceramic-to-metal joints are critical. However, despite certain successes, prior work (see Background Section 1.1) has shown that the joint between two drastically different materials is the weakest link because of their intrinsically different bonding natures. To the best of the authors' knowledge, the strategy to join advanced ceramic components to the metal-based HTF network is not clearly mapped out. This lack of knowledge could undermine the investment in ceramic components. Therefore, this project aims to bridge the knowledge gaps for making a reliable ceramic-to-metal joint and eventually de-risk Gen3 CSP technology by enabling the use of an advanced ceramic component.

The National Renewable Energy Laboratory (NREL), Missouri University of Science and Technology (MS&T), Massachusetts Institute of Technology (MIT), and Colorado School of Mines (CSM) collaborated to design, develop, and test a material concept at bench scale that will be used to achieve a ceramic-to-metal (C2M) joint between a selected metal HTF loop material and a selected ceramic material used by the Gen3 CSP technology pathway. The final joint assembly will need to have sufficient mechanical properties to withstand static high-temperature (650°C–700°C), high-pressure (20 MPa), and thermal cycling (between 650°C and 100°C) conditions. The material concept consists of three key components, as shown by Figure ES1: (1) a ceramic matrix composite (CMC) that serves as a compliant transition material aiming to mitigate the stresses due to the mismatch of coefficient of thermal expansion (CTE) at a direct ceramic-to-metal joint, (2) a metal end joint using a multi-principal element alloy (MPEA) with a changing percentage of particle loading to bond the candidate metal to the CMC, and (3) a ceramic end joint using a glass ceramic to bond the candidate ceramic to the CMC.

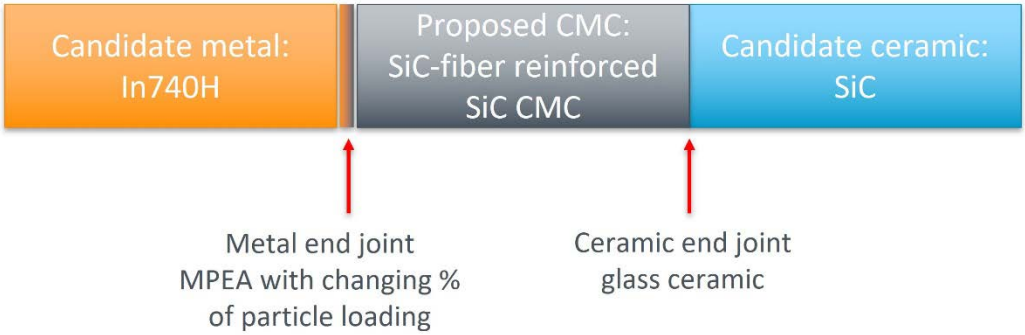

Figure ES1. Schematic of the ceramic-to-metal (C2M) joint concept

The project team selected SiC as the candidate ceramic and Inconel 740H (In740H) as the candidate metal for further experimental investigations, as SiC and In740H are considered to be promising materials for CSP components. SiC-fiber-reinforced SiC CMC was proposed as the transition between the In740H and SiC because of its chemical similarity to SiC, relative technical maturity, and commercial availability.

CSM experimentally investigated various MPEA compositions for bonding between SiC and In740H. A composition of Ti-Mn-Fe-Ni-Cu MPEA was discovered by a computational method. This composition exhibited the highest potential where chemical bonding behavior was observed experimentally between SiC and In740H. However, cracks on the SiC substrate were also discovered, suggesting that stress relief mechanisms are needed. Subsequently, a metal matrix composite (MMC) composed of the MPEA and inert carbide particles (e.g., WC and TiC) was investigated to mitigate the CTE mismatch. This showed improvement, as the inert carbide particles with lower CTE than the MPEA reduce the overall CTE mismatch between the MMC and SiC.

NREL and MS&T experimentally investigated various glass ceramic compositions for bonding SiC to SiC as well as bonding SiC to SiC CMC. An SiO_2-Al_2O_3-Y_2O_3 (SAY) glass ceramic near the eutectic composition was studied extensively; various surface treatments on the SiC and the joint's processing conditions were studied. Over 100 MPa of shear strength was measured for the SAY glass ceramic, and high-temperature hermiticity at up to 900°C was demonstrated at over 4 atm.

Unfortunately, the experimental campaign was not able to continue to the stage of demonstrating the joint concept due to DOE's decision to terminate the funding for the project after August 2024.

Table of Contents

List of Figures

List of Tables

1 Introduction

1.1 Background

Metals and alloys are used frequently by various industries, including concentrating solar power (CSP), for a few reasons. First, metals are generally ductile. When over-stressed, the mechanical failure is often gradual, making metals straightforward to monitor and replace during routine maintenance. Second, metals can be welded/brazed, meaning that localized heating can melt them to form bonds, even between different metals. These traits make it easy to bond and seal metal parts in the field. Third, metals are strong at temperatures well below their melting point. This means that their mechanical properties can be used to form systems that can support the weight of themselves and other components. Fourth, many metals are affordable. Their affordability is especially important for large-scale applications such as CSP. Fifth, metals are formable into complex shapes via casting and machining. Finally, some metals can be oxidation resistant via formation of surface passivation. Therefore, for each of the three candidate Generation 3 (Gen3) CSP pathways—liquid (molten chloride salt and molten sodium), solid (oxide particles), and gas (sCO_2)—metal-based components form the majority of the subsystems of the plant, i.e., the transfer network for the heat transfer fluids (HTFs).[1]

On the other hand, ceramics are also popular engineering materials for specialized applications, for a few reasons. First, ceramics usually have strong covalent (or ionic) bonds. These stronger bonds lead to better mechanical properties (high Young's modulus, hardness, and strength), thermal stability (high melting point), and chemical stability (more corrosion resistance) in extreme environments. Second, ceramics can be less dense than their metal counterparts that have similar mechanical, thermal, and chemical properties (such as Ni-based alloys and steel alloys). Hence, for weight-sensitive applications, ceramics could be beneficial. Third, ceramics usually have high dielectric constants that are useful for electric insulation. These unique properties can give ceramics an advantage over metal alloys for certain specialized applications. From the CSP perspective, ceramics have the potential to replace their metal counterparts in key components that need to operate under the most extreme conditions (e.g., high-temperature, corrosive, or erosive environments). Therefore, in addition to ongoing research and development efforts on metal-based CSP components, the U.S. Department of Energy (DOE) has invested in projects to simultaneously develop ceramic-based components for the candidate Gen3 CSP technology pathways.[2] Success from these projects will undoubtedly reduce the risks of Gen3 CSP.

A reliable high-temperature ceramic-to-metal (C2M) joint has been a long-time materials challenge. The traditional approach is to select a thin interlayer material (on the order of nanometers to micrometers) to (1) provide additional ductility and compliance to accommodate the stresses from the coefficient of thermal expansion (CTE) difference between the ceramic and

[1] Ceramic-based loop/piping material is possible. However, easy-to-perform, high-temperature ceramic joining method(s) in the field are still lacking. Given the needed quantities and number of joints, metal/alloy piping is much easier to implement.

[2] For example, (1) Argonne National Laboratory developed a MAX-phase solar receiver, (2) Ceramic Tubular Products developed a SiC solar receiver for the liquid pathway, (3) the Massachusetts Institute of Technology developed a ceramic castable cement for thermal energy storage tanks and piping, as well as ceramic pumps and valves for molten salts, (4) Purdue University and Missouri University of Science and Technology developed ceramic heat exchangers, (5) Powdermet developed a cermet-based molten salt pump, and (6) various projects developed ceramic-based coatings, such as by the University of California San Diego.

metal[3] [1] and (2) serve as a diffusion barrier to prevent unwanted reactions that may form brittle intermetallic phases [1]. In the past, the interlayer was typically limited to a few thin homogenous materials (e.g., Ag-Cu-Ti [2], Ni [3–7], Ag [7], Cu [8], Al [9], or Ti [10,11]).

The motivation for the proposed C2M joint approach comes from recent advances in ceramic technologies:

(1) The ability to make a ceramic/metal composite may provide a suitable interlayer chemistry with intermediate properties between the two end materials (e.g., Al_2O_3/Ni [12–17], Al_2O_3/W [18–20], Al_2O_3/Al [21], Al_2O_3/Mo [22–25], SiC/Al [15], TiC/Fe [26], TiB/Ti [27], AlN/Mo [28], or AlN/Al [29]).[4]
(2) Ceramic additive manufacturing (such as extrusion [30–35], 3D printing [35–42], and others [43–46]) may be able to produce a gradual transitioning interlayer.[5] If the interlayer can transition from 100% ceramic to 100% metal, it could eventually enable conventional joining methods to join to similar materials.

These two advances could theoretically reduce the mismatch between the CTEs as well as the residual thermal stresses that are normally responsible for a ceramic-to-metal joint failure. The use of a longer transition material (e.g., a ceramic matrix composite [CMC]) may also act as an additional component of the joint, which, if having sufficient compliance, may also help reduce the overall gradient of the CTE mismatch and the resulting thermal stresses.

1.2 Project Overview

The project consisted of multiple stages of research. The first year was focused on down-selection of the candidate ceramics and metals to be joined, development of the preliminary design concept for the joint, and preliminary chemistry selection for the joining materials. The second year was focused on further development of the joining materials and joining conditions, with extensive mechanical testing at room temperature and hermiticity testing at high temperatures.

The project impacts are primarily twofold. In the near term, successful completion of this project will support and de-risk the Generation 3 (Gen3) concentrating solar power (CSP) technology pathway. In the long term, it will develop a new joining methodology that can be used for other applications under different operating conditions. The project will have a wide-ranging impact on the high-temperature materials research community because it will enable a smoother and easier integration of the two most commonly used high-temperature materials: ceramics and metals. The materials and processing advances will encourage more innovative high-temperature component designs in a wide variety of industries because the concerns over the ceramic-to-metal joints will be less of a design constraint. The impact and merit/applicability of this work can extend beyond the CSP community, or even beyond solar energy technologies in general. Other industries, such as aerospace and nuclear, can also benefit from the successes and lessons learned.

[3] Nonrefractory metals usually have higher CTEs compared to ceramics (i.e., $>10\times10^{-6}$ °C^{-1} for metals and $<10\times10^{-6}$ °C^{-1} for ceramics).
[4] Our preliminary literature review reveals that Al_2O_3 is a major ceramic material of interest to the ceramic/metal composite concept. Among the studies of Al_2O_3, Ni is a major metal material of interest.
[5] Usually called a functionally graded material.

2 Results and Discussion

2.1 Down-Selection of Ceramic and Metal

2.1.1 Materials Framework

NREL consulted with multiple metal and ceramic engineering experts to determine the suitability of a few candidate materials as the end materials of the joint application. These materials are only relevant to the metal piping and ceramic components (not the material of the joint). The goal was to set the materials boundary conditions for the joint. The project team made a down-selection from a few candidate materials that are currently under serious consideration for CSP ceramic heat exchangers, solar receivers, and piping applications. The team gathered information on their temperature-dependent thermal and mechanical properties (e.g., tensile strength, creep and fatigue resistance, CTE), surface chemistry, applicability to reaction bonding, cost/availability, relevance to CSP applications, and so on.

Table 1 lists the candidate materials for ceramic and metal CSP components that are currently under investigation by various industrial, national lab, and academic entities.

Table 1. Summary of the Candidate Metal and Ceramic Materials That Are Under Current Consideration for CSP Applications

Institute	Material(s)	Component(s)
Ceramic Component Developments		
Ceramic Tubular Products	Monolithic SiC and fiber-reinforced SiC composite	Receivers, piping, heat exchangers
Palo Alto Research Center	Fiber-reinforced composite	Receivers, piping
General Electric (GE) Research	Alumina	Coolers
Purdue University	Alumina-matrix composite	Heat exchangers
Argonne National Laboratory	SiC	Piping
Metal Component Developments		
Sandia National Laboratories	In740H, In617, In625	Heat exchanges, piping
Electric Power Research Institute	In740H	Piping
Special Metals	In740H	Piping
University of California, Davis	H282	Heat exchangers

There are two major ceramic materials of interest for the CSP components: (1) SiC and SiC composite and (2) alumina and alumina composite. The interest in these two types of materials is easy to understand, given the amount of knowledge of their physical and mechanical properties, corrosion performance, and manufacturing capabilities.

There are a few major advantages and disadvantages for each type. SiC and SiC composites have competitive mechanical and thermophysical properties at the Gen3 CSP operating temperature range, including high thermal shock resistance; high creep resistance; high strength; high corrosion resistance to molten salt, molten Na, and supercritical CO_2 (sCO_2); high resistance to oxidation; high abrasion resistance to flowing particles; and high thermal conductivity. However, SiC and SiC composites are difficult to manufacture, with long and complex manufacturing processes; they are also difficult to achieve consistent properties from batch to batch and are more expensive to

make. Alumina/alumina composites have high stiffness and creep resistance at high temperatures, enhanced resistance to fracture if in composite form, high erosion resistance, and high resistance to oxidation in air and sCO_2. On the downside, alumina and alumina composites are difficult to fabricate in thin and dense plate form with tailorable patterns.

Given the research performed on the two major ceramic materials, the down-selection is less about the absolute performance advantages that one material has over the other (both materials have a few major benefits compared to metals/alloys) and more about the current development of the material that may enable future deployment. Based on the feedback received from industry and academia, SiC/SiC composites are considered a more promising material to focus on, because a few industrial and national lab players (such as Ceramic Tubular Products, Palo Alto Research Center, and Argonne National Laboratory) have already invested in the development and manufacturing process. Because the proposed joint application needs a feasible ceramic CSP component, we chose to focus on SiC/SiC composite due to its future commercialization potential and deployment possibility.

Feedback on the candidate metal/alloy materials for the HTF piping network was provided by a few research and commercial entities (NREL, Sandia National Laboratories, EPRI, and Special Metals). Similar to the ceramic candidates, a few alloys stood out based on their performance/properties, and the down-selection was mostly based on possibility of future deployment. Two alloys—In740H from Special Metals and H282 from Haynes International—are the most promising because of their superior properties, such as high strength and corrosion/erosion resistance at high temperatures. Other alloys, such as SS304H (good affordability) and In617/In625/Hastelloy C276 (availability of corrosion data), are not considered here because of a combination of limited strength at Gen3 CSP operating temperatures, high cost, long lead time, insufficient supply chain development, and so on.

We did not down-select between In740H and H282 because these two alloys are very similar in composition and strengthening mechanisms. Both are high-Ni alloys with the addition of Al and Ti to form gamma prime precipitates. Their compatibility with ceramic is believed to be similar from a technical feasibility point of view.

2.2 Thermomechanical Simulation of a Simple Butt Joint Design

The project team performed a set of thermomechanical simulations to understand the thermal and mechanical stresses at a simplified butt joint between a SiC piping and an In740H piping, assuming a smooth transition (i.e., no defects) without any joining material. A computational fluid dynamics (CFD) model was set up to simulate the fluid flow and temperature fields, with the initial environment at room temperature and atmospheric pressure. The calculated results were then input into finite element models to calculate the stress/strain contours associated with the sCO_2 flow. Two finite element models were set up with different boundary conditions. The first model (Model 1) was constrained at the SiC pipe end with zero displacement. In contrast, the second model (Model 2) allowed for free span of the pipe; in other words, no constraint was applied at either pipe end. The pipeline was assumed to have a total length of 3.94 inches (10 cm) and an inner diameter of 2 inches (5.08 cm). Based on the literature on In740H pipes [47], we determined that, at the operating temperatures examined in this study (approximately 725°C), the allowable operating stress is approximately 110 MPa. This value was input as σ_h in Equations (1)–(3) for

thick-wall hoop stress (σ_h) calculations. In these equations, p is the sCO_2 gas pressure either inside (i) or outside (o) the pipe, and r is the radius of the internal (i) and outer (o) walls.

$$\sigma_h = A + \frac{B}{r_i^2} \quad (1)$$

$$A = \frac{p_i r_i^2 - p_o r_o^2}{r_o^2 - r_i^2} \quad (2)$$

$$B = \frac{(p_i - p_o) r_o^2 r_i^2}{r_o^2 - r_i^2} \quad (3)$$

Based on the calculations, both the SiC and In740H components need to have the same wall thickness of 0.201 inches (0.51 cm) based on the maximum allowable stress of an In740H pipe in the hoop direction.

To bound the thermal and mechanical cycles, we assumed that there will be two primary fluctuations in operating conditions each day—temperature and flow rate. The temperature was assumed to fluctuate between 620°C and 720°C, and the flow rate of sCO_2 within the pipes was assumed to fluctuate between 30 kg/s and 60 kg/s.[6] These values and fluctuations were based on feedback from sCO_2 power cycle experts from NREL; University of California, Davis (UC Davis); and the Massachusetts Institute of Technology. The fluid was modeled to be flowing from the heat exchanger (or "hot") side to the pipeline (or "cold") side. In the initial models, the assumption is that the fluid comes from inside the heat exchanger, where it has been heated to approximately 720°C, and is pumped into the simulated pipes with a flow rate of 60 kg/s. We calculated the internal pressure and compared it to the expected 20 MPa internal pressure. A schematic of this simulation can be seen in Figure 1. Figure 2 shows the calculated results of the temperature and flow rate fields after flowing the fluid for approximately 10 min. The CFD model is still ongoing to calculate the evolution of these fields at a longer operation time. The internal pressure was calculated to be around 25 MPa, which is close to the expected 20 MPa.

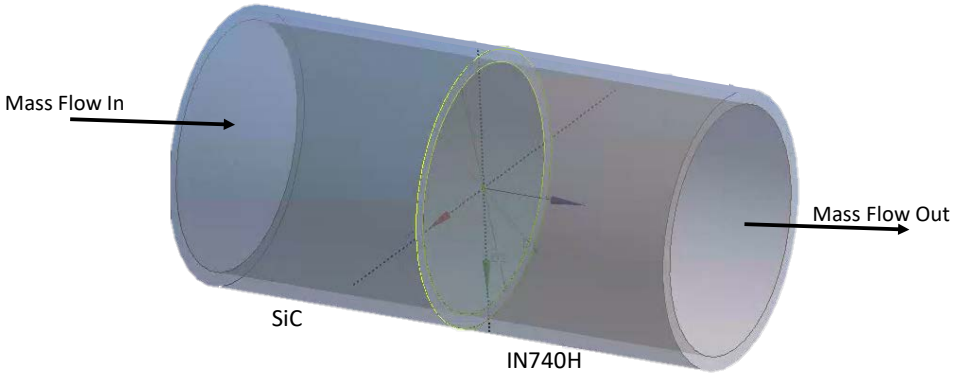

Figure 1. Configuration of the piping system for thermomechanical simulation

[6] The approximate maximum sCO_2 flow rate is about 1,200 kg/s for a 100-MWe power plant. Assuming that such a power plant has roughly 20 primary heat exchangers, the maximum flow rate for each heat exchanger is about 60 kg/s. Assuming the flow is halved at night, the minimum flow rate for each heat exchanger is about 30 kg/s.

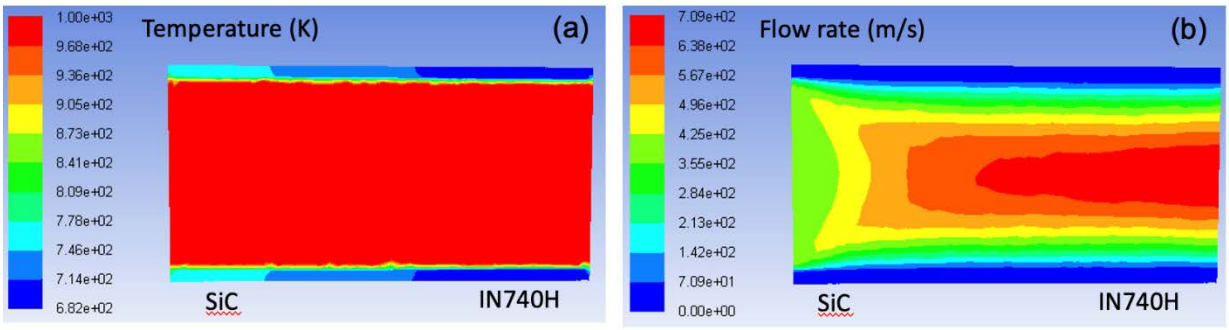

Figure 2. CFD results (2-D transect) of (a) temperature and (b) sCO_2 fluid flow fields after approximately 10 min of flow

With the initial CFD results of temperature and fluid flow as an input (i.e., Figure 3(a)), the finite element models were able to further calculate the stress/strain distributions in the SiC/In740H pipe. In Model 1, we found that the von Mises stress peaked at the fixed end and the joint, as shown in Figure 3(b). This is likely due to the constraint that prevents the free thermal expansion of the materials. We found that the In740H side experienced similar von Mises stress (up to 550 MPa) at the joint interface in the two models with different boundary conditions (compare Figure 3(b) to Figure 3(c)), and the SiC experienced up to 375 MPa von Mises stress near the interface in both models.

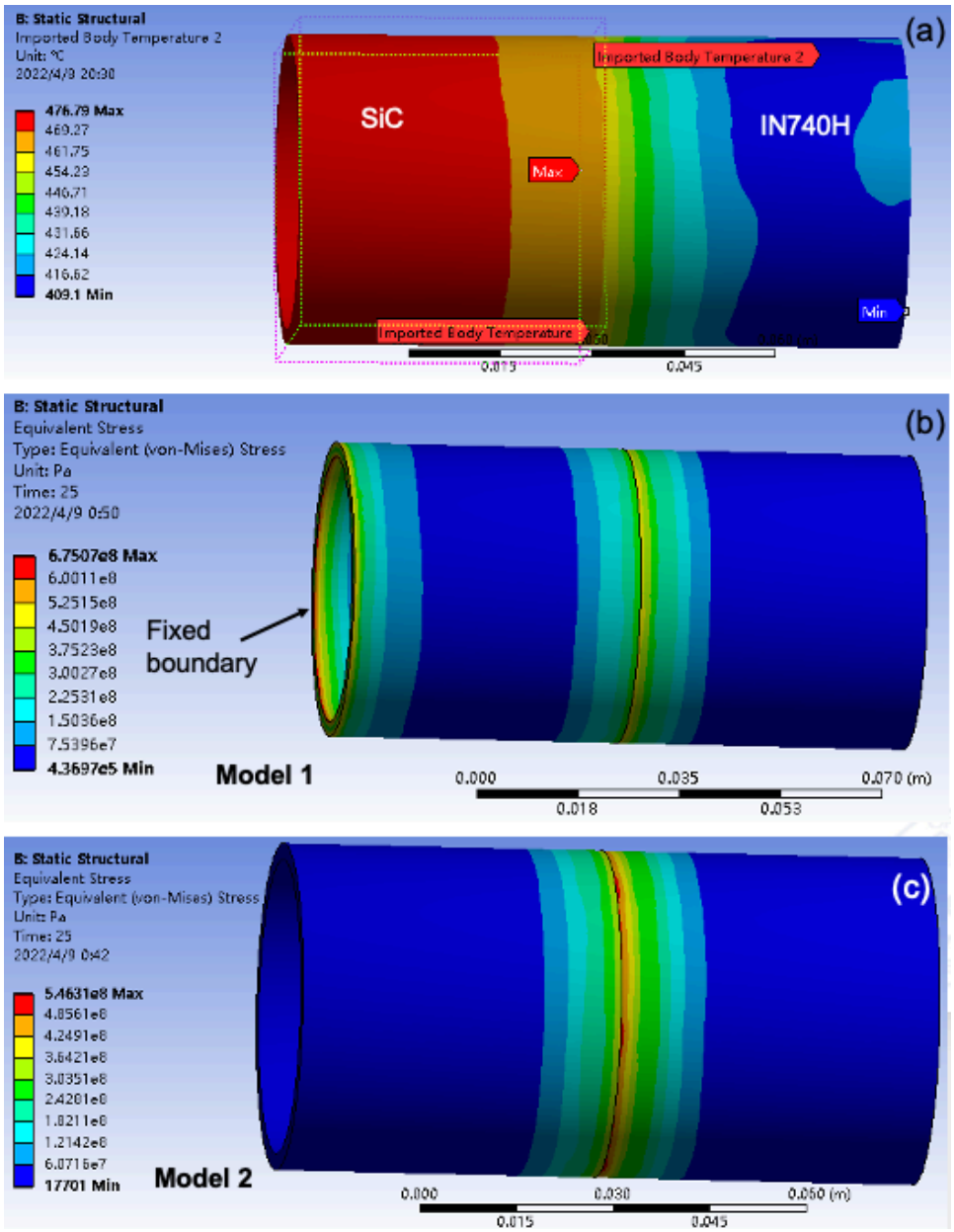

Figure 3. Finite element model results: (a) temperature input from CFD model, and von Mises stress experienced by the SiC/In740H pipe for (b) Model 1 (fixed boundary at the SiC pipe end) and (c) Model 2, which allows for free span

Figure 4 and Figure 5 summarize the stresses calculated along radial (x), hoop (y), and longitudinal (z) directions from Model 1 and Model 2, respectively. At the current flow time (approximately 10 min), without a proper transition joint, the peak stresses experienced by the ceramic and metal sides near the joint interface were similar in both models. The ceramic side near the interface experienced tensile radial and hoop stresses as high as 310 MPa and 410 MPa, respectively, in both Model 1 and Model 2. In comparison, the In740H side experienced high compressive radial and hoop stresses up to 350 MPa and 477 MPa, respectively, in both models. The In740H side experienced a tensile longitudinal stress up to 274 MPa in both models, while the ceramic side experienced a low tensile stress below 100 MPa.

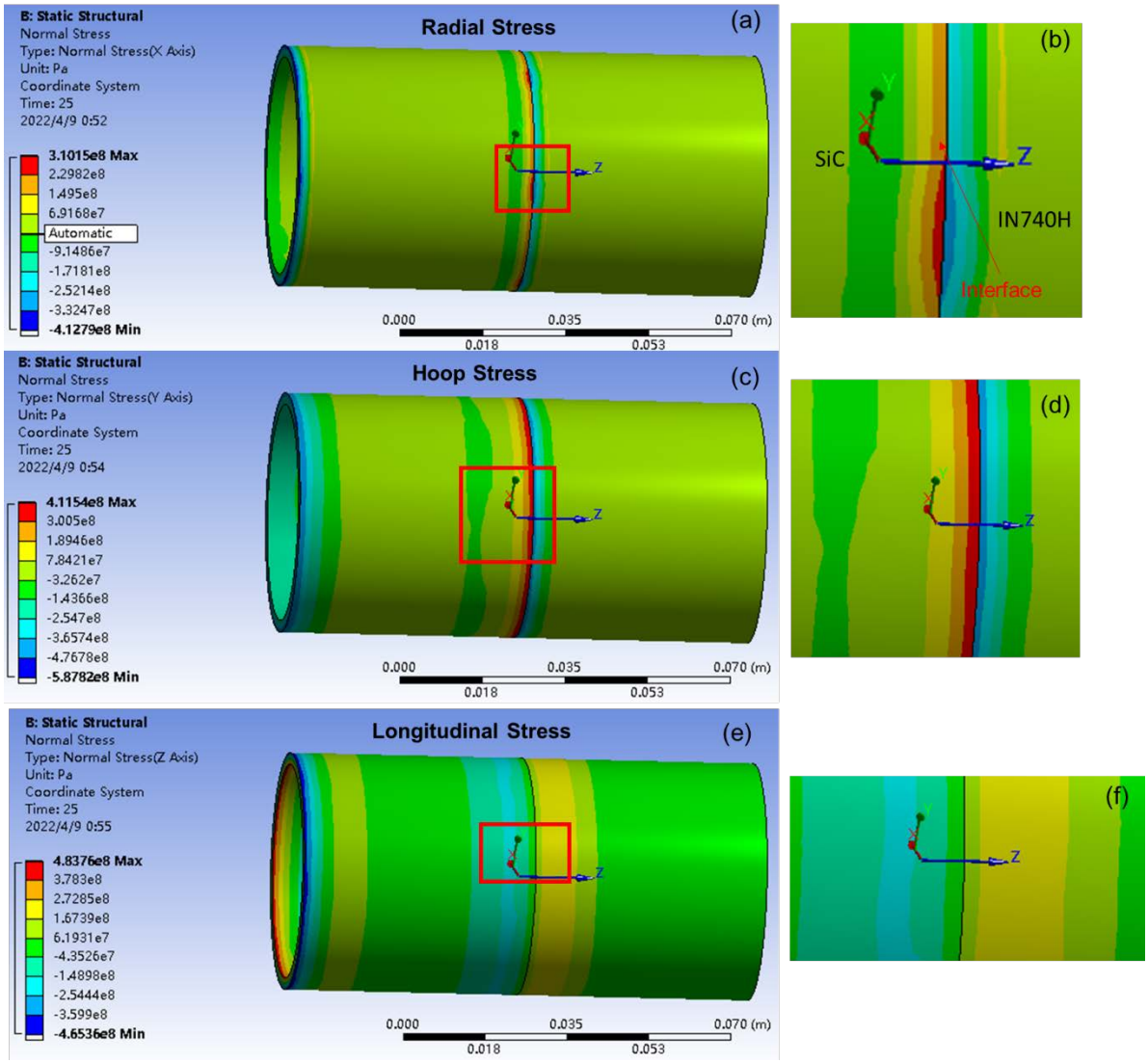

Figure 4. Finite element results for Model 1 (fixed end for SiC pipe). (a–b) radial stress, (c–d) hoop stress, and (e–f) longitudinal stress.

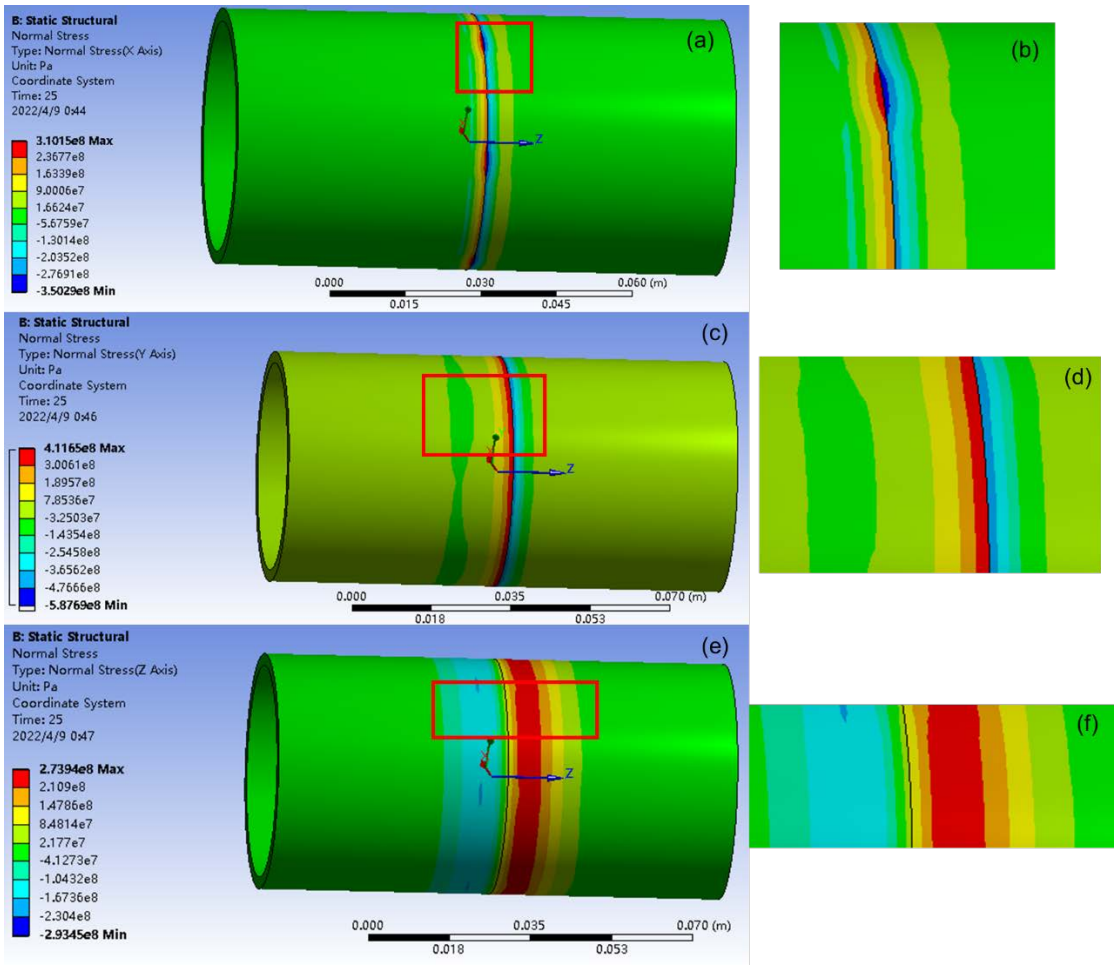

Figure 5. Finite element results for Model 2 (no constraint). (a–b) radial stress, (c–d) hoop stress, and (e–f) longitudinal stress

Both models indicated that the peak stresses at the joint were above the maximum service stress prescribed by the material manufacturer for In740H [47]. In the SiC component, the peak stress was the hoop stress at 82.7% of the fracture strength at the maximum simulated temperature [48]. Note that these values were all calculated only up to 10 min flow time to 409°C on the In740H side. Even at such a low temperature, the thermal expansion was causing concerning stress levels. This confirmed the need for a transition joint that can accommodate the difference in CTEs. The modeling results estimated the stress levels that need to be handled by the joint, thus serving as a design basis for the preliminary joint.

In addition, Figure 6 showed the calculated results of temperature and flow rate fields after flowing the fluid for approximately 10 min. The internal pressure was calculated to be around 25 MPa, close to the expected 20 MPa pressure of an sCO_2 heat exchanger.

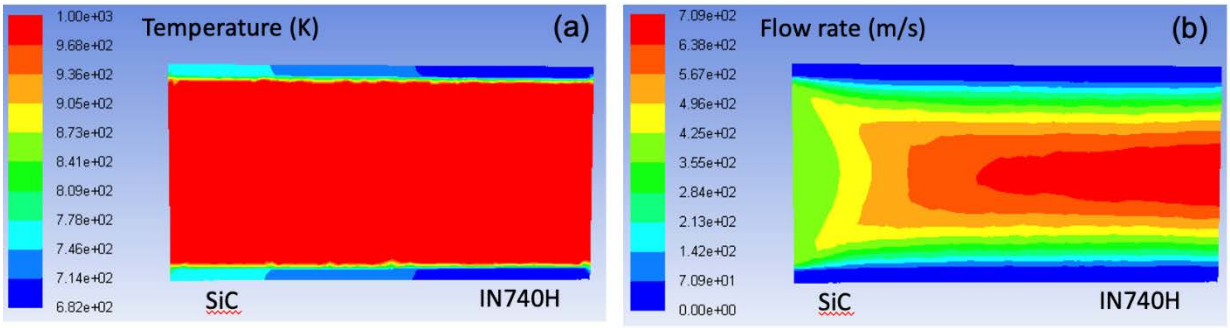

Figure 6. CFD results of (a) temperature and (b) sCO_2 fluid flow fields after flowing the fluid in for approximately 10 min

A key issue that was overlooked by the early simulations was identified in Figure 6(b), where the sCO_2 fluid flow's maximum velocity was over 700 m/s. Apparently, a supersonic sCO_2 gas is outside the expectation, which will lead to other technical issues. In contrast, the average sCO_2 gas velocity inside a prototype 20-kW sCO_2-to-molten-salt heat exchanger made by a research team at UC Davis was only 0.45 m/s, whereas the maximum velocity near the sCO_2 inlet was no more than 2.81 m/s. To scale up, the plan was to add more plates with the same mass flux and speed of sCO_2 instead of increasing the mass flux and velocity. Therefore, going from <5 m/s from inside the channels of a prototype-scale heat exchanger to a supersonic >700 m/s inside the joint area connected to the heat exchanger header was clearly an inappropriate assumption in the initial specifications of the joint, or the simulation settings were wrong.

Therefore, the project team validated the modeling effort shown above by comparing it to a simplified back-of-the-envelope calculation based on gas volume and flow rate. The calculation estimated that 60 kg/s of sCO_2 flow through a 2-inch pipe should yield about 17 m/s of gas velocity. The result indicated that the supersonic 700 m/s velocity from the previous simulation was wrong.

With corrected modeling sittings, Figure 7(a) and Figure 7(b) present the contour plots calculated by the ANSYS Fluent model for the temperature distribution and fluid flow inside the dissimilar butt joint from SiC to In740H, respectively. Figure 7(a) shows that an overall pipe temperature equal to 720°C (993.15 K) was achieved. Figure 7(b) shows that the peak output flow velocity was equivalent to 31 m/s, which is on a similar order of magnitude as the 17 m/s calculated manually with a simplified model. It also fell into a much more reasonable velocity range of 10–50 m/s, given the general knowledge of fluid dynamics and sCO_2 power cycles. The internal pipe pressure associated with the sCO_2 flow was about 18.9 MPa. The results showed that with the current assumption of joint dimensions and flow rate, the sCO_2 gas would achieve a reasonable velocity. If the 31 m/s speed were still unacceptable, we would further modify the joint design. For example, the assumed total flow rate for each heat exchanger was between 30 kg/s and 60 kg/s, based on a known target of 1,200 kg/s of total sCO_2 flow for a 100-MW_e power plant. For each 100-MW_e power plant, there will likely be >20 primary heat exchangers to achieve an estimated power density of 5–10 MW_e/m^3. For 60 kg/s of sCO_2 to flow through a 2-inch joint pipe (assuming each ceramic heat exchanger is equipped with only one C2M joint), the required flow speed of sCO_2 will reach a maximum of about 30 m/s. To further reduce sCO_2 velocity and mass flux, increasing pipe dimension would help. However, to reduce overall hoop stress due to internal pipe pressurization, increasing the joint pipe size is not the preferred method, because hoop stress

increases with pipe size. Hence, the more logical solution is to reduce the total flow rate of sCO_2 through the joint pipe, or equivalently, to increase the number of joint pipes for each heat exchanger (i.e., each ceramic heat exchanger would need multiple smaller-diameter joint pipes to manage both the hoop stresses on each joint pipe and the flow rate or flow speed of sCO_2). The project team had to make such an assumption because there was little public information about the specifications of a commercial-scale ceramic-based sCO_2 heat exchanger. The team continued the project with its own specifications for the C2M joint based on expected stresses and other constraints around the joint area.

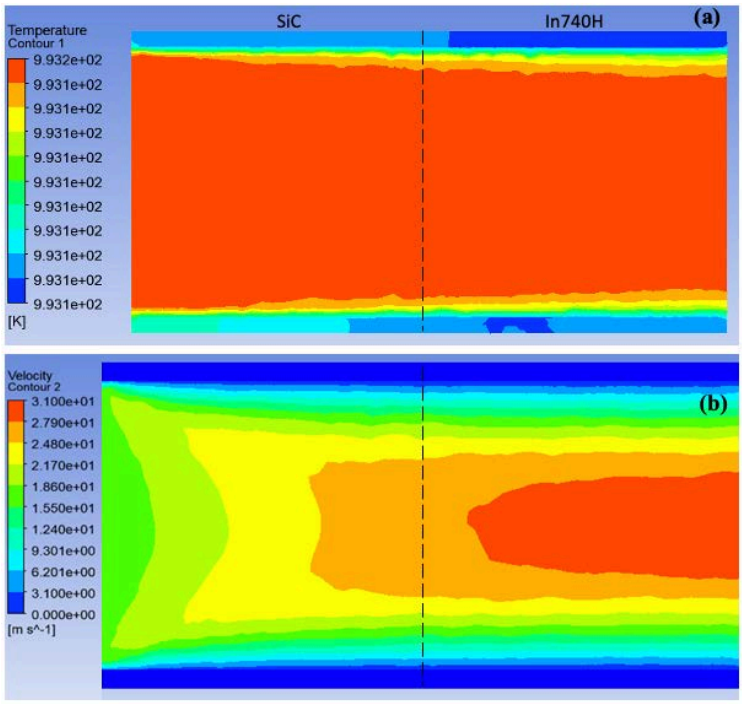

Figure 7. ANSYS Fluent model contour plots presenting (a) the temperature distribution in the pipeline and (b) the sCO_2 flow rate inside the pipe

Another important implication of the modeling results is that for a reliable design, it is no longer the reported ultimate strength of the material that matters most. Instead, the distribution of the material's strength given a certain manufacturing method is also critically relevant. One of the methods to address the variance of the strength is to calculate the maximum allowable stress using the Weibull model. For example, for a material with a reported strength σ_0 and a Weibull modulus m, the maximum allowable stress at a certain probability of failure is given by Figure 8. The quantity V^* is the ratio of the effective volume of the part under tensile load to the effective volume of the standard geometry used to measure strength (e.g., a four-point bend bar). To find V^*, one needs to compute the effective volumes by integrating the quantity of (principal tensile stress of the element/maximum principal tensile stress)^m, where m is the Weibull modulus over all elements in the model. Some finite element analysis (FEA) programs have such capability, but the Ceramics Analysis and Reliability Evaluation of Structures (CARES) program[7] is an industry standard for this purpose. CARES can take the mechanical stress analysis as an input to evaluate this integral.

[7] http://www.ceramicreliability.com/software/cares.html

To make a meaningful comparison for the ratio, this calculation should be repeated for a model of the four-point bend test condition with similar mesh size.

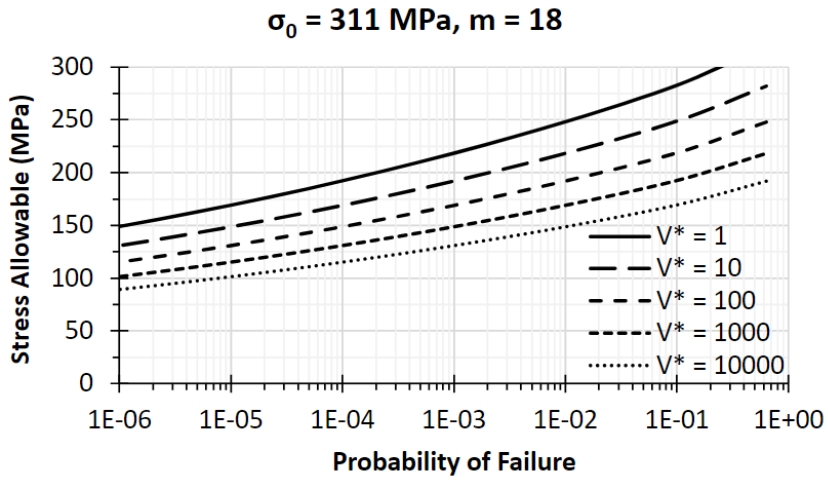

Figure 8. An example Weibull distribution between the maximum allowable stress and the probability of failure at different ratios *V

2.3 Selection of Candidate Joining Chemistries and Joint Designs

The candidate materials to achieve the SiC-to-In740H joint need to have a chemistry that is compatible with the two end materials. They must also be resistant to creep at the targeted operating temperature. We performed a literature survey to identify potentially feasible chemistries for this purpose.

From the literature survey, we determined that some elements to be included in the potential chemistry design for joining the In740H to the SiC-based CMC via brazing are titanium, chromium, zirconium, and nickel [49–53]. Brazing is of interest because brazes for SiC are most effective when they contain carbide-forming elements that will plastically deform before cracking during cooling. Titanium, chromium, and zirconium are extremely good carbide formers, which improves the brazeability to the SiC. Nickel and titanium have high toughness, and therefore can potentially serve to enhance the ability of the braze to absorb the stress induced by the difference in CTEs. Elements like gold and silver provide great wetting, ductility, and bonding, but fail to provide good strength at high temperatures because of their low melting points [54]. Brazes for In740H, if used, are likely to benefit from the inclusion of iron, chromium, and nickel [49,52,54]. These elements aid in In740H brazing because they help break down the passive oxide layer that forms on the surface of the Inconel alloy, as well as being alloying elements themselves in In740H. Breaking down the oxide layer is one of the primary stages of wetting found in successful brazing of nickel superalloys.

For joining the SiC-based CMC to the SiC end, we consider glass ceramics. Based on a review by Liu et al. [55], oxide glass ceramic systems made of a rare-earth oxide (e.g., Y_2O_3), Al_2O_3, and SiO_2 at various compositions are promising. Depending on processing temperature, joining has been reported using a binary Y_2O_3 and Al_2O_3 glass ceramic at relatively high temperatures of 1,600°C–1,900°C with minor additions of other additives, such as SiO_2 and C [56–61]. When SiO_2 is added as a major constituent, the processing temperature can be significantly lower, at about

1,400°C [62–66]. The lower processing temperature helps prevent the SiC-based CMC from excessive decomposition at >1,400°C, which is a major constraint when selecting the materials and process conditions.

Based on the information gathered, the project team initially suggested several possible design routes to consider for the transition between the SiC and In740H.

1) A monolithic ceramic tube body: This route is easiest to manufacture but is the least reliable. The monolithic ceramic tube needs to have minimal volume under load.
2) A fiber-reinforced composite tube body: This route is most difficult to manufacture but is more reliable than monolithic ceramic. Achieving and maintaining hermiticity may be a significant issue.
3) An array of smaller monolithic ceramic tube bodies: This route has an intermediate manufacturing difficulty and is more reliable than a single (larger) tube body. To achieve this design, hoop stresses should be minimized in each tube body. The size and number of parallel paths in the array will be limited by the allowable pressure drop in the system.
4) A metallic tube with ceramic fiber wound backing: This route has an intermediate manufacturing difficulty and is possibly most reliable, because the metallic tube provides hermiticity and the ceramic fiber backing provides stiffness and creep resistance. However, it would introduce another metal-to-ceramic interface between the metallic tube and the ceramic fiber backing.

These design routes share the same challenges at the metal/ceramic interface, where multiple compliant layers might be necessary to reduce misfit stress. It should be noted that one of the key features of the original conceptual design is a transition tube with a graded composition from metal to ceramic. The chemical grading in the axial direction of the transition tube serves two purposes. First, by using an integral compositional grading, the transition from metal to ceramic is gradual over the tube length and obviates the need for a metal-to-ceramic dissimilar material joint. Second, the thermal-elastic mismatch between the metallic and ceramic end components would theoretically be mitigated by a composite approach to grading the Young's moduli and thermal expansion coefficients in the graded region.

Despite the theoretical advantages in the original concept, the project team advocated for modifying the direction of the grading from an axial configuration to a radial configuration. Several reasons justify this position.

- Manufacturability: Tubular ceramic bodies (whether they are graded or not) are typically made by casting or extrusion. A thorough literature review indicated that procedures for producing axially graded ceramic tubes have not been previously detailed. Conceptually, there are means by which such grading can be achieved (e.g., by controlled variation of the feedstock using in-line mixing or by pre-mixing multiple feedstock materials); however, the development of a completely new production technique suitable for future deployment is inherently risky and may require substantial development efforts to mature the process to a useful technology readiness level. Other means by which grading may be achieved have been considered. For example, discrete segments of tubes (each containing varying amounts of the materials) can be formed, where each segment can be fabricated by any number of conventional techniques. The segmented design is shown in Figure 9. The blue color indicates metallic alloy composition,

and the red color indicates ceramic composition. Varying compositions are indicated by graded colorations. A major disadvantage of a segmented design is the introduction of additional interfaces, each of which represents a high-risk region for failure [51]. Each interface of a varying composition may require the development of its own parameters for successful joining to the adjacent segments. In grading from a metal to a ceramic, the likelihood of a common set of parameters that can be used to join all segments in a single operation to form the transition joint is uncertain.

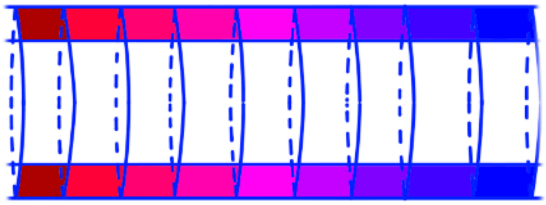

Figure 9. A schematic showing the segmented design of the transition tube

- Thermal-mechanical reliability: The use of monolithic ceramics to withstand substantial internal pressurization at high temperatures requires great care in the production of the material. Due to the flaw-limited strengths of brittle ceramic bodies, the probability of failure of any given component subjected to a set of loads will depend on the distribution of flaws present in the volume under load. Statistical approaches to estimate failure probabilities have been developed and can be applied in the present case to illustrate the magnitude of the challenge. As shown by Figure 8, the allowable stress is calculated at a given failure probability for a commercial grade of sintered SiC (e.g., Hexoloy SG) with a 311-MPa flexural strength and a Weibull modulus[8] of 18. From this, to achieve a failure probability of 1×10^{-5} in service, a maximum principal tensile stress of 100 MPa is advised. Therefore, the use of monolithic ceramics in the joint design requires materials with both high strength (at both ambient and elevated temperatures) and high reliability, as measured by the Weibull modulus. For a given material, the typical options available to improve component reliability are to reduce the volume of the material under load (e.g., by minimizing the component size) or to reduce the magnitude of the load (i.e., by judicious component design). For the joint applications, the magnitude of loads (as shown by the thermomechanical simulation results) due to thermal-elastic mismatch and internal pressurization may result in unacceptably high failure probabilities, even for mature advanced technical ceramic materials in monolithic form.

Without significant and compelling evidence from analytical or numerical models, it is difficult to suggest that an axially graded metal-to-ceramic configuration *with a reasonable graded length* provides significant reduction in maximum service stresses relative to grading in alternative directions. Therefore, the project team settled on employing a tubular SiC-based CMC (which has a similar chemistry to the SiC end component) as a key structural component of the transition tube in lieu of monolithic ceramic bodies. These CMCs have been proven to be reliable in high-temperature structural applications for aerospace and advanced energy systems, where flaw tolerance is derived largely from the high strengths of the ceramic fibers and their capability to maintain loading even when the matrix has failed. In addition, the SiC-based CMCs have a higher

[8] The Weibull modulus is a measure of the spread of the strength values for identical test specimens, where larger values indicate smaller spreads. Values larger than 10 are typical of advanced engineering ceramics.

technological maturity, as they have been investigated by various commercial and research entities, as shown in Table 1.

2.4 Development of Multi-Principal Element Alloys for Metal-End Joining

2.4.1 MPEA Filler Metal Down-Selection Process

No commercial alloys were found to be directly suitable for a dissimilar SiC-to-In740H joint at the high service temperatures associated with CSP applications. We performed a novel multi-principal element alloy (MPEA) design and down-selection process to determine candidate alloy compositions as a braze filler. The entire down-selection process was comprised of four filters: (1) alloy system creation and basic physics-based criteria, (2) high-throughput Scheil-Gulliver solidification simulations, (3) equilibrium phase diagram prediction, and (4) diffusion and kinetics calculations. While Filters 1 through 3 were performed prior to the beginning of any experimental work, Filter 4 was performed alongside experimentation. The objective was to down-select alloy composition(s) that are compatible or exhibit good wettability with both In740H and SiC.

2.4.1.1 Filter 1: Alloy System Design Using Physics-Based Criteria

Filter 1 began by creating all potential composition spaces in a MATLAB script that permuted all possible alloy combinations that fell within a given criteria (see Table 2 for details). Note that all the elements in Table 2 were based on literature search that could facilitate wetting on either or both substrate materials. This created a full set of composition spaces with 16.6 million possible alloy combinations within 55,440 distinct alloy systems.

Table 2. Input Parameters for Composition Space Creation

Parameter	Metric
Number of Elements Allowed	5
Min Alloying Content (at.%)	5
Max Alloying Content (at.%)	35
Min Allowed Difference in Composition (at.%)	0.1
Included Elements	Ti, Fe, Ni, Si, Cr, Mn, Co, Cu, Zr, Nb, Mo

After the composition space was created, the individual alloys were filtered through a set of physics-based parameters that removed alloys that were highly unlikely to solidify as a face-centered cubic (FCC) crystal structure. These parameters are given in Table 3.

Table 3. Filtering Parameters for Filter 1

Parameter	Metric
Atomic Size Mismatch (δ)	0.06
Minimum Valence Electron Count	8
Entropy of Mixing Range $\left[\frac{J}{mol \cdot K}\right]$	5.212 to 5.812
Enthalpy of Mixing Range $\left[\frac{kJ}{mol}\right]$	-15 to 5

After the first step of filtering, the number of potential alloys dropped from 16.6 million to 574 thousand within 14 alloy systems, eliminating 96.55% of all individual alloy combinations and 99.97% of all alloy systems. The final criterion in this filter was based on the probability that an alloy system would be successful through the rest of the filtering steps. Hence, alloy systems with more than 30,000 potential alloy combinations were selected to progress to Filter 2. This criterion reduced the alloy systems from 14 to 6, narrowing the list down to the following systems: (1) AlCrFeCoNi, (2) AlMnFeCoNi, (3) SiMnFeCoNi, (4) TiCrFeCoNi, (5) TiMnFeCoNi, and (6) CrMnFeCoNi. These are summarized in Table 4.

Table 4. Alloy Systems Remaining After Filter 1

Index	Element 1	Element 2	Element 3	Element 4	Element 5	Remaining # of Compositions	% of Remaining Set
1	Al	Cr	Fe	Co	Ni	31417	5.6771
2	Al	Mn	Fe	Co	Ni	68695	12.4132
3	Si	Mn	Fe	Co	Ni	36874	6.6632
4	Ti	Cr	Fe	Co	Ni	45033	8.1375
5	Ti	Mn	Fe	Co	Ni	79591	14.3822
6	Cr	Mn	Fe	Co	Ni	257923	46.6069

2.4.1.2 Filter 2: High-Throughput Scheil-Gulliver Solidification Simulations

High-throughput Scheil-Gulliver solidification simulations were then performed for the six alloy systems defined in Table 4 to predict the solidification characteristics. For each alloy system (also referred to as an "index"), the upper and lower boundaries for the composition of each element were identified and set as the maximum range for the alloy compositions. This filtering step includes seven parameters, as listed in Table 5.

Table 5. Filter 2 Input Parameters

Input Parameter	Value
Required Minimum Solid Fraction	0.9
Ideal Final Solid Fraction	0.93
Fraction of Liquid at Solidus Temperature	0.05
Simulation Starting Temperature [°C]	2,500
Minimum Liquidus Temperature [°C]	1,000
Maximum Liquidus Temperature [°C]	1,288
Required FCC Fraction	0.5

The liquidus solid fraction and the minimum solid fraction required to end the simulation were defined by the "required minimum solid fraction." The "ideal final solid fraction" was the desired cut-off molar fraction of solid for the simulation. The solidus temperature was calculated by defining the input "fraction of liquid at solidus temperature." The "simulation starting temperature" was set to the default given by Thermo-Calc. The minimum and maximum liquidus temperatures were set based on expected processing temperatures and the melting point of In740H, respectively. Finally, the "required FCC fraction" was the required mole fraction of the solidified material that had to be an FCC crystal structure for the composition to pass this filter. The first four parameters were required for the simulations, whereas the last three were set points for filtering.

The naming convention for the MPEA alloys is given here. All alloys produced from Filter 2 are MPEAs; therefore, the first section of the name is "MPEA". The second portion of the name indicates from which index the sample was taken. This means that the second portion is "i" followed by the index number in Table 4. The third portion of the name refers to the specific sample within the given index and is designated by an "s" followed by a number. The final portion designates which ceramic system the MPEA is designed for, i.e., SC for silicon carbide.

The unfiltered results of the Scheil-Gulliver simulations provide a view of the general solidification trends of each index. An example is given below. Figure 10(a) is a compilation of the solidification curves for 200 samples from the MPEAi4SC system. This data is made more concise in Figure 10(b), where a histogram of the solidus temperature is plotted. The figure shows that most compositions have a solidus temperature between 1,000°C and 1,075°C.

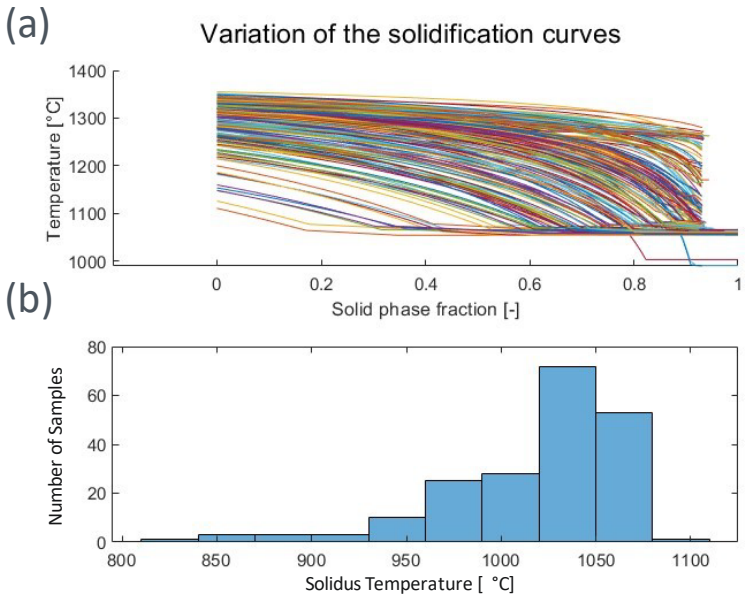

Figure 10. Unfiltered results of the Gulliver-Scheil simulations

The simulation and program for Filter 2 removed four more alloy systems from the list of indexes. Only Indexes 4 and 5 passed the filter, with Index 4 including two compositions and Index 5 including eight compositions. Table 6 lists the passing alloys. Five more alloys were eliminated for their high volume fractions of brittle intermetallic phases. The five alloys that remained after the manual examination are highlighted in green in Table 6.

Table 6. Alloy Compositions (in at.%) That Passed Filter 2

Alloy	Ti	Co	Fe	Cr	Mn	Ni
MPEAi4s9SC	18.87	29.90	8.29	20.39	0	22.55
MPEAi4s10SC	19.64	27.68	8.32	18.41	0	25.95
MPEAi5s13SC	18.47	22.89	18.09	0	11.11	29.43
MPEAi5s22SC	18.92	21.13	23.02	0	10.46	26.47
MPEAi5s28SC	19.35	21.29	25.56	0	10.23	23.57
MPEAi5s33SC	20.87	21.82	19.29	0	10.91	27.11
MPEAi5s136SC	16.32	24.24	19.67	0	9.63	30.14
MPEAi5s139SC	20.80	29.50	22.13	0	6.83	20.75
MPEAi5s143SC	23.44	23.46	20.13	0	6.85	26.11
MPEAi5s200SC	22.62	26.46	17.23	0	7.72	25.97

2.4.1.3 Filter 3: Equilibrium Phase Diagram Calculation

The five remaining alloys from Filter 2 were further investigated using Thermo-Calc's Calculated Phase Diagram (or "CALPHAD") module to reveal what phases would be present during brazing (not yet taking into consideration the interaction with the substrate materials) and, more importantly, at service conditions. The only input parameters for this filtering step were the compositions of the alloys down-selected in Filter 2 and the temperature range over which to calculate the equilibrium phases.

There were only two alloys that were calculated to have low concentrations of brittle intermetallic phases during equilibrium at 725°C. These were MPEAi4s9SC and MPEAi4s10SC. However, from previous knowledge of the detrimental effects of titanium on the formation of Laves intermetallic phases, we hypothesized that if the titanium content was reduced in MPEAi5s200SC to about 1 at.% and the balance was given to nickel, the FCC phase at 725°C could become more stable. Once the composition was adjusted to reflect this hypothesis, we ran the CALPHAD simulation again. FCC was predicted to be the only stable phase at 725°C. However, the increased nickel content caused the liquidus temperature to exceed 1,300°C, which renders this alloy unusable for brazing. Therefore, at the end of the CALPHAD simulation steps, only MPEAi4s9SC and MPEAi4s10SC were considered feasible options. The phase diagrams of these alloys are shown in Figure 11.

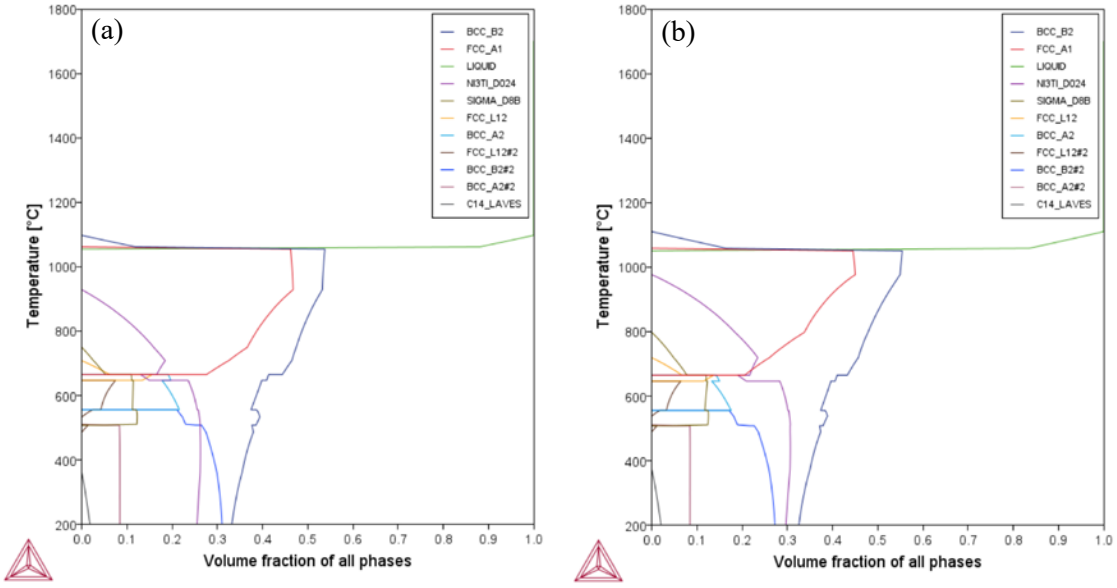

Figure 11. Calculated phase diagrams for (a) MPEAi4s9SC and (b) MPEAi4s10SC

2.4.1.4 Filter 4: Interface Diffusion Calculations

The fourth filtering step is a process that runs in tandem with experimental work because it must be validated by experimental results. Nonetheless, Filter 4 aids in the understanding of the diffusion products that will appear during brazing. In this process, the chemical composition of the MPEA filler and the ceramic were input as parameters for the diffusion calculation. The time, temperature, and initial concentration gradient were also included, and the Thermo-Calc diffusion ("DICTRA") module was used to predict the precipitation of phases across the interface between MPEAi4s9SC and SiC. Because of the computational complexity and time-consuming nature of MPEA diffusion calculations, the initial concentration gradient was assumed to follow the error function curve, as shown in Figure 12. For these calculations, the temperature was at 1,025°C and the hold time was 10 seconds. There was no temperature ramp included in the calculation. At this point, only MPEAi4s9SC was successfully run in DICTRA simulations. The process for these simulations was both time consuming (~1 week) and computationally intensive.

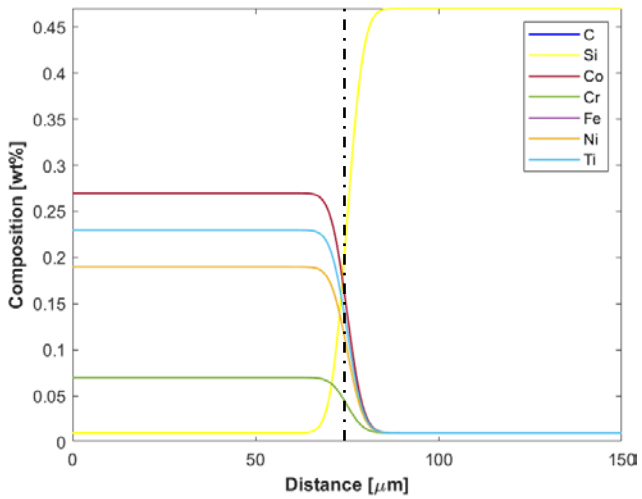

Figure 12. Initial concentration gradient for MPEAi4s9SC to SiC diffusion calculation

The first set of diffusion simulations were over a calculated distance of 25 µm. After we discovered that this distance window was too small to accurately represent the system, we increased the calculated distance to 150 µm. The results in Figure 13 shows that there were three main areas of interest: the MPEA side of the interface from 0–69 µm, the interface region from 69–75 µm, and the SiC side of the interface beyond 75 µm. Although the composition at 0 µm was set to the composition of MPEAi4s9SC, immediately past that point, the composition drifted to an increased mass percent of titanium, a sharp increase in silicon, and a sharp increase in carbon, while the rest of the elements appeared depleted. This indicated that the region far from the interface had permitted high diffusion of both carbon and silicon into the MPEA and diffusion of the other alloying elements out of the primary matrix and into the interface region. The area from 0–69 µm was predicted to be characterized by very high amounts of titanium silicides and carbides. In the interface region from 69–75 µm, there were only two data points for each element composition. Therefore, although there appeared to be multiple subregions within the interface region, this cannot be accurately determined without more precise calculations. In this narrow region, the concentrations of all alloying elements were greater than zero, and all metallic elements except for titanium were enriched. This likely indicated the formation of various metal carbides and silicides, rather than the primarily titanium carbides and silicides that formed in the other areas of the joint. From 75–150 µm, the composition was similar to the other side of the interface except that there was an increase in chromium content and the slope of the chromium concentration curve mirrored the slope of the titanium concentration curve. This likely indicated competitive formation between the chromium and titanium intermetallic phases.

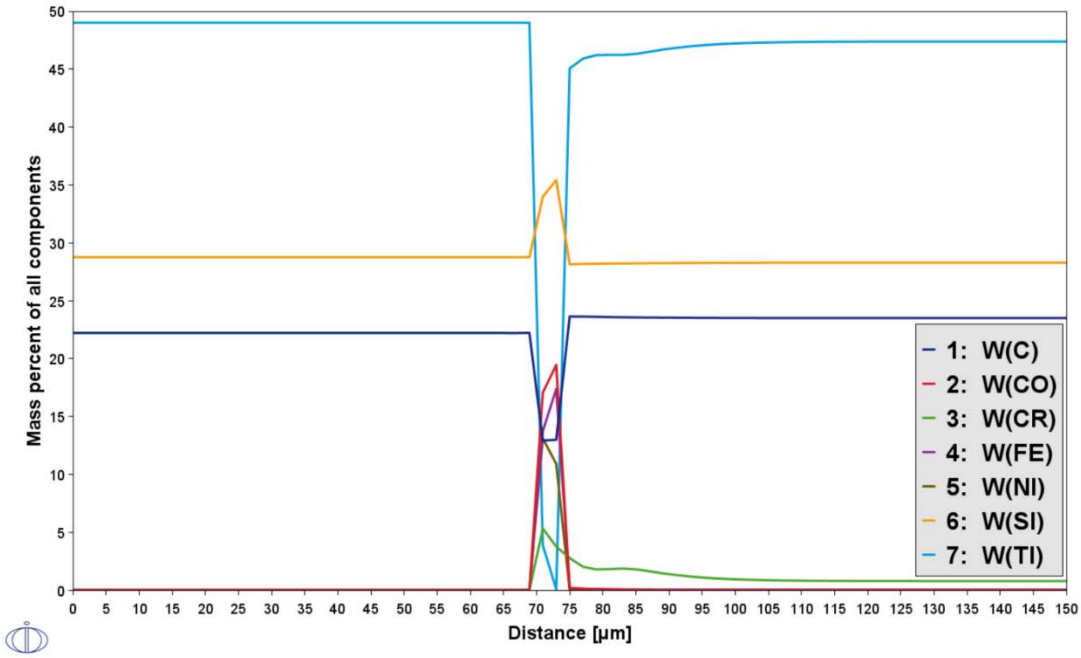

Figure 13. DICTRA simulation results for MPEAi4s9SC

While the DICTRA diffusion simulations can be helpful based on the first simulation sets, there was doubt regarding the accuracy of the predictions made. It seems unlikely that the MPEA would lose nearly 70 µm of material to diffusion. The systems being modeled are highly complex, and experimental validation is necessary to determine the reliability of these calculations.

2.4.2 Preliminary MPEA Filler Fabrication, Metallurgical Analysis, and Bonding Trials

2.4.2.1 Fabrication of Preliminary MPEA Compositions

Two MPEA samples were down-selected and fabricated based on the predictions made during the composition filtering steps. The nominal compositions for these two MPEA samples are given in Table 7.

Table 7. Nominal Compositions of the Down-Selected MPEA Samples

Sample	Nominal Composition (at.%)				
	Ti	Co	Cr	Fe	Ni
MPEAi4s9SC	21.78	28.03	8.81	20.17	21.22
MPEAi4S10SC	22.65	25.92	8.83	18.20	24.41

These samples were first made using a lab-scale vacuum arc melting furnace and a gas-tungsten arc welding electrode with a peak current of 200 amperes affixed above a water-cooled copper platan, shown in Figure 14. The raw materials were placed in one well, while titanium getters were placed in the other wells to reduce the oxygen content in the air during melting. The vacuum chamber underwent six vacuum/purge cycles where the chamber was evacuated below 1300 µm Hg and subsequently purged with industrial-grade argon before melting. Then, the Ti getters were each melted twice to absorb residual atmospheric oxygen. Once this process was complete, the

MPEA raw materials were melted and cooled before the chamber was opened and the sample was retrieved. The MPEA buttons were flipped and remelted a minimum of three times to ensure bulk compositional homogeneity. A post-fabrication image of the experimental setup can be seen in Figure 14.

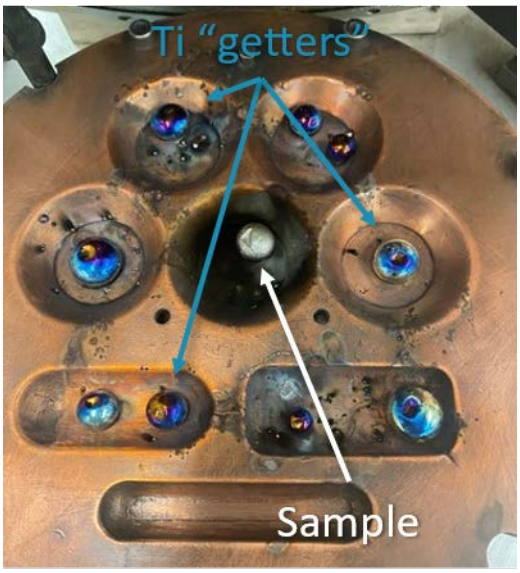

Figure 14. Vacuum arc-melting furnace experimental setup for MPEA fabrication

2.4.2.2 Metallurgical Analysis of MPEA Samples

Once the samples were fabricated, metallurgical analysis was performed using optical microscopy and scanning electron microscopy (SEM) with energy dispersive spectrometry (EDS) on MPEAi4s9SC #1. This sample was polished to 1 µm and etched with undiluted aqua regia solution for 3 seconds by immersion before rinsing with deionized water and isopropanol. The as-cast condition in Figure 15 revealed very large grains with long dendrites, as expected from the casting method. Individual grains were indicated by clusters of dendrites with a unique orientation. The light, unetched region along the edges of the sample was likely the result of the copper-containing mount providing cathodic protection during etching. Aside from the unetched edges, no fabrication anomalies were detected.

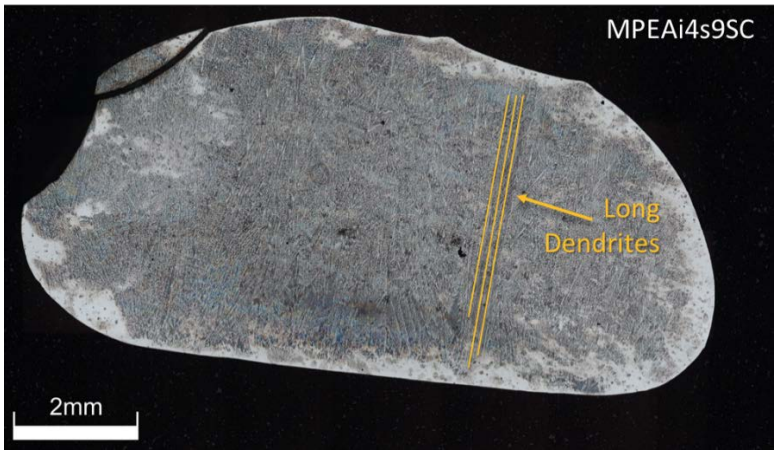

Figure 15. Macrograph of MPEAi4s9SC #1 in the as-cast condition after sectioning, polishing, and etching

A few observations were made from the EDS scans (Figure 16). First, Co was homogeneously distributed throughout the microstructure, with little to no preference of segregation for the dendrite core or interdendritic region. Second, Ni tended to partition away from the dendrite core and into the interdendritic region. This left the dendrite cores locally rich in Ti, Cr, and Fe. A comparison of the Ni and Ti maps in particular showed that where the Ni was enriched, Ti appeared depleted, and vice versa. This may be due to the atomic size mismatch of these elements, as they have the largest difference between them of any two elements in the alloy, and was a first indicator of phase separation. Additionally, there were Ti-rich particles where all other elements were low, and oxygen did not appear enriched in these areas. Therefore, these Ti-rich particles were likely not titanium oxides. As there were only small compositional variations and between MPEAi4s9SC #1 and MPEAi4s10SC #1, the preliminary EDS analysis in Figure 16 was considered representative of the microstructural constituents in both materials, which were evaluated further by synchrotron X-ray diffraction (XRD).

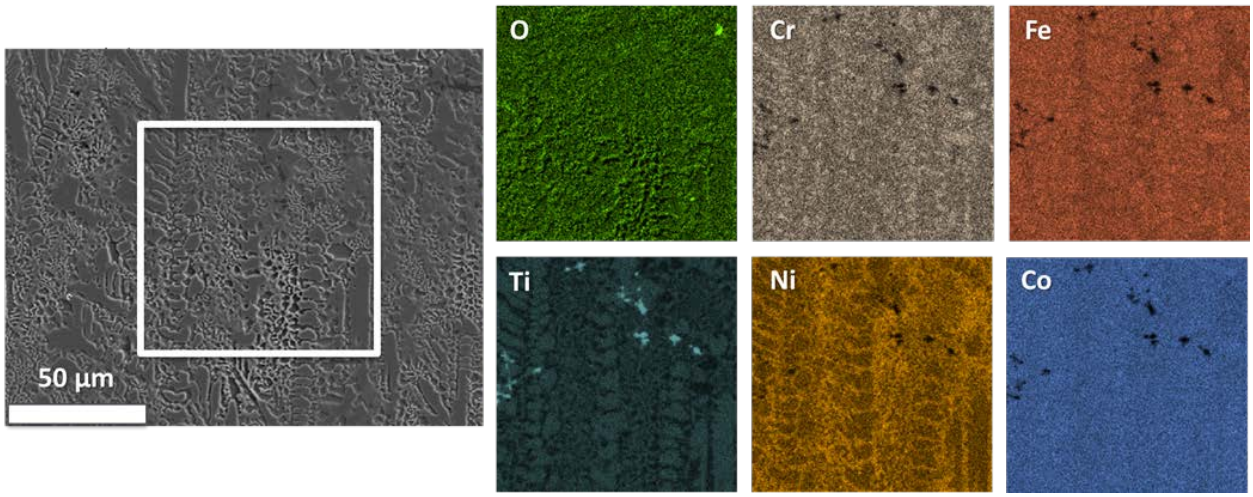

Figure 16. EDS maps of O, Cr, Fe, Ti, Ni, and Co for MPEAi4s9SC #1

2.4.2.3 *In Situ Synchrotron X-Ray Diffraction Setup and Experimentation*

To evaluate the constituent phases present in the MPEAs, including intermetallic compounds, samples were prepared and sent to the Advanced Photon Source (APS) at Argonne National Laboratory for assessment by high-energy synchrotron XRD. Additionally, to assess the complex interactions that may occur during brazing, we also conducted a set of in situ laser-melting experiments in which the MPEA was melted upon a SiC substrate piece, with XRD patterns collected from a fixed location at high temporal resolution during melting and re-solidification.

Samples consisting of a SiC substrate piece and an MPEA filler piece were prepared for the in-situ experiment, with the two pieces assembled prior to laser-melting using an adhesive tape. Both pieces were machined to 500 ± 100 µm in thickness using a slow-speed saw. The height of the SiC substrate was approximately 4 mm, and the MPEA filler height was 500 µm. The overall sample length was approximately 7 mm. The sample geometry is summarized in Figure 17(a). This sample geometry was also employed for the collection of ex situ (static) diffraction patterns from the MPEA prior to laser-melting.

Figure 17(c) depicts the experimental diffraction setup, showing the position of the incident and diffracted beams, detector, and sample. A Pilatus3X CdTe 2M hybrid photon counting detector with a sample-to-detector distance of 680 mm was used to collect diffraction patterns. Before and after melting, radiographs were also taken to image each sample using a 2x PointGrey detector with camera model Gs3-u3-23s6m-c with a 2 mm by 1 mm field of view. For the static diffraction patterns, the incident beam dimensions were 100 µm horizontally by 50 µm vertically, and the detector exposure time was 0.1 s. Static patterns were collected from a series of at least 10 locations in the MPEA material, and locations were averaged to evaluate a larger diffracting grain population and to approach a powder pattern condition. All two-dimensional patterns were reduced to one dimension by azimuthal integration of the full pattern, performed using the FIT2D software calibrated using a cerium oxide standard.

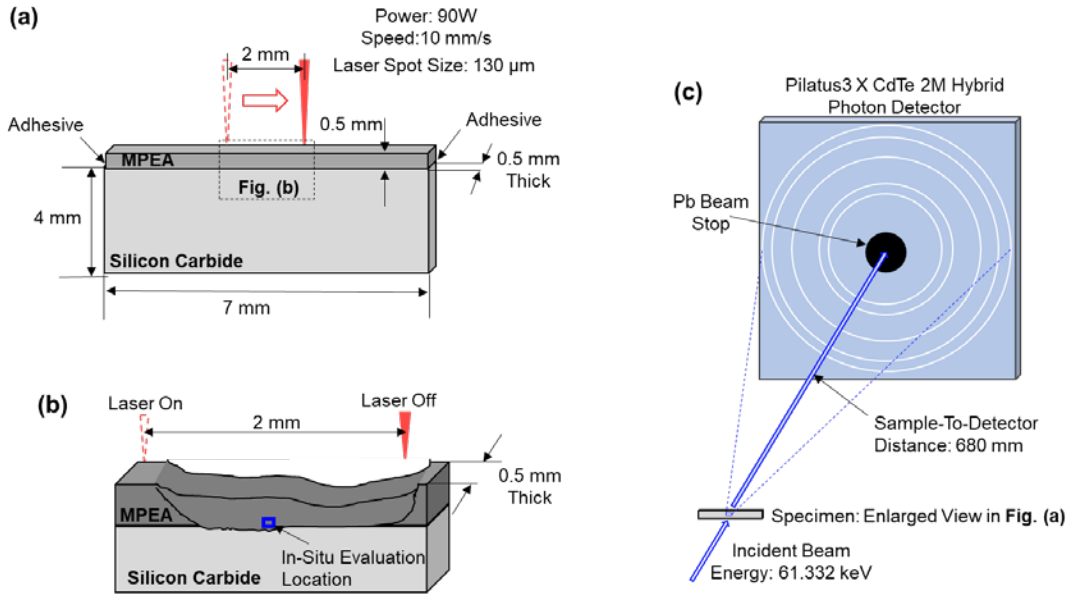

Figure 17. Schematics of (a) the sample geometry for synchrotron X-ray diffraction and the laser-melting setup, (b) after laser-melting, and (c) the diffraction experiment setup

For the in situ patterns, the incident beam dimensions were 50 µm horizontally by 30 µm vertically, the detector exposure time was 1 ms, and the detector frame rate was 4 ms. The laser parameters were tuned using trial and error to a power of 90 W, a scan speed of 10 mm/s, and a spot size of approximately 130 µm. The material was evaluated in situ approximately 100 microns above the filler/substrate, at the location indicated schematically in Figure 17(b). All laser-melting was performed in an environmental chamber evacuated to 100 mTorr and backfilled with argon gas.

The single-axis equilibrium phase diagram calculated for MPEAi4s10SC using Thermo-Calc Software is shown in Figure 18. The static patterns for this alloy were collected following heat treatment at 975°C for 15 minutes and water quenching to evaluate the microstructure after a solutionizing heat treatment. Solutionizing was attempted because a cold-rolling trial on the as-cast MPEAi4s10SC yielded brittle results, with prolific cracking before the sample reached a 10% thickness reduction. Based on the calculated phase diagram in Figure 18, 975°C was within the predicted temperature range where only FCC and body-centered cubic (BCC) solid solutions should be present. However, the kinetics of solutionization were not yet evaluated, so the selected heat treatment time may have been insufficient for complete solutionizing. The MPEAi4s9SC samples were left in the as-cast condition. Because the material was melted again by the laser for the in situ experiments, the prior thermal history would have had little bearing on the in situ and postmortem diffraction data.

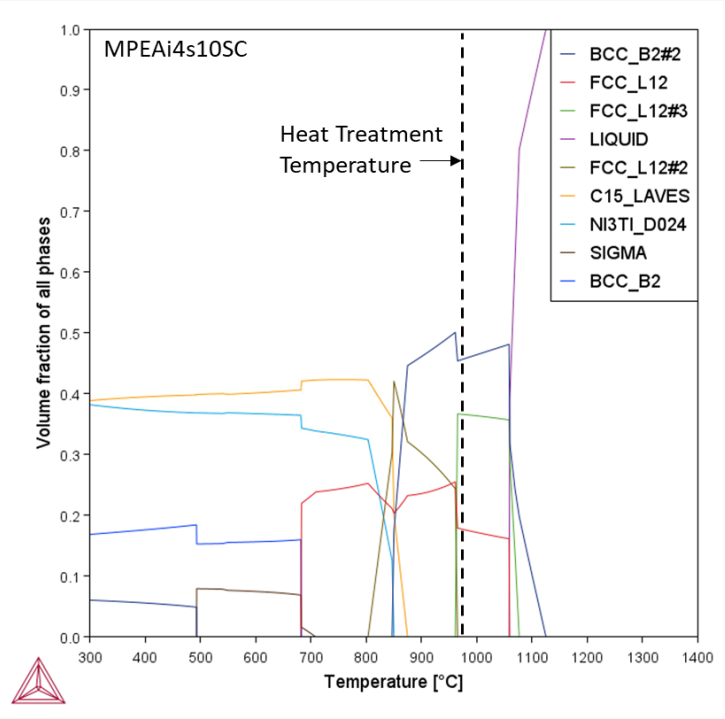

Figure 18. Single-axis equilibrium diagram for MPEAi4s10SC, showing the equilibrium volume fraction of phases as a function of temperature

Figure 19 shows examples of static diffraction patterns (plotted against $q = 2\pi/d$) taken from each un-melted MPEA material, averaged over 10 locations within the material. A rigorous peak identification process for these patterns was nontrivial for these newly fabricated MPEA compositions. A few important conclusions could be drawn by inspection. First, neither pattern

was consistent with either a single-phase FCC or a single-phase BCC structure, indicating that a mixture of phases and/or phases with lower symmetry were present. Secondly, the pattern for heat-treated MPEAi4s10 in Figure 19(a) contained many peaks that were absent in the pattern for as-cast MPEAi4s9 in Figure 19(b). This finding indicated that heat-treated MPEAi4s10 may contain an additional phase or a phase with a different ordering scheme compared to as-cast MPEAi4s9, either because of its different composition or its different thermal history. Considering the similar compositions reported in Table 7, it is likely that the difference in thermal history was an important factor, and the solutionizing attempt resulted instead in a more complex microstructure.

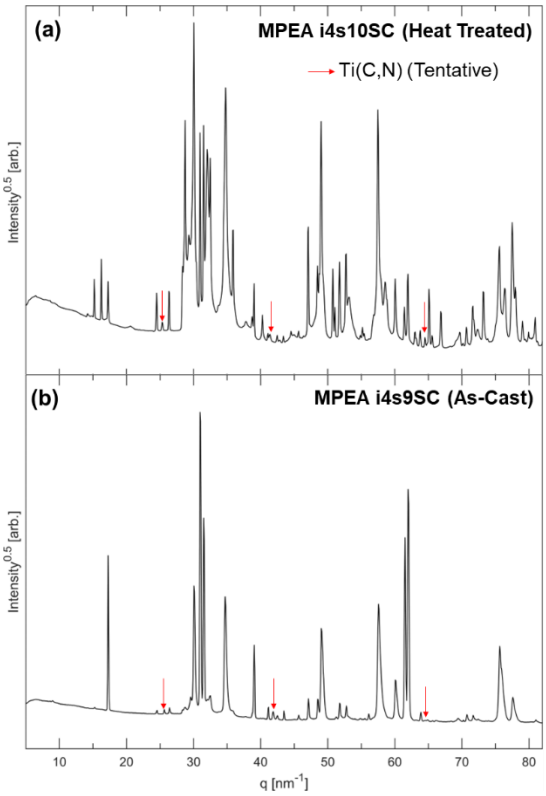

Figure 19. Static synchrotron X-ray diffraction patterns for (a) MPEA i4s10SC, heat-treated at 975°C for 15 min and (b) as-cast MPEA i4s9SC

One minor phase whose peaks could be readily identified in the diffraction patterns was Ti(C,N), with the peaks tentatively labeled in Figure 19. The presence of this phase was consistent with the presence of Ti-rich particles identified in Figure 16, and clearly visible in higher-magnification SEM images such as Figure 20, which shows MPEAi4s10 in its heat-treated condition. These particles were seen throughout the microstructure and, as indicated by their sharp edges and corners, were likely incoherent or semi-coherent with the surrounding matrix. The smaller white particles on the surface were consistent in size with the colloidal silica medium used in the final polishing step, and thus may represent an artifact from polishing.

Beyond the Ti(C,N) particles, at least two phases, labeled α and β, are indicated in Figure 20. Despite the heat treatment applied to MPEAi4s10, the α and β phases retained evidence of the solidification structure from the arc-casting process. The large, globular, island-like morphology of the α phase, alongside a lamellar-type α/β mixture, was consistent with the proeutectic

solidification of α and the subsequent eutectic solidification of α + β. Analysis of the collected in situ synchrotron XRD data can help confirm this solidification sequence.

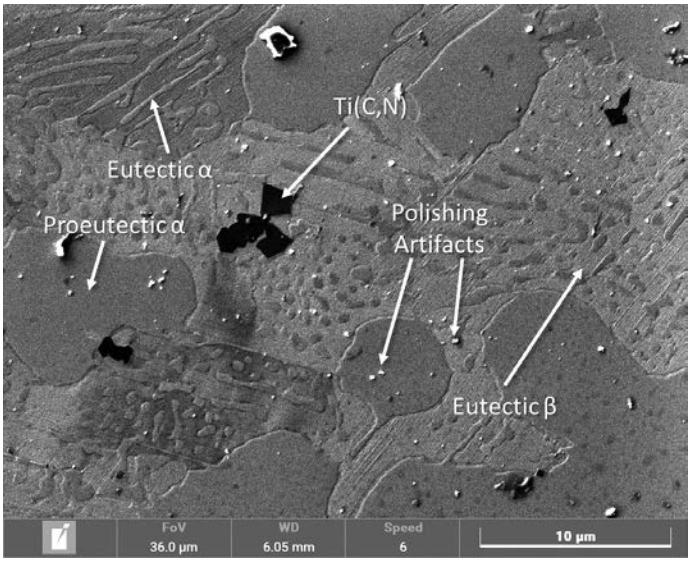

Figure 20. Electron micrograph of heat-treated MPEAi4s10SC showing the three potential phases and polishing artifacts

The β phase was characterized by the fine, parallel, and linear features within it. Higher-resolution imaging, such as with a transmission electron microscope (TEM), is required to characterize these features further. They may be needle-like precipitates that formed during the applied heat treatment, which could account for the additional diffraction peaks in Figure 19(a) that were absent in Figure 19(b). Alternatively, their parallel nature could be indicative of slip lines, which would indicate deformation in the β phase at some point during processing. If this were the case, these marks would point to the possibility that the α phase was harder and the β phase was softer and more ductile. Table 8 summarizes the composition of the α and β phases in the as-heat-treated MPEA, measured by point-based EDS,[9] averaged over six locations. This analysis indicates that α corresponds to the Ti-rich dendrites and β corresponds to the interdendritic regions previously identified.

Table 8. EDS Compositions of the α and β Phases in MPEAi4s10SC

	EDS Composition (at.%)				
	Ti	Co	Cr	Fe	Ni
α phase	28.5	27.7	7.8	19.6	16.4
β phase	21.5	24.3	8.1	18.4	26.5

Table 9 summarizes the set of in situ samples analyzed at APS. In addition to the samples prepared using SiC and the two MPEAs in Table 7, a few other experiments were performed. These included a weld directly between In738 and SiC; a weld of a different MPEA filler, MnFeCoNiCu [67] (developed by the CSM team for Ni brazing), upon SiC; and a weld of MPEAi4s10SC upon In738. In738 was selected as a substitute for In740H because samples cut to the appropriate geometry

[9] With atomic number, absorption, and fluorescence excitation (ZAF) correction

were readily available. Because the most significant challenge in brazing In740H to SiC is wetting SiC, the focus of the analysis was on the welds of MPEAi4s10SC or MPEAi4s9SC upon SiC; results from all the experiments in Table 7 are available for future analysis.

Table 9. Sample and Experiment Setup Information for the APS Samples

Sample Designation	Filler	Substrate	In Situ?	Laser Power	Notes
A	MPEAi4s9SC	SiC	Yes	100 W	As-cast
B	MPEAi4s9SC	SiC	Yes	90 W	As-cast
C	MPEAi4s10SC	SiC	Yes	90 W	Heat-treated
F	MPEAi4s10SC	SiC	Yes	190 W	Heat-treated
H	MPEAi4s10SC	SiC	Yes	90 W	Heat-treated
K	MPEAi4s10SC	N/A	No	N/A	As-cast; static; filler only
X	In738	SiC	Yes	150 W	
Y	Filler from [67]	SiC	Yes	100 W	As-cast
Z	MPEAi4s10SC	In738	Yes	150 W	Laser weld

Analysis of the in-situ diffraction data was performed to supplement the phase identification previously described, and to determine the phase solidification sequence in a laser-melting environment. A more immediate outcome of the laser-melting experiments was a postmortem assessment of the wetting behavior of the MPEAs upon SiC. X-ray radiographs, such as those in Figure 21, were taken to image each sample before melting (i.e., Figure 21(a)) and after melting (i.e., Figure 21(b)). Figure 21(b) shows that the laser weld affected the uppermost edge of the SiC, generating a rougher appearance. Instances of circular porosity in the filler, as well as dendrites growing upward from the interface, were also visible in the postmortem radiograph.

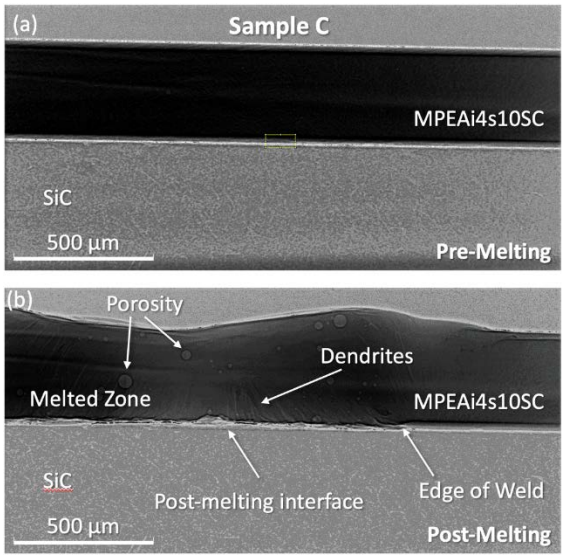

Figure 21. Example X-ray radiograph of APS sample C before and after laser melting

From the radiograph alone, it was difficult to assess the extent of bonding between the MPEA and SiC. Rather than being indicative of bonding, the roughened interface may be caused by the MPEA filler beading on the surface. A transverse cross section would allow for an assessment of the wetting angle; however, the laser-melting samples were too delicate to perform this sectioning. In the selected-area radiograph in Figure 22, there was apparent variability in the quality of the bond along the length of the weld, with some regions displaying a clear interfacial gap and others indicating some possibility of bonding.

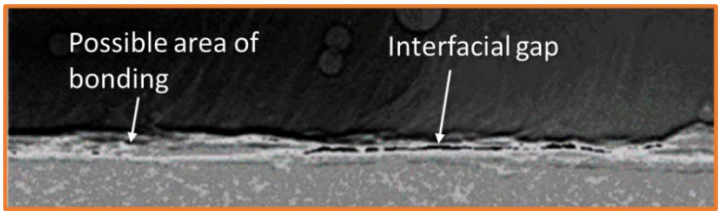

Figure 22. Detail view of interface region from the APS sample C

Optical microscopy was performed to support the observations made by radiography. In the optical macrographs in Figure 23(a) and Figure 23(b), the resolidified material appeared rounded, as if it were beading on a nonwetting surface. This was particularly evident for the sample in Figure 23(b), where a gap was visible beneath a portion of the filler material. Without a transverse cross section, the wetting angle could not be measured, but this convex, beaded appearance indicated that the wetting angle was likely high. Figure 23(c) shows the post-melting radiograph corresponding to the sample and location in Figure 23(b). When compared, it was evident that the region with a clear gap in the optical micrograph did not appear as a gap in the radiograph. The appearance of material overlap in the radiograph can be explained by the sample being slightly askew relative to the incident beam (i.e., not perfectly perpendicular). In general, the viewing angle could cause the appearance of overlap in any of the postmortem radiography, emphasizing that further characterization is necessary to assess the quality of the bond. Additionally, certain laser-melted specimens fell apart upon handling for metallographic preparation and polishing, indicating that any bond that existed between SiC and the MPEA filler was not strong.

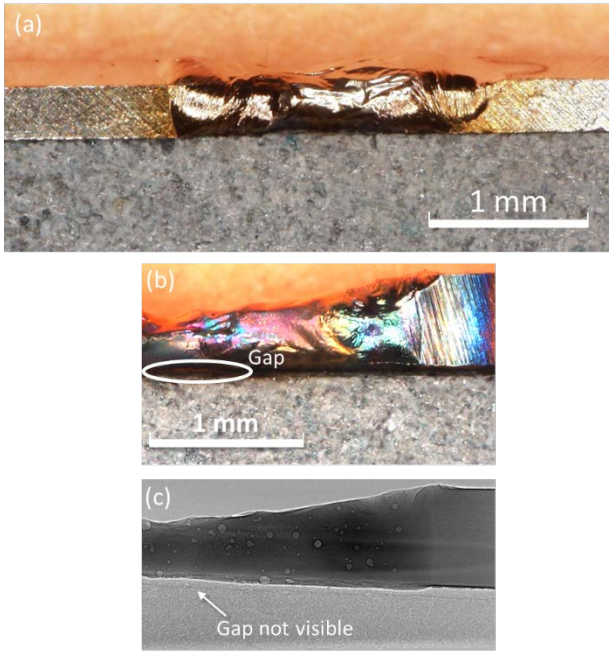

Figure 23. (a–b) Optical macrographs of selected laser-melting specimens of MPEAi4S10SC upon SiC. (c) X-ray radiograph at the location corresponding to (b).

An additional dataset characterizing the interface behavior after laser-melting consists of the SEM and EDS data in Figure 24. This EDS mapping analysis did not show any interdiffusion across the interface and provided a very clear line between the MPEA elements and the Si-rich silicon carbide, indicating the presence of a potentially weak metallurgical bond.

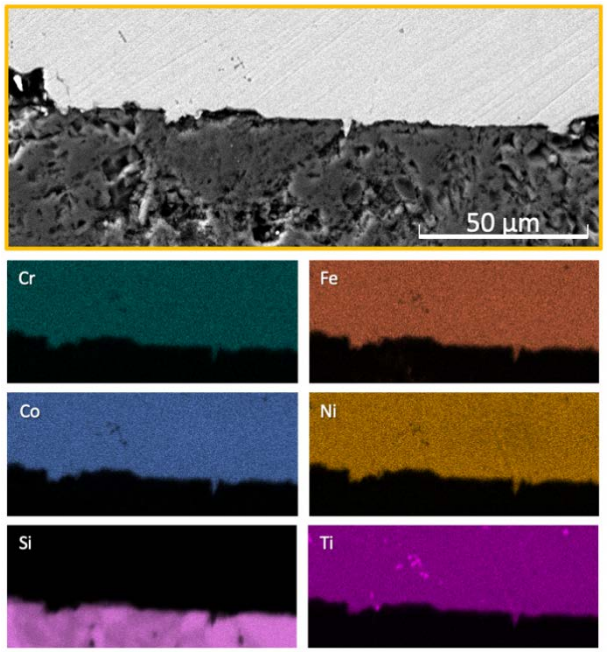

Figure 24. EDS maps of a laser-melting sample of MPEAi4S10SC upon SiC at the SiC/MPEA interface

The optical micrographs, X-ray radiographs, and EDS data indicated a lack of good wetting in the laser-melting experiments. The lack of wetting may be because of the low heat input or the extremely short heating time of the laser. To test this hypothesis, we planned furnace brazing experiments. Additionally, as evidenced by Figure 23(b), for certain laser melting experiments, there was enough oxygen present in the environmental chamber to form oxides on the surface of the laser-melted MPEA. Better control of oxygen in a vacuum furnace could potentially improve the wetting behavior.

Despite the apparent lack of bonding during the laser-brazing trials, the in situ XRD experiments provided data to enable an assessment of the evolution of the constituent phases present in the material during solidification. This was in conjunction with the analysis of the static diffraction data. An initial postmortem SEM micrograph is provided is Figure 25(a) for the sake of comparison to the microstructure before laser-melting in Figure 20. Based on the quantified line scan data in Figure 25(b), we proposed that the same α and β phases indicated in Figure 20 with compositions listed in Table 8 were present in the laser-melted material. However, the morphology was different in Figure 25 than in Figure 20, with the eutectic microconstituent more difficult to identify here. This finding was suggestive of a different solidification mechanism during laser-melting than in arc-casting, which may reinforce the idea that longer time-temperature exposures and slower cooling rates may have changed the wetting behavior upon SiC.

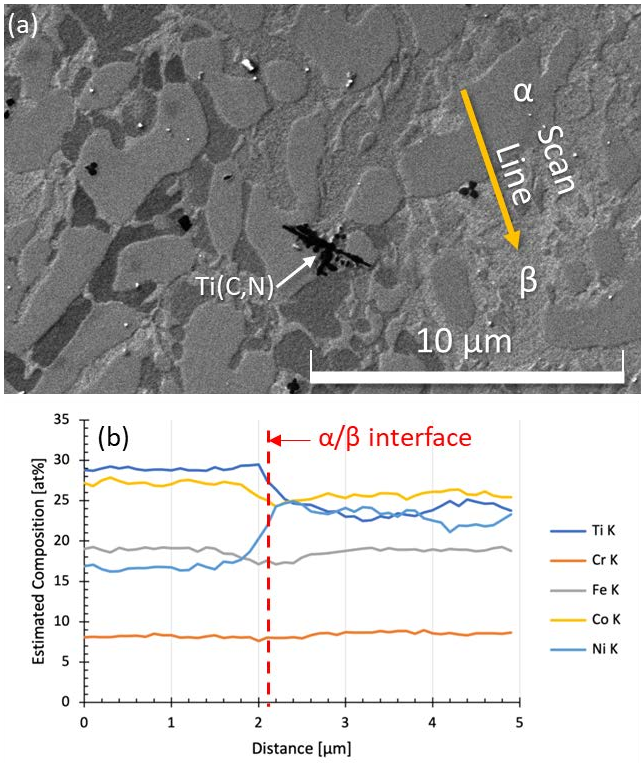

Figure 25. (a) SEM micrograph and (b) EDS line scan between α and β phases in laser-melted MPEAi4s10SC

2.4.2.4 Diffusion Bonding and Commercial Brazing Experiments

For the preliminary diffusion bonding experiment, a small disk of In740H was placed on a substrate of nitride-bonded SiC.[10] The SiC and In740H were polished to 1 µm before the experiment to attempt to create a surface finish facilitating diffusion bonding. The In740H was approximately 3 mm thick with a diameter of 12 mm. The SiC substrate was also approximately 3 mm thick but with a 25.4-mm diameter. This sample was then inserted into a stainless-steel heat treatment bag with two titanium getters for the experiment to avoid oxidation. Pressure for diffusion bonding was provided by placing a 6.57-kg steel cylinder on top of the sample outside of the bag. However, because the steel cylinder was significantly larger than the sample upon which it was balanced, and fixturing was difficult inside the furnace, the cylinder tilted during the process, reducing the applied load. For this experiment, the sample was heat treated under load at 1,150°C for 16.5 hours. The sample was then furnace-cooled to below 200°C and air-cooled to room temperature. Because the experiment was performed at high temperatures over a long period, the stainless-steel heat-treatment bag disintegrated due to oxidation and kindling inside the furnace. Upon opening the furnace to retrieve the sample, only small fragments of the bag were left.

Once the sample was removed from the furnace, it was clear that there was no lasting bond between the two materials. As shown in Figure 26, there was a region on both the SiC and In740H surfaces that indicated some bonding. However, this small area was not strong enough to keep the sample together after removal from the furnace. The SiC disk was separated from the In740H upon handling. The dull color and high roughness of this region, however, indicated that the residual material was pulled from the SiC side of the joint rather than the In740H side. Another observation was that a green oxide layer remained on the surface of the SiC where it contacted the In740H disk. A similar oxide could also be seen on the In740H surface in some areas. The In740H side of the sample was sectioned along the white dotted line in Figure 26, and the revealed surface was polished for microscopy.

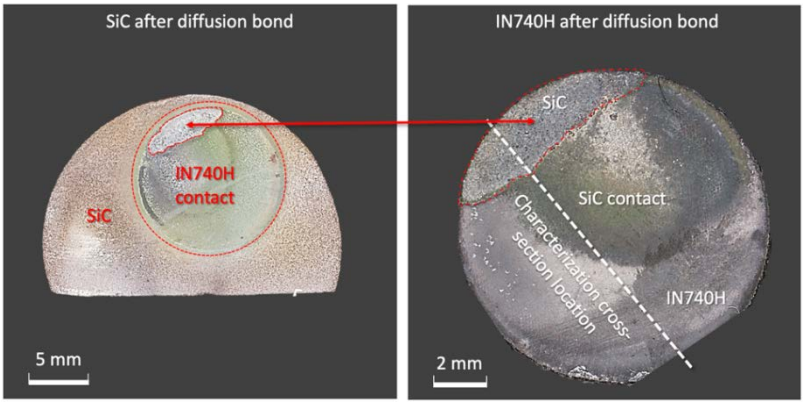

Figure 26. Joint interface after diffusion bonding experiment; SiC (left) and In740H (right)

After performing microscopy and EDS, we determined that on the surface between the In740H and the SiC, there was a reaction product that formed, which may account for the apparent bond surface seen in Figure 26. As is evident in Figure 27, O, Si, Al, and Cr were enriched at or near

[10] Nitride-bonded SiC contains 20%–30% Si_3N_4.

the surface that touched the SiC. Note that the arrow in the top left SEM image points to where the SiC substrate was originally before breaking off. This points to a likely mixture of chromium oxides, silica, alumina, and chromium silicides. We predicted previously that chromium silicides may appear in the reaction zones between chromium-containing metals and SiC, and that these may provide some benefit to bonding. Al appeared to have interacted with oxygen that diffused into the In740H, creating inclusions of alumina within the metal. On the air-facing side of the Inconel sample, there appeared to be an enrichment of Nb, Ti, Si, Al, and O. While Nb and Ti were expected, as they are strong oxide formers in In740H, Si and Al were unexpected. One potential explanation for this is that silicon may have diffused to form a silica layer along the outside of the Inconel sample.

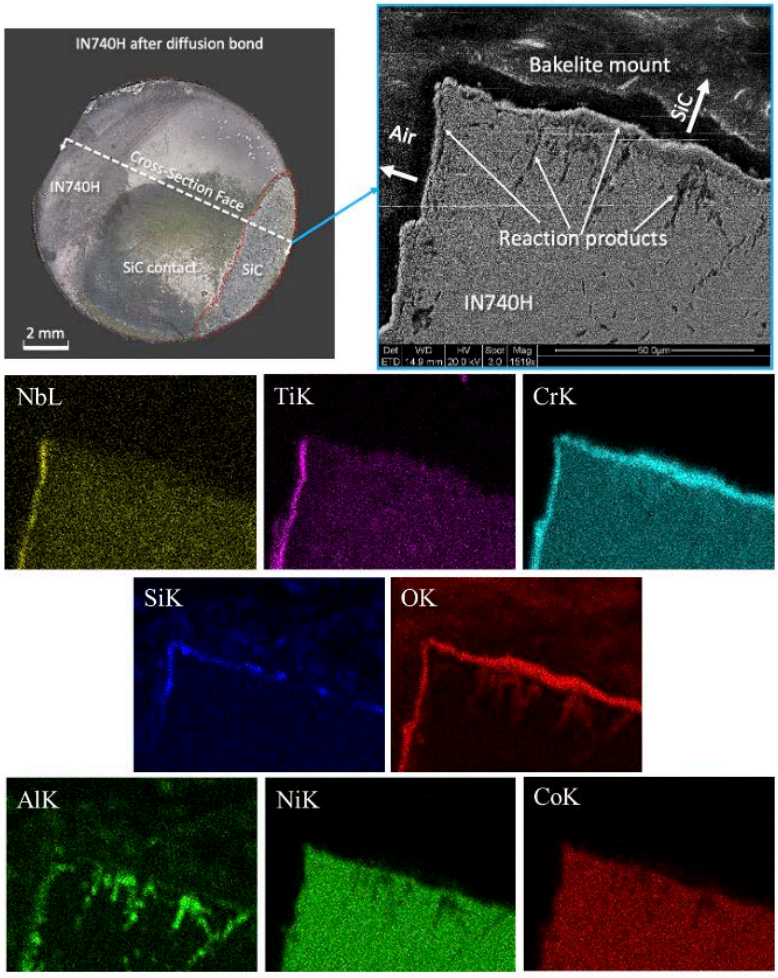

Figure 27. EDS analysis of In740H-to-SiC diffusion bond surface

A similar experimental configuration was used to test a commercial braze (Ticusil from Morgan Braze Alloys). However, there were a few key changes dictated by the joining process. First, rather than being polished to 1 μm, the surfaces of the SiC and the In740H were roughed to 240 grit to increase the bond surface area. Second, a small square (0.25 inch × 0.25 inch) of the Ticusil foil was placed between the two materials. Finally, brazing was performed at 780°C for 20 min in air.

The sample was then furnace-cooled to below 200°C and air-cooled to room temperature. The reported composition of the braze alloy can be seen in Table 10.

Table 10. Composition of Commercial Braze Alloy Ticusil

Composition (wt.%)		
Ag	Cu	Ti
68.8	26.7	4.5

Similar to the diffusion bonding experiment, the cylindrical weight providing the downforce was canted during the brazing experiment, causing the joint to be under uneven pressure. However, the commercial braze was still able to bond well across part of the interface. As can be seen in Figure 28, even with the uneven pressure, there was good wetting between the two surfaces near the middle of the joint, e.g., at the region marked by the blue rectangle. EDS was performed on the region highlighted in blue in Figure 28.

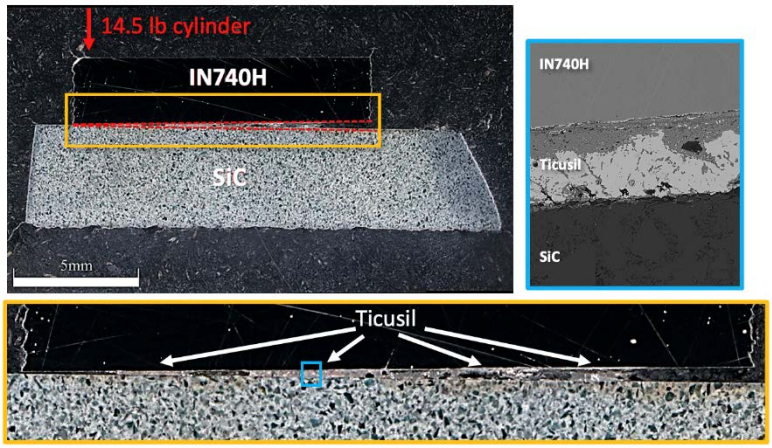

Figure 28. Micrographs showing the joint made during the commercial brazing experiment

As can be seen in Figure 29, there was a clearly defined line where the SiC ended and the transition into braze material began. Aluminum is a minor alloying element in In740H (nominally at 1.35 wt.%), which is likely where most of the Al in the melt region came from, but the small fraction present in the Inconel substrate did not account for the high concentration in the SiC. Based on these results, it appears likely that Al was added to the SiC during manufacturing. Moving left in Figure 29, at the interface between the SiC and the braze, there was a discontinuous layer that appeared to consist of Ti, Ni, Cr, and O. Ti, Ni, and Cr were believed to the be active element facilitating wetting on SiC surface. Among these, Ti was introduced through the braze filler, while Ni and Cr diffused from the Inconel side into the molten pool. The presence of high amounts of oxygen at the SiC/filler interface indicated chromium, nickel, and titanium oxides forming at this surface. These likely formed because this experiment was done in air. Although there were oxides, the probability of Ti and Ni silicides was also high. The discontinuous nature of the Ti/Ni-rich layer indicated that Ag also touched the SiC surface. Ag is not known to produce silicides, and based on the Ellingham diagram for oxides, it is the least likely element in this material to produce oxides. The presence of Ag at the interface was likely a result of SiC being a strong adsorbent for Ag [68]. Moving into the bulk of the braze region, there was phase separation between Cu and Ag. The first was a silver-rich phase. It was lean in all alloying elements except for niobium, which

was relatively homogenous across the entire braze zone. The second was the Cu-rich phase, which contained Ti, Cr, and O. Copper oxide has a lower Gibbs free energy of formation than silver oxide; thus, it can be theorized that the Cu, Cr, and Ti absorbed the atmospheric oxygen that the Ag rejected. The observed trend closely aligns with the results seen in [53,68], where the Ticusil filler separated into two phases upon solidification. The biggest experimental difference between these experiments and those performed in [53,68] was that those experiments were done on SiC-to-SiC joints, whereas this work focused on brazing a metal alloy to SiC. Because one of the substrates was Inconel in this experiment, there was diffusion of Ni, Cr, Co, and Nb into the braze from the metal substrate. Furthermore, Ag appeared to wet the Inconel surface and form an Ag-rich thin line, as seen in Figure 29. High-magnification investigation of each boundary region would improve the understanding of the boundary interactions at both sides of the joint.

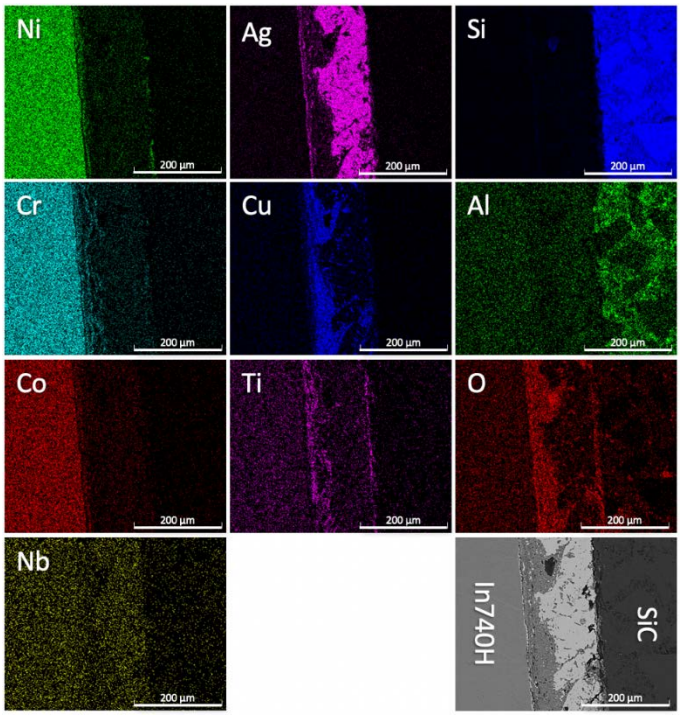

Figure 29. EDS map of the SiC-In740H joint interface using the commercial Ticusil braze

The brazing experiment using the commercial Ticusil filler provided interesting insights into the chemical interactions of the braze material and the two substrates. Based on this work and previous literature searches, it appears that there may be some benefit to adding Ni, Cr, Nb, Ti, Al, and Cu into the MPEA system to aid in wetting and ductility.

2.4.3 Further Validation of MPEA Compositions

The TiCrFeCoNi alloys explored proved to contain significant fractions of brittle secondary phases. To control the fraction of brittle phases, we investigated other MPEA compositions, guided by critical attributes of the compositions and microstructures of commercial, low-temperature braze alloys. For instance, Ticusil braze is effective at low temperatures, but its mechanical properties are not adequate for the target application. However, using these alloys to inform the composition and microstructure of the MPEAs manufactured in this project proved beneficial. Specifically, Ticusil contains less than 4 at.% Ti, which is high enough to make it an effective

active braze yet low enough to prevent embrittlement caused by extensive titanium carbide (TiC) formation. Conversely, the 22 at.% Ti in the TiCrFeCoNi MPEAs tested previously contributed to significant formation of TiC and other brittle intermetallic phases. Therefore, two new MPEAs were evaluated that contained 5 at.% or less Ti. The first MPEA evaluated was a MnFeCoNiCu alloy developed for brazing Ni-based superalloys [67], and the composition was modified by the addition of 1 at. % Ti with a final composition of $Ti_1Mn_{35}Fe_4Co_{20}Ni_{20}Cu_{20}$, labeled as TiMnFeCoNiCu-1. The second was an MPEA previously developed as a trial composition for titanium-to-steel joining [69] with a composition of $Ti_5Mn_{32}Fe_{20}Ni_{35}Cu_8$, labeled as TiMnFeNiCu-1.

The calculated equilibrium diagrams for these two alloys, shown in Figure 30, predicted FCC as the primary stable phase, with low volume fractions of the Ni_3Ti η-phase predicted to form below 700°C for TiMnFeCoNiCu-1 and below 800°C for TiMnFeNiCu-1. The η-phase was identified by its predicted $D0_{24}$ hexagonal close packed (HCP) crystal lattice. Although η is an intermetallic, when it occurs in Ni-superalloy systems, it is generally considered among the more benign intermetallic phases, in contrast to the topologically close-packed phases that are universally detrimental [70]. Both MPEAs demonstrated good ductility and strength in prior forming operations and mechanical testing [69,71], e.g., approximately 38% total elongation and 310-MPa room-temperature yield stresses for TiMnFeNiCu-1. These results indicated promise for both alloys to potentially meet the needs of this project. Therefore, samples of both TiMnFeCoNiCu-1 and TiMnFeNiCu-1 were fabricated and tested to evaluate their compatibility with SiC and In740H.

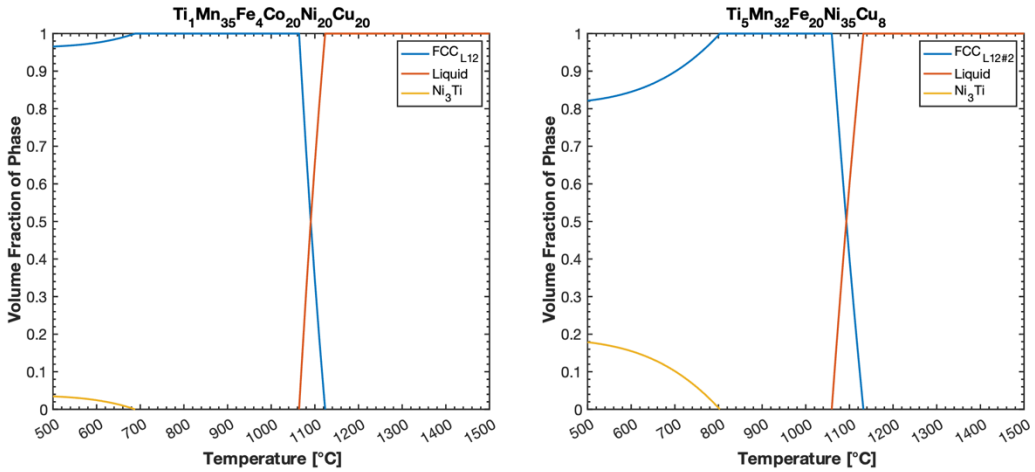

Figure 30. Single-axis equilibrium diagrams for the TiMnFeCoNiCu-1 and TiMnFeNiCu-1 alloys

2.4.3.1 Wettability Tests

We first evaluated the wettability of the two new MPEA compositions on nitride-bonded SiC (NB-SiC). The wettability experiments were performed under vacuum at 1,200°C for 90 minutes to determine whether the alloys, upon melting, would spread across the surface with an acceptable wetting angle and chemically mix with the substrate. As seen in Figure 31, both the TiMnFeNiCoCu-1 and TiMnFeNiCu-1 samples exhibited wetting angles of less than 30°, which is less than the wetting angle of pure copper and pure nickel on SiC and is considered an appropriate wetting angle [72]. An important aspect of the wetting behavior examination was the

interaction zone characterization between the MPEA and SiC substrate. The presence of this interaction region in both cases indicated that both alloys achieved the goal of being active brazing alloys by reacting with the SiC substrate to reduce the surface energy between the ceramic and filler and to promote spreading [73]. However, further microscopic evaluation demonstrated the presence of large, globular dark phases, cracks, and porosity/spattering in the filler, as shown in Figure 31. EDS characterizations determined that the dark regions were silicide and graphite particles, indicating that the chemical interaction with the MPEA filler promoted local dissociation of the SiC near the surface. Some dissociation may be necessary in active brazing to allow the molten filler to wet the surface, but ideally should be controlled to a small fraction within a well-defined bonding region. In the experiments shown in Figure 31, the dissociation was more extensive than the ideal case, as indicated by the large silicide and graphite particles that detached from the substrate and floated in the molten filler pool during the experiment due to their low density. In addition to these second phases, EDS revealed 8–38 at.% of silicon, depending on location, and significant amounts of carbon in the matrix of the MPEA filler materials. This, in combination with the brittle silicide and graphite particles, likely reduced the MPEA ductility and led to the observed cracking. Finally, the porosity and spatter were likely caused by a volatile interaction between the SiC and the MPEA while under vacuum. These observations led to the conclusion that a reduced heat input should be tested to carefully control the reaction between the substrate and filler and achieve a thinner bonding layer. More conservative temperature and time parameters were therefore employed in subsequent vacuum brazing experiments.

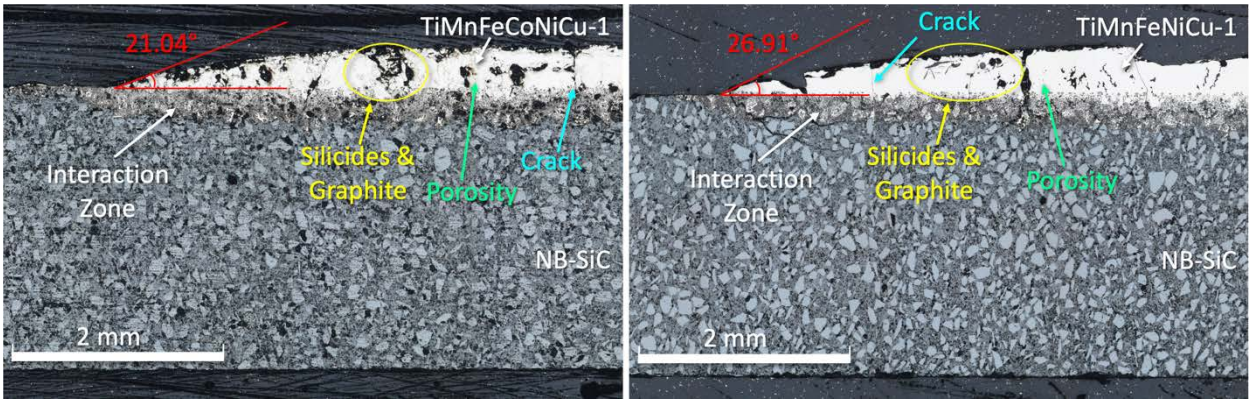

Figure 31. Measured wetting angle for TiMnFeCoNiCu-1 and TiMnFeNiCu-1 on nitride-bonded silicon carbide (NB-SiC)

2.4.3.2 Vacuum Furnace Brazing Experiments

Vacuum furnace brazing was performed with TiMnFeNiCu-1 as the filler between the In740H and nitride-bonded SiC (NB-SiC) substrates. The sample geometry for these experiments can be seen in Figure 32.

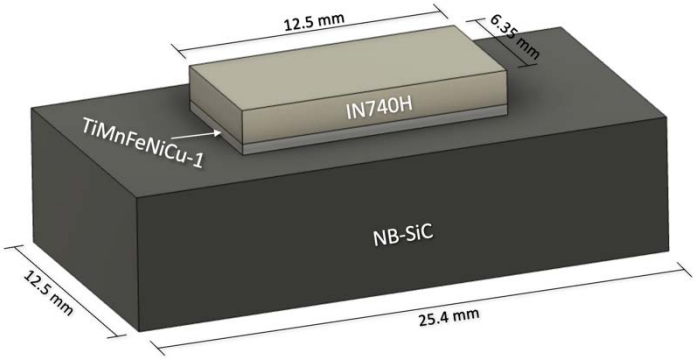

Figure 32. Experimental setup for vacuum brazing experiments

To reduce the extent of reaction product formation, the brazing time was reduced to 45 minutes, and brazing experiments were conducted at both 1,200°C and a reduced temperature of 1,150°C. Upon examination, we determined that similar amounts of silicides, graphite, and pores formed during these experiments, as in the wettability test case, meaning that there was little improvement in the reaction behavior by brazing at lower temperatures and shorter times. Additionally, the brazed samples were fragile during handling, which led to separation of the joint during handling and preparation. This indicated that if the lower heat input had improved the reaction characteristics, it had also become detrimental to the interface bond strength. Although there was difficulty in joining to the SiC, the MPEA and In740H were successfully joined in every case, showing that the MPEA and In740H were compatible.

2.4.3.3 Diffusion Bonding Experiments

The results of the wetting and brazing experiments indicated the need for a joining method with a more careful control of the interaction between the MPEA and SiC. Based on this hypothesis, diffusion bonding, a solid-state joining method, was investigated again, with the MPEA serving as an interlayer to promote a controlled reaction to a certain surface depth in the SiC substrate and facilitate bonding. The parameters for the diffusion bonding trials are summarized in Table 11, and references to each experiment correspond with the names provided in the left-most column. The four key variables studied in this set of experiments were temperature, applied pressure, bonding time, and type of SiC. Pertaining to the lattermost variable, we hypothesized that impurities in the NB-SiC from manufacturing may be a conflating chemical variable to consider, possibly affecting joint integrity. Therefore, we added sintered silicon carbide (S-SiC) with near stoichiometry to the experiment matrix to reduce the chemical complexity in the reaction region. In general, in the experiment matrix, the time variable was adjusted inversely to either temperature or applied pressure to keep the overall extent of diffusion consistent.

Table 11. Summary Table of Diffusion Bonding Experiments

Sample	Ceramic	Filler	Temperature (°C)	Pressure (MPa)	Time (Hr)	Cracked SiC?
DB1	NB-SiC	TiMnFeNiCu-1	1,000	117.7	1	Yes
DB4A	NB-SiC	TiMnFeNiCu-1	1,000	10.1	2	Yes
DB5	S-SiC	TiMnFeNiCu-1	950	10.8	2	Yes
DB7	S-SiC	TiMnFeNiCoCu-1	950	49.5	1	No
DB8	S-SiC	TiMnFeNiCu-1	1,000	99.8	1	Yes
DB3	NB-SiC	TiMnFeNiCu-1	800	8.5	4	No
DB6	NB-SiC	TiMnFeNiCu-1	950	10.0	4	No
DB4b	NB-SiC	N/A	1,000	10.1	2	Yes

Note: All diffusion bonding trials were performed in vacuum.

These experiments achieved more success in generating a dissimilar bond than the furnace brazing experiments, especially when NB-SiC was the ceramic substrate. The most successful trials were DB1 and DB4A (highlighted in green in Table 11), where the samples did not separate during machining steps for characterization purposes. Both DB1 and DB4A used NB-SiC as the ceramic substrate and TiMnFeNiCu-1 as the MPEA filler, and both employed a bonding temperature of 1,000°C. The difference between these two tests was primarily in the applied uniaxial pressure, which was 10 MPa for DB4A and 118 MPa for DB1. With a high bonding pressure, DB1 exhibited significant SiC substrate cracking, which can be seen in Figure 33(a), likely resulting from the high applied pressure, or a higher-than-optimal loading rate during the application of pressure to the sample, which is another variable to consider. However, there was a region in the center of the DB1 sample that had a uniform, thin reaction interface with the MPEA without significant dissociated particles, as seen in Figure 33(b). This sample warranted additional characterization and indicated some initial promise for MPEA-facilitated diffusion bonding as a technique, with further refinement of process parameters required. In DB4A, the materials were successfully joined, but during cutting and grinding for examination, there was a significant loss of material in the interfacial reaction region between the NB-SiC and the MPEA filler. This created a crevasse between the two materials approximately 200 μm wide and 90 μm deep, as can be seen in Figure 34. It is possible that the optimal bonding pressure using NB-SiC as the ceramic substrate and TiMnFeNiCu-1 as the MPEA interlayer lay between the values used in DB4A and DB1.

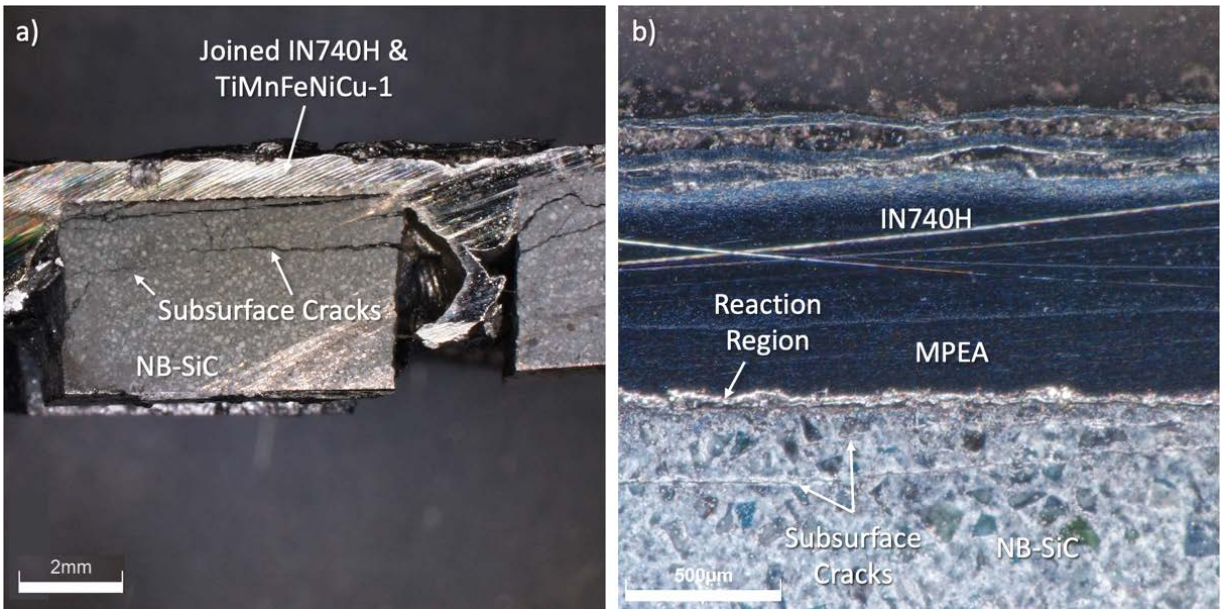

Figure 33. (a) Unpolished macrograph of DB1 cross section showing prolific cracking, and (b) high-magnification image of the well-bonded section in DB1

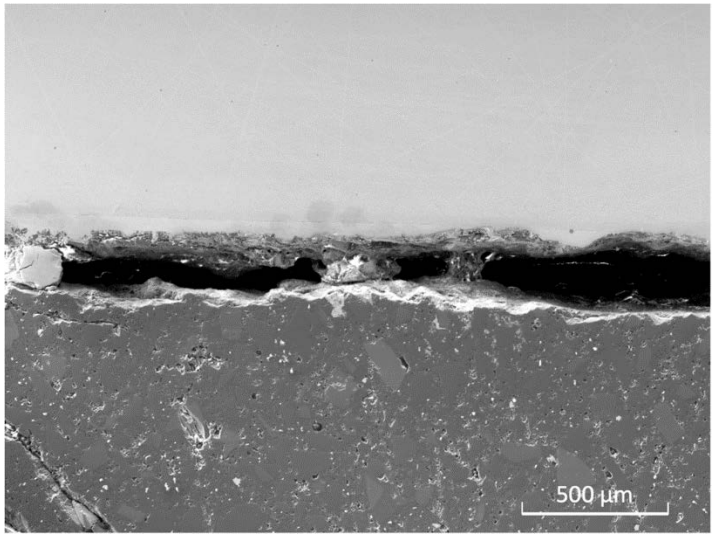

Figure 34. Micrograph showing the material loss at the DB4A reaction zone during sample preparation

For experiments employing S-SiC (highlighted in yellow in Table 11), no satisfactory bonding between MPEA and S-SiC was observed. For instance, experiment DB5 was performed using S-SiC exposed to 950°C under a 10.8 MPa load. In this test, the MPEA and In740H components bonded, but the MPEA did not fully join to the S-SiC. Upon examination of the resulting morphology of the reaction region, it appeared that the reaction product, rather than forming a continuous layer, created globules of nonwetting liquid that beaded up on the surface of the S-SiC substrate, indicated by the rounded, fragmented morphology of the material, as seen in Figure 35. In addition, the DB4B case represented a direct bonding experiment between In740H and NB-SiC, in which the bond was too weak to survive the cutting process for metallurgical characterization.

All diffusion bonding experiments (except DB3) were performed 50°C–100°C below the predicted MPEA solidus temperature of about 1,050°C. Characterization of the ceramic-to-MPEA bond interface indicated that there was likely a eutectic reaction resulting from the diffusion of silicon and carbon into the MPEA, resulting in local melting. Further characterization of the NB-SiC/MPEA interfaces in DB4A and DB1, and the S-SiC/MPEA interfaces in DB8, should be performed to characterize the eutectic microconstituent and local melting in order to understand the difference in bonding formation between the two different ceramic substrates.

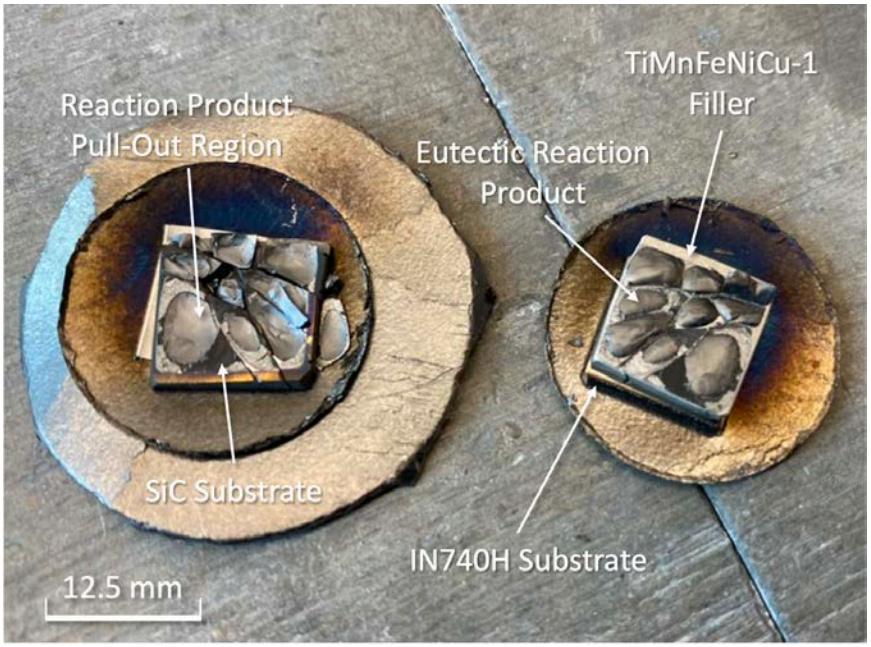

Figure 35. DB5 reaction product and substrate after diffusion bonding

Iterative single-axis equilibrium calculations were run in Thermo-Calc's TC-Python with increasing, equimolar amounts of silicon and carbon introduced to the TiMnFeNiCu-1 to help understand the reaction at the ceramic-to-MPEA interface. The equimolar constraint assumed that, once liquid formed, the erosion process would introduce silicon and carbon from the SiC in approximately their stoichiometric ratio, despite the fact that carbon, as an interstitial element, diffuses faster than silicon through solid metal. Figure 36 shows the plot of the calculated solidus temperature as a function of SiC dilution, where the MPEA composition was diluted by the equiatomic diffusion of silicon and carbon. This plot shows that initially, the solidus temperature increased to 1,131°C up to 8 mol.% dilution and reduced beyond this point to 941°C beyond 40 mol.% dilution. Based on this calculation, liquation at the ceramic/MPEA interface should be expected to occur during diffusion bonding above 940°C. Hence, the explanation of local melting in the DB5 experiment, which occurred at 950°C, was in part validated by this calculation.

The collective results shown in Table 11 were a starting point to guide future tuning of pressure and hold time. Regarding pressure, the 100+ MPa tests induced significant plastic deformation in the In740H metal workpiece and MPEA interlayer. This is unsurprising because extrapolating the yield stress curve from [47] indicates that the expected yield strength of In740H is only about 70 MPa. Plastic deformation of the metal substrate during diffusion bonding is undesirable for the purpose of joint geometry control. More importantly, the geometry change of the metal pieces

likely led to a bending moment in the SiC, which was potentially the main reason for the observed cracking in the SiC substrate of DB1 and DB8. To both avoid plastic deformation in the metal substrate and reduce cracking of the ceramic substrate, the bonding pressure should be limited to no more than 70 MPa [47]. We used the proposed upper bounds on pressure and equilibrium phase diagram calculations to guide future process optimization. In previous experiments, the maximum hold time for joining was 4 hours. If the bonding temperature were held below the solidus temperature with dilution of Si and C, the bonding process would rely primarily on solid-state diffusion, and therefore the time necessary for joining would likely increase significantly, as the diffusivity governing the extent of interdiffusion between the MPEA and SiC scales dramatically with temperature. Although the literature was vague on appropriate hold times for diffusion bonding to SiC, it has been reported that diffusion bonding times can vary from minutes to several hours [55]. Next, we evaluated experiments with longer hold times at low temperatures to understand their impacts on the dissimilar joint interface.

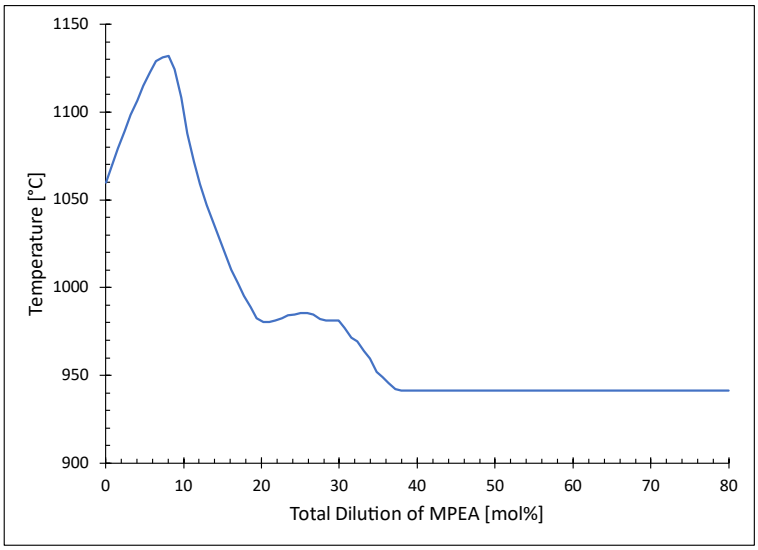

Figure 36. Plot of the effect of combined equimolar silicon and carbon diffusion on the solidus temperature of TiMnFeNiCu-1

2.4.3.4 Strategies for Reducing Thermal Residual Stress

Residual stresses were hypothesized to play a significant role in the observed cracking on the SiC side of diffusion-bonded samples. Mounting and polishing the NB-SiC substrate revealed a large U-shaped crack that propagated from one edge of the reaction layer to the other through the bulk of the NB-SiC, which can be seen in Figure 37. This crack was consistent with thermal residual stresses in the ceramic substrate. Suganuma et al. [74] determined that along flat bond interfaces between metal and ceramic, like those created during this process, compressive residual stresses formed in the center of the sample near the top (near the filler material) [74]. Toward the edges of the sample, these transitioned into tensile stresses, which provided the mechanism for crack opening and propagation, as illustrated in Figure 37.

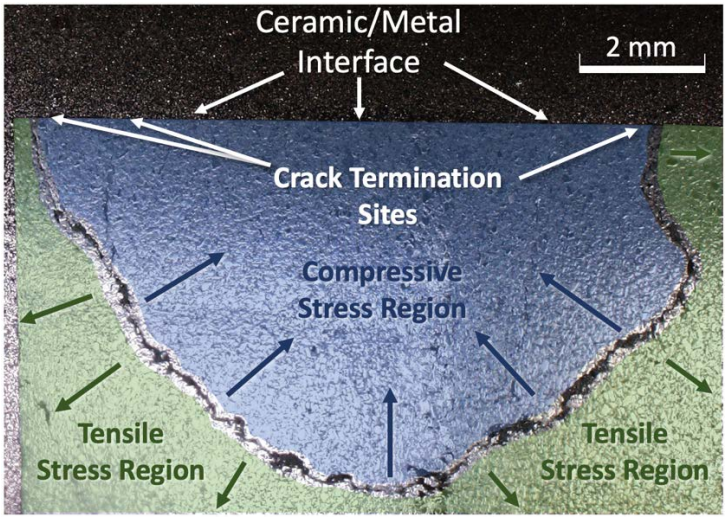

Figure 37. U-shaped crack in the NB-SiC substrate after bonding, showing residual stress regions

As a strategy to mitigate the cracking in the SiC substrate observed during previous diffusion bonding trials, we implemented a slow cooling rate with the goal of minimizing the formation of high residual stresses as the samples were cooling. These experiments followed the heating and cooling schedule in Figure 38, which had intermediate holds at 800°C and 500°C. The 800°C hold was selected because it is above the solvus for carbide formation in the In740H yet below the solidus temperature. The second hold was at 500°C to provide stress relief after the carbides had finished forming and the stress had increased due to the CTE mismatch. The cooling rate was set to 0.7°C/min (or about 42°C/hr) until the samples reached 200°C, when they were then furnace-cooled to room temperature.

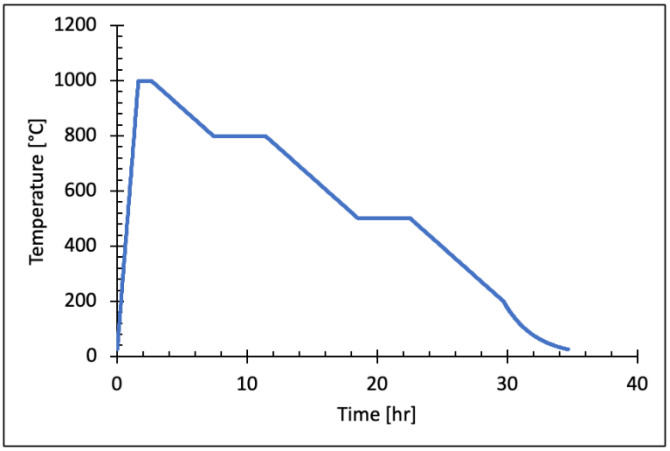

Figure 38. Time-temperature curve for slow cooling stress relief experiments

These experiments included stress relief steps that were not performed previously. However, the additional time at an elevated temperature increased interdiffusion between the materials and likely contributed to microstructural evolution (to be discussed in Section 2.4.3.5). Measuring residual stress in a complex, multi-material structure required advanced characterization techniques; however, cracking still occurred in some of the slow-cooled samples, indicating that the stress relieved during these experiments was insufficient.

Literature reports on SiC-to-metal bonding discussed that, because of the brittle nature of the reaction layer and its planar growth into the NB-SiC substrate, when cracks began to form, there was little driving force to stop their propagation. Wang et al. [75] explored the idea of using a carbon-fiber-reinforced SiC (C-SiC) during brazing to GH4169 Ni superalloy, which helped their bond characteristics in a few ways. First, when the braze filler bonded to the SiC substrate, it reacted with and incorporated the matrix SiC, leaving the carbon fibers essentially unchanged. This resulted in a large portion of the brittle intermetallic reaction products being in regions bounded by carbon fibers, which ultimately interrupted crack propagation at the interface, as can be seen in Reference [75]. Second, they observed that the presence of the carbon fibers increased the concentration of TiC that formed in the reaction zone, where the Ti-rich filler preferentially bonded to the pure carbon rather than continuing to penetrate the SiC. This was beneficial because TiC provides a much stronger bond than $TiSi_2$. Third, the fiber reinforcement in the ceramic substrate increased the compliance of the bulk substrate material, which made it less susceptible to cracking. We then used a C-SiC composite as the ceramic substrate to validate the effectiveness of ceramic fibers on cracking mitigation with an MPEA interlayer. The C-SiC composite was provided by the Palo Alto Research Center (PARC).

2.4.3.5 Characterization of Reaction Products

We used EDS and SEM to assess microstructural evolution and infer phase constituents in the slow-cooled diffusion-bonded samples between NB-SiC and the MPEA interlayer after bonding. Although EDS provides a good approximation of the phases present, for exact determinations of the phase constituents, XRD is recommended. Figure 39 presents the EDS mapping results in a cracked bonding location. Multiple microstructural features were identified on the MPEA side of the reaction region, where one phase was highly enriched in silicon and nickel, while the other phase was enriched with cobalt, iron, and copper.

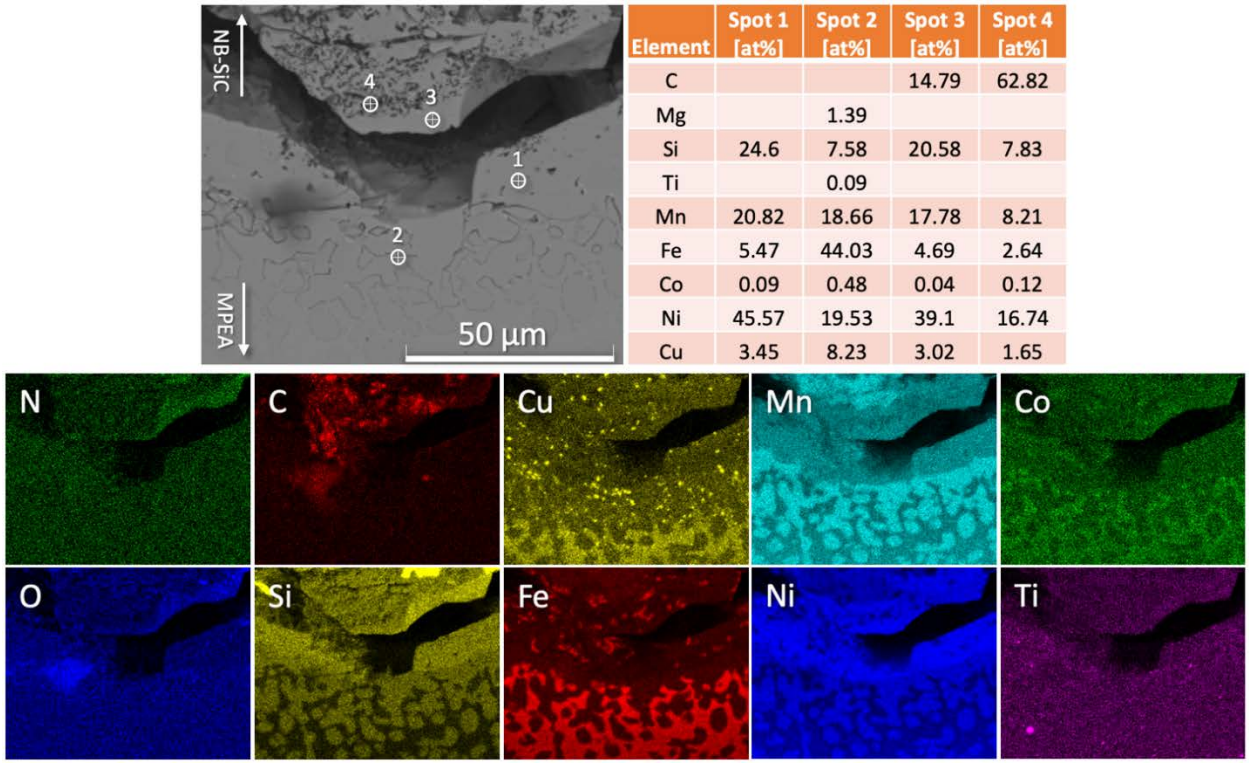

Element	Spot 1 [at%]	Spot 2 [at%]	Spot 3 [at%]	Spot 4 [at%]
C			14.79	62.82
Mg		1.39		
Si	24.6	7.58	20.58	7.83
Ti		0.09		
Mn	20.82	18.66	17.78	8.21
Fe	5.47	44.03	4.69	2.64
Co	0.09	0.48	0.04	0.12
Ni	45.57	19.53	39.1	16.74
Cu	3.45	8.23	3.02	1.65

Figure 39. SEM and EDS analysis of the reaction zone between the NB-SiC and TiMnFeNiCu MPEA

Moving further toward the NB-SiC side of the interaction region, it appears that Fe-based silicides were present, which likely led to the formation of the C-rich islands, as shown in the high-magnification EDS analysis in Figure 40. In addition, Figure 40 shows the presence of Cu-rich islands. Of the MPEA constituents, Cu is the most prone to exhibiting phase separation due to its positive binary enthalpy of mixing with many of the other elements [76]. Furthermore, at lower magnification (Figure 39), an Ni- and Si-rich region formed a layer between the two-phase region on the MPEA side and the remainder of the reaction zone. The enrichment of Ni and Si in this region, as well as the semi-quantified results of EDS Spot 1, strongly suggested that Ni_2Si was a potential dominant phase in this region. While MnSi or $MnSi_2$ were also likely present, the high Ni and Si concentrations in nearly stoichiometric proportions at this point suggested the formation of a significant amount of Ni_2Si. Figure 39 showed that the aforementioned graphite islands become larger and more numerous in the vicinity of the SiC. The presence of both carbon- and Si-rich phases in the interaction zone was evidence of some dissociation of SiC during the bonding process. Such dissociation was inevitable, but the Ti present in the MPEA interlayer was intended to bond with the free Si and C, preventing the formation of less stable silicide and carbide phases. In this way, Ti acted as the active element in the interlayer.

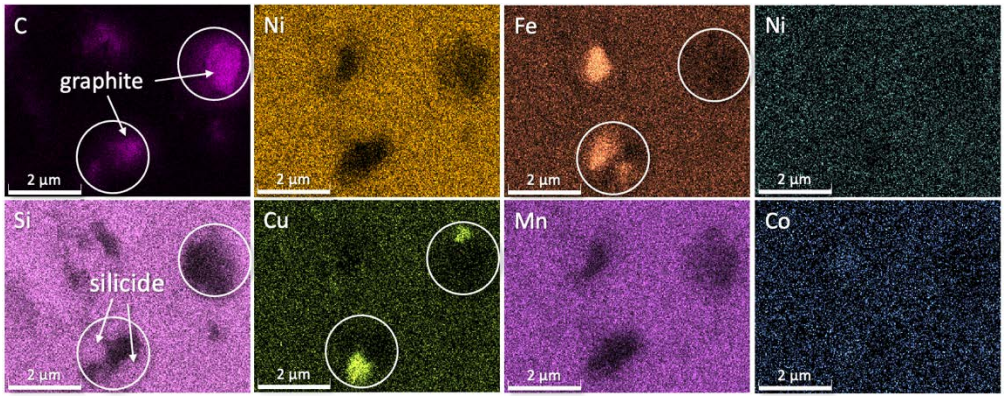

Figure 40. High-magnification EDS maps of the secondary phases in the reaction zone between the NB-SiC and MPEA

In experiments performed by Wang et al. [75], Ti formed a continuous layer of carbides and silicides between the filler material and the ceramic substrate, promoting bonding. In these experiments, the filler contained a large concentration of Ti (15 at.%), which enabled the formation of a continuous layer quickly during the joining process. The MPEA in our work contains 5 at.% Ti. Based on earlier work with commercial braze fillers, 5 at.% Ti should be sufficient to react with the SiC substrate in a manner consistent with that observed by Wang et al., yet low enough of a concentration to prevent the formation of brittle phases in the MPEA bulk. However, as discussed in the following section, the vacuum induction melting process used to fabricate the MPEA resulted in an experimental composition that was deficient in Ti, which may have critically influenced the observed microstructural evolution.

2.4.3.6 Casting Improvements and Crucible Material Exploration

To enable the best environmental control in MPEA fabrication, we selected vacuum induction melting as the casting process. We used an Indutherm MC20V tilt-casting unit, for which the only commercially available, geometrically compatible crucible was a silica-alumina blend in a ratio of 2:1. Because silica is a substantially less stable oxide than TiO_2 [77], extensive alloy/crucible reaction occurred during the fabrication melts, resulting in significant deviation from the designed composition as determined by X-ray fluorescence (XRF). This is reflected in Table 12.

Table 12. Comparison of As-Designed and As-Fabricated Composition of the MPEA Filler Samples Using a Vacuum Induction Melting Furnace With an Aluminosilicate Crucible

MPEA	Composition (at.%)						
	Al	Si	Ti	Mn	Fe	Ni	Cu
As-designed	0	0	5	32	20	35	8
As-cast	2.3	5.3	0.6	28.9	18.2	36.2	8.6

As indicated by the approximate resulting composition measured by XRF, Ti and Mn were lost to slag formation, whereas Si and Al from the aluminosilicate crucible material were incorporated into the melt. This led to a final composition with 5.30 at.% Si and 2.25 at.% Al before bonding. Additionally, the Mn concentrations were reduced from 32 at.% to 28.90 at.%, and the Ti concentration was reduced from 5 at.% to 0.58 at.%.

As Ti was intended to perform the critical function of stabilizing silicide and carbide phases at the bonding interface, this tenfold reduction from the designed Ti concentration may have heavily influenced the effectuation of bonding. In the low-magnification EDS maps in Figure 39, it did not appear that Ti performed its function. However, at high magnifications, like those in Figure 41, Ti can be seen along the interface, forming a semi-continuous line of compounds. This indicated that if the final Ti concentration in the MPEA can be raised to near the design intent, much of the detrimental diffusion and resulting embrittlement could be mitigated. Therefore, we undertook a crucible compatibility study by melting this MPEA and similar alloys in a vacuum furnace on alternative ceramic substrates, including several grades of alumina and zirconia. Minimal interaction was observed when melting the MPEA on a slip-castable zirconia grade (zirconia is known to be more stable than titanium oxide [77]). A zirconia supplier produced slip-cast zirconia crucibles that were geometrically compatible with the casting unit, and all subsequent MPEA fabrication was done using these crucibles.

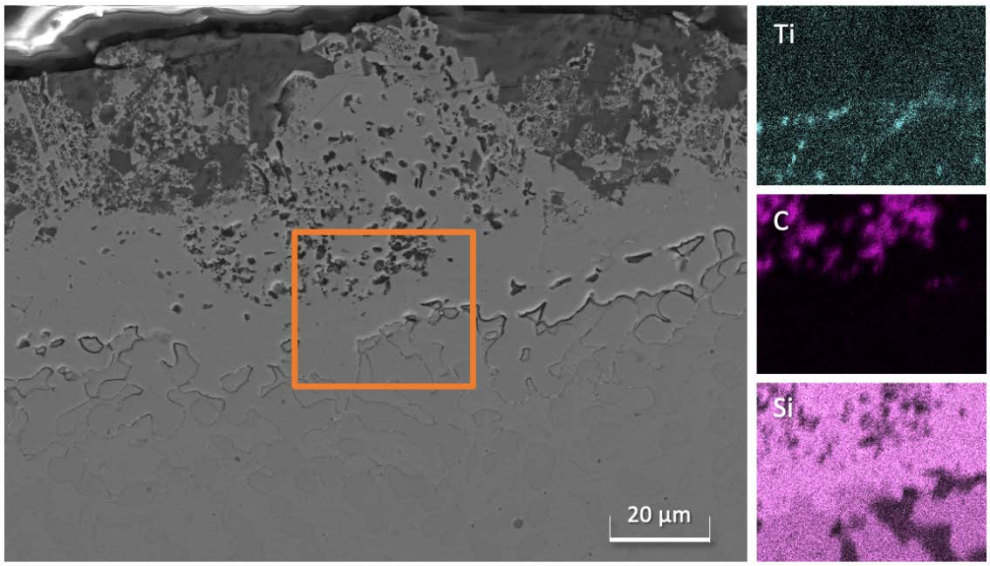

Figure 41. Reaction zone between NB-SiC and TiMnFeNiCu MPEA that contains portions of a Ti-rich boundary layer

2.4.3.7 C-SiC to In740H Diffusion Bonding Using Arc-Cast MPEA Filler

After arc casting, the TiMnFeNiCu MPEA filler in a zirconia crucible matched the design intent; the overall composition was verified via XRF (Table 13). Next, a diffusion bonding experiment using the C-SiC substrate was performed with the new batch of filler material. In these tests, the samples were oriented as seen in Figure 42 in a hot press and subjected to a slow cooling cycle under a uniaxial load, as discussed previously. The pressure and temperature (plotted in Figure 43) peaked simultaneously, at 50 MPa and 1,000°C, respectively, and the pressure was released to the resting load of 11 MPa once the temperature had decreased to 900°C.

Table 13. Comparison of As-Designed and As-Fabricated Composition of the MPEA Filler Samples via Arc-Casting With a Zirconia Crucible

MPEA	Composition (at.%)				
	Ti	Mn	Fe	Ni	Cu
As-designed	5	32	20	35	8
As-cast	4.92	33.9	19.4	34.0	7.8

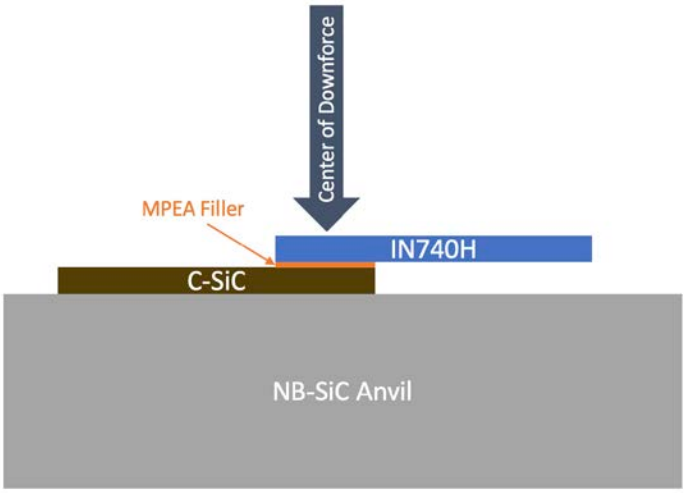

Figure 42. Schematic of the experimental setup for diffusion bonding between C-SiC and In740H

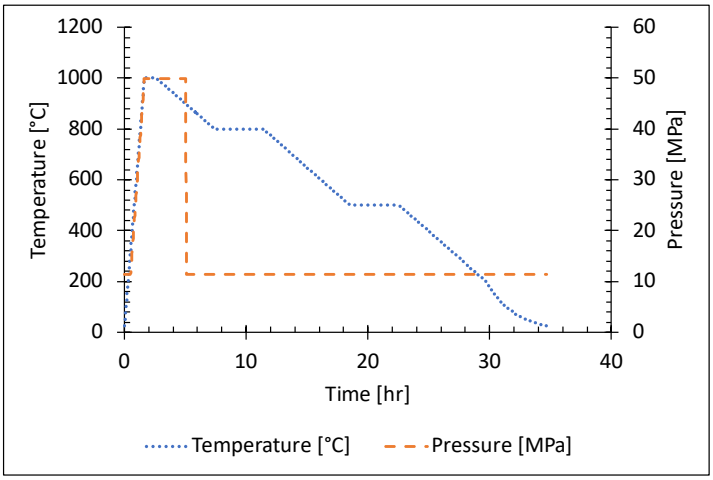

Figure 43. Temperature and pressure used during diffusion bonding between C-SiC and In740H

After removing the diffusion bonding sample from the hot press, we found that the sample had separated. However, it appeared that some TiMnFeNiCu had bonded to the C-SiC. The separation occurred primarily within the C-SiC substrate. As shown in Figure 44, the C-SiC around the bond region separated into three pieces. The first piece of C-SiC adhered to the TiMnFeNiCu filler and was attached to the In740H through the bond after separation. The second piece of C-SiC adhered to the Grafoil layer that was used to protect the fixturing during the experiment. The third piece

adhered to the NB-SiC anvil and punched through the Grafoil layer during joining. This indicated that the C-SiC delaminated at some point during the joining process (discussed later).

Figure 44. In740H-MPEA-(C-SiC) sample after diffusion bonding at 1,000°C with 50 MPa of uniaxial pressure

Following the experiment, the joined section was mounted and polished for metallographic and chemical analysis. Microscopy revealed distinct differences between the joint made with C-SiC joint and NB-SiC when compared to joints made previously. First, there was significantly less cracking at the interface between the MPEA and the C-SiC than was seen in the NB-SiC. Second, the reaction region was measured to be approximately 20 μm thick, as seen in Figure 45, in comparison to the nearly 50-μm-thick reaction region seen in previous experiments. Although there were promising results in the joint, it appeared that the C-SiC had not been fully densified before joining. This was evidenced by the flaky nature of the as-received material and by some areas within the C-SiC holding large amounts of mounting resin, which indicated large voids and potential porosities within the C-SiC. These voids may have been induced during the joining process, but they could also be indications of defects in the C-SiC microstructure during manufacturing.

When examining the chemistry of the joint via EDS mapping (Figure 45), we observed that the primary matrix in the C-SiC was highly Si-rich. This is consistent with a common processing path for making C-SiC, which is to infiltrate the carbon-fiber layers with pure Si. The Si interacts with the carbon fibers during the sintering process, producing a SiC matrix. As there were areas of nearly no carbon between some of the fibers in the C map in Figure 45, the sintering steps may not have fully transformed the Si to SiC as intended, leaving excess free Si in the system. Significant oxygen was observed in the C-SiC material between the fibers and in the interaction region. Not only was there significant oxygen in the C-SiC substrate, but it was also often enriched in the regions that overlapped with Si but did not overlap with carbon. This may indicate the presence of either silica in the system or voids housing oxygen-bearing species at these locations. Further analysis would be necessary to make this determination.

Within the reaction region, we saw that a continuous Ti-rich boundary layer formed adjacent to the MPEA. This, combined with the observation of the thinner reaction layer, supports the hypothesis that enough Ti in the system (i.e., when the fabricated composition matches the design intent using the zirconia crucible) will serve as an active element facilitating the controlled dissociation of SiC and will thus promote bonding. Ideally, this reaction would form a thin boundary zone to reduce the reaction of SiC with other MPEA constituents. The results in Figure 45 indicated that the Ti in the system may have partially served this function, as Mn, Ni, Cu, and Fe present in the reaction region were observed to be at a reduced level compared to previous experiments using vacuum induction casted MPEA with a much lower Ti content.

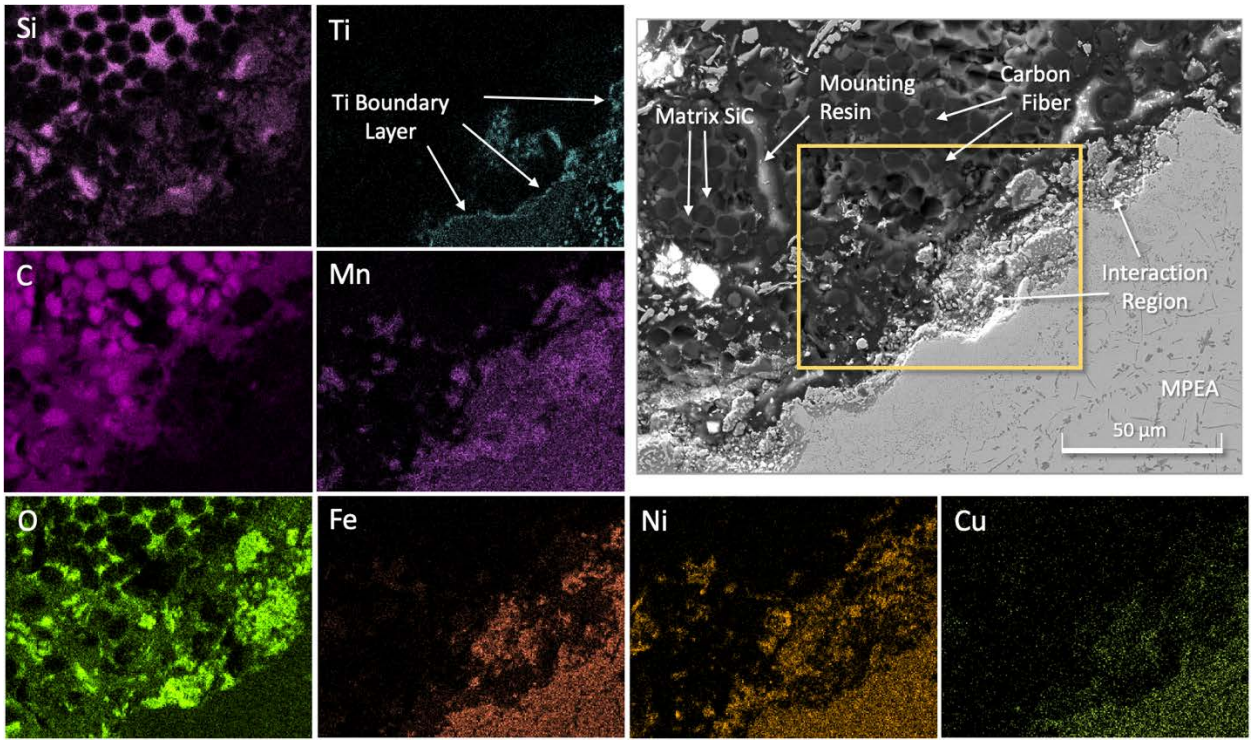

Figure 45. SEM micrograph and EDS maps of the interface between the MPEA and C-SiC

The C-SiC substrate appeared to be extremely weak under compression and failed by delamination, as previously mentioned. The morphology of the broken C-SiC after diffusion bonding showed that it was crushed under the pressure of the press and delaminated between the carbon-fiber layers. The reasoning is likely threefold. First, from microscopy and communication with the supplier (PARC), we learned that the initial C-SiC samples were only densified to approximately 70%. Second, the fiber fraction in these samples was between 50% and 60%, which is much higher than the desired fraction (e.g., <20% to achieve a higher-toughness C-SiC). In the direction normal to the fibers, the primary structural component was the SiC matrix. The lack of matrix SiC reduced the ability of the sample to bear loads in this direction and increased the likelihood of delamination. Finally, EDS mapping showed that the processing conditions may have led to a high fraction of silica and/or void networks trapping oxygen-bearing species in the system after sintering, which likely degraded the mechanical performance. Hence, we suggest that the ideal C-SiC composite material should contain less than 30 vol.% of carbon fibers, achieve >85% densification, and minimize the presence of oxygen in the system during sintering as much as

possible. Under these conditions, it is likely that the fiber count will still be high enough to improve the joining characteristics by increasing the relative TiC fraction and interrupting interface crack propagation, while also containing sufficient matrix SiC to withstand the forces applied during joining in the direction normal to the fibers.

2.4.3.8 NB-SiC and C-SiC to In740H Vacuum Brazing Using Arc-Cast MPEA Filler

In addition to diffusion bonding, vacuum brazing trials were also performed with the arc-cast MPEA filler. Thermodynamics calculation through Thermo-Calc in Figure 46 predicted the liquidus temperature of the TiMnFeNiCu alloy to be 1,138°C. Hence, the brazing temperature was set to 1,200°C and held for 1 hour before furnace cooling. Both NB-SiC and C-SiC were tested for vacuum brazing experiments using the new arc-cast MPEA with the desired Ti content.

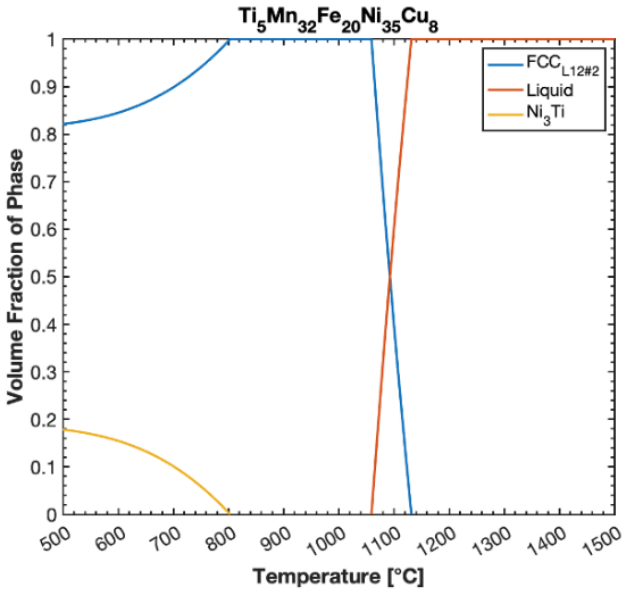

Figure 46. Single-axis equilibrium diagram for the TiMnFeNiCu filler

Initially, it appeared that the In740H-MPEA-(C-SiC) joint had successfully bonded after brazing, as can be seen in Figure 47(a). However, after further examination, we determined that it was mostly unbonded, with a small bonded section near the end of the brazed area. On the same end, a small amount of the braze filler had escaped the joint interspace and bonded with the graphite fixturing on which the sample was placed. Additionally, the MPEA did not appear to have spread significantly in the joint. This was shown by the fact that the final braze filler shape, while slightly deformed along the edges, was essentially the same as the initial foil, as outlined in Figure 47(b). Finally, in the unreacted regions of the filler, there was dark discoloration on the surface, which was most likely a signature of carburization from the C-SiC substrate.

Overall, because there was no force applied to the sample, the MPEA foil may not have made sufficient contact with the surface of the C-SiC to initiate reaction across most of the interface. However, at the end, where the MPEA escaped the joint interspace and bonded to the graphite, it was held fast to the surface by the graphite, thus creating a local anchoring effect and facilitating a bond at that end of the filler. Also, because the MPEA did not spread well, it likely did not fully

melt, or if it did, it was not superheated enough to allow sufficient flow. This means that the melting point of this filler was likely higher than predicted by the Thermo-Calc simulations, and the brazing temperature needed to be reevaluated after measurement of its true melting range by differential scanning calorimetry (DSC).

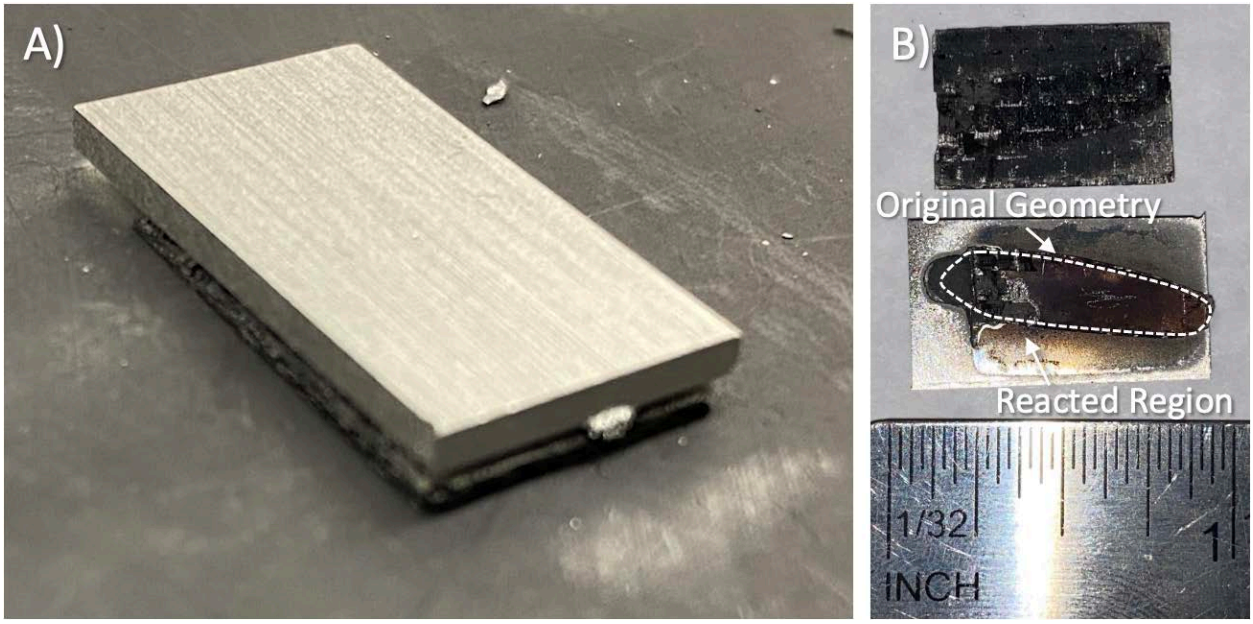

Figure 47. In740H-MPEA-(C-SiC) braze results (a) directly after brazing and (b) after separation

In the In740H-MPEA-(NB-SiC) case, the In740H and NB-SiC substrates were found to be completely and violently separated during the brazing process. However, on the surfaces of both substrates, there were reaction products and evidence of bonding. The ceramic substrate was found in multiple pieces atop the graphite fixturing, sitting askew from where it was originally. The In740H was found on the back of the furnace, a distance of roughly 8 inches from the staging position, and was lying on the graphite insulation outside the hot zone. We believe that the explosion was caused by gas rapidly escaping from the joint while the filler was either fully or nearly molten. This is evidenced in Figure 48 by the residual ejected filler material on the surface of the NB-SiC. There are two hypotheses for where this gas may have originated. The first is that a pore (or multiple pores) in the NB-SiC may have been disturbed by the interaction of the MPEA with the NB-SiC, which could have significantly weakened the material surrounding the pore. The trapped gas bubble would have been under pressure to escape because of the high vacuum conditions in the chamber and could have found the path of least resistance to the surface of the NB-SiC workpiece and then through the soft MPEA. The second and more probable hypothesis is that this entrapped gas originated from a volatile reaction between elements from the NB-SiC and O contaminant in the arc-melted MPEA and NB-SiC, which would have caused the nucleation of multiple gas bubbles (e.g., CO_2). These then coalesced and caused the pressure in the joint interspace to build up, eventually leading to catastrophic separation of the workpieces. Previous brazing experiments employed vacuum induction melted filler with lower interstitial N and O content, which may explain why this explosive phenomenon was newly presented in this experiment.

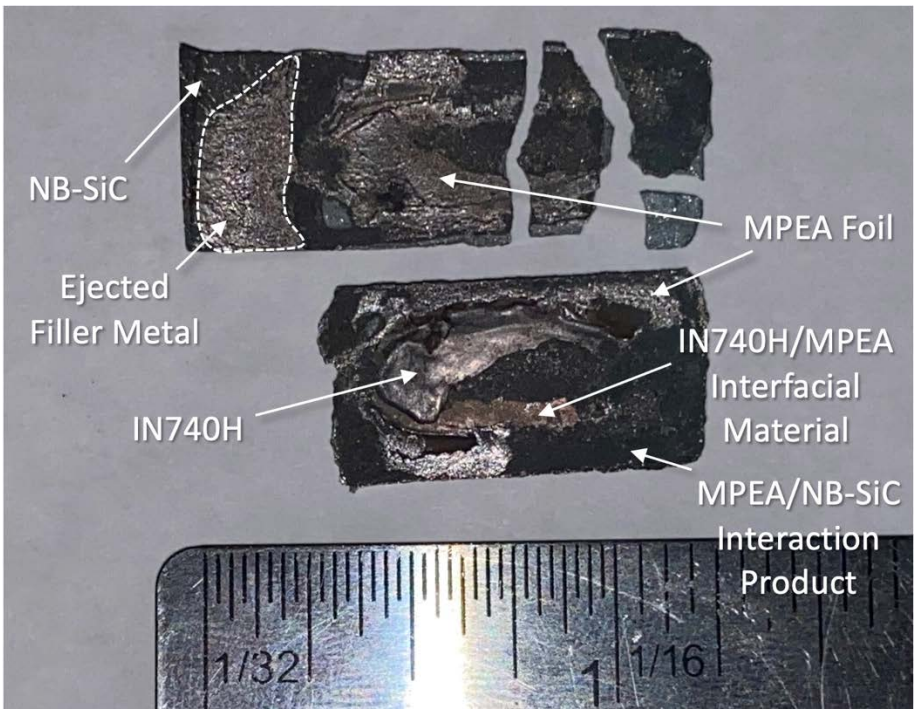

Figure 48. The retrieved In740H-MPEA-(NB-SiC) braze sample after brazing

The brazing experiment and previous work using the NB-SiC showed that this ceramic substrate, while better than sintered SiC, was also not a viable option for a ceramic substrate using the current MPEA composition as the filler. The brittle nature of all the interaction layers produced, the previously discussed presence of cracks in the bulk material, and the potential contribution of nitrogen to the system provided sufficient evidence that the focus of future work should not be on joining to NB-SiC.

2.4.3.9 MPEA Melting Point by Differential Scanning Calorimetry

Based on the braze results in the previous section, the TiMnFeNiCu MPEA filler's melting point was suspected to be higher than the predicted value from thermodynamic calculations. We performed DSC to experimentally determine the MPEA's melting point. The thermodynamically predicted solidus and liquidus were 1,060°C and 1,138°C, respectively. Experimentally, the solidus and liquidus were found to be 1,141°C and 1,153°C, respectively, as shown in Figure 49. These values were critical to designing the brazing experiment with an appropriate superheat.

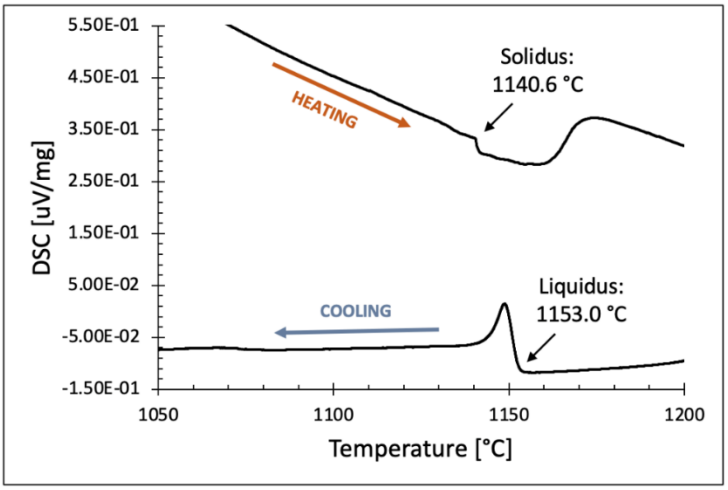

Figure 49. Solidus and liquidus of TiMnFeNiCu MPEA filler as determined by DSC

2.4.3.10 Further Improvement of MPEA Fabrication via Vacuum Furnace Casting

Vacuum furnace casting was performed to achieve very low levels of interstitial contamination in the filler heats. For this process, the raw materials were placed in a covered zirconia crucible, then heated to 1,250°C and furnace cooled, all under high vacuum (10^{-4}–10^{-5} torr). Although 1,250°C was below the melting temperature of some of the individual constituents, the degree of partial melting was sufficient to promote incorporation of all components into the alloy. The well-mixed composition was fully molten at 1,250°C. To promote homogeneity, the resolidified sample was flipped and remelted two additional times under identical conditions. After the three melting cycles, the sample was sectioned and validated for chemical accuracy using XRF. The as-designed and as-cast compositions are compared in Table 14, and no component deviated from the design composition by more than 1%, which is within the desired tolerance based on thermodynamic calculations.

Table 14. Comparison of As-Designed and As-Fabricated Composition of the MPEA Filler Samples via Vacuum Furnace Casting With a Zirconia Crucible

MPEA	Composition (at.%)				
	Ti	Mn	Fe	Ni	Cu
As-designed	5	32	20	35	8
As-cast	5.0	31.7	20.2	35.1	8.0

2.4.4 MPEA Metal Matrix Composites for Stress Mitigation

2.4.4.1 C-SiC Braze Experiments and Thermal Stress Mitigation Strategy

The vacuum furnace cast MPEA filler was tested on >90% dense C-SiC substrate. To mitigate the thermal stresses induced by the thermal expansion mismatch in the In740H/MPEA/SiC sandwich structure when cooling the braze, the project team investigated adding inert ceramic particles to the metallic filler with an increasing volume ratio to enable a gradient in the effective CTE of the metallic filler. It is widely accepted that composite materials generally exhibit properties proportional to the relative fraction of each component. Therefore, adding a low-CTE ceramic powder into the metal filler to create a metal matrix composite (MMC) should reduce the effective CTE of the filler proportional to the amount of powder added. Tungsten carbide (WC) was first

considered because of its low CTE and its success as a cemented carbide MMC for use in industrial cutting tools [78]. TiC fine powders (<4 μm) were also considered for initial trials, because TiC is a desirable reaction product between the MPEA and C-SiC to effectuate joining, even though TiC has a slightly higher CTE (7.7×10^{-6} K^{-1}) than that of WC (5.5×10^{-6} K^{-1}).

The selected carbide powders were first mixed with a polymeric braze binder to keep them in place on the surface. The binder/carbide paste was then applied with a spatula onto the surface of the C-SiC substrate, and the MPEA filler foil (~200-μm thickness) was placed directly on top of the paste. As an organic compound, the binder was formulated such that during the heating process, it would evaporate and leave minimal residue. A schematic of the joint sample before and after joining is given in Figure 50. As shown, the setup targeted a uniform MMC layer after melting by allowing the molten MPEA to flow downward and incorporate the TiC particles. For a control specimen, we ran an identical joint sample simultaneously without TiC particles added.

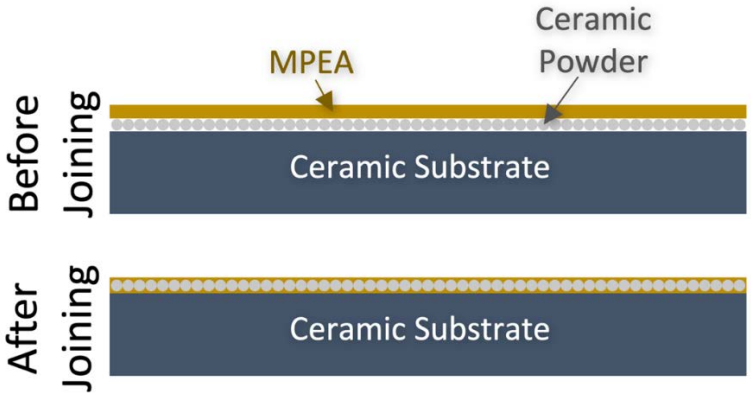

Figure 50. Schematic of the experimental setup for the ceramic powder joint test

After joining, the control specimen and the MMC specimen were removed from the furnace and compared. As seen in Figure 51, The control sample exhibited significant substrate delamination between the carbon fiber layers and had a maximum deflection of 339 μm. In comparison, the MMC sample exhibited no visible delamination, and instead contained only one short crack in the middle of the specimen. The MMC sample had a maximum deflection of 271 μm. These results demonstrated that the addition of TiC particles in this initial trial reduced the overall sample deflection and resulted in fewer defects after joining.

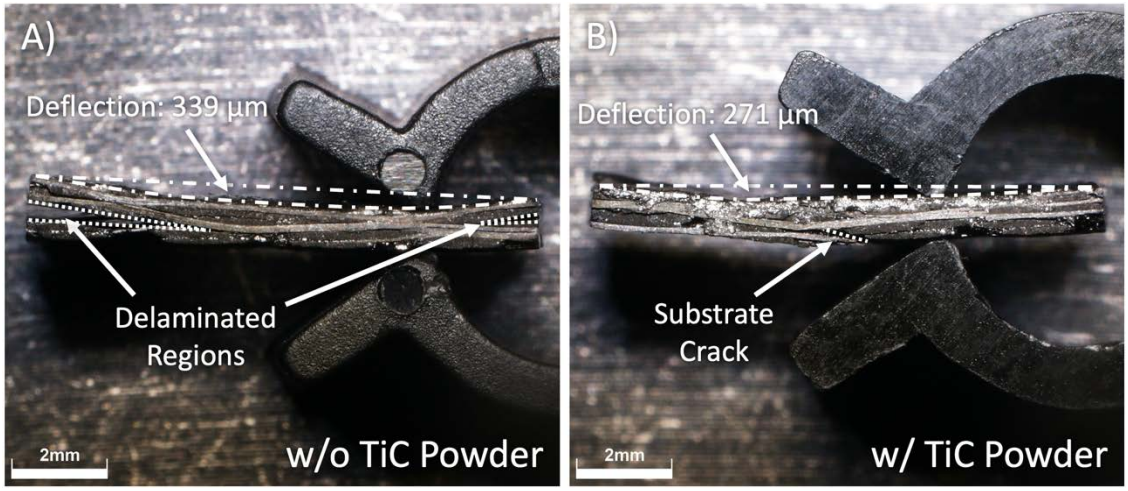

Figure 51. Comparison between (a) the MPEA-filler-only joint sample and (b) the TiC/MPEA MMC joint sample

We performed SEM on the MMC sample to examine the interaction of the TiC particles with the MPEA filler and C-SiC substrate. The SEM image in Figure 52 demonstrates that, unlike all braze and diffusion bonding samples from previous reports, there were no microcracks at the filler/C-SiC interface. In addition to a lack of cracking, the reaction product was not in a continuous layer. Instead, a reaction region of about 150 µm thick formed with dispersed MPEA-SiC reaction product particles throughout the topmost layers of the C-SiC. The original MPEA filler foil thickness was about 200 µm. The MPEA reacted with the SiC matrix, while breaking up the carbon fiber morphology. The reaction region morphology in Figure 52 was a significant improvement over previous microstructures, because the reaction product was dispersed throughout the matrix, not forming a thick layer of brittle silicides.

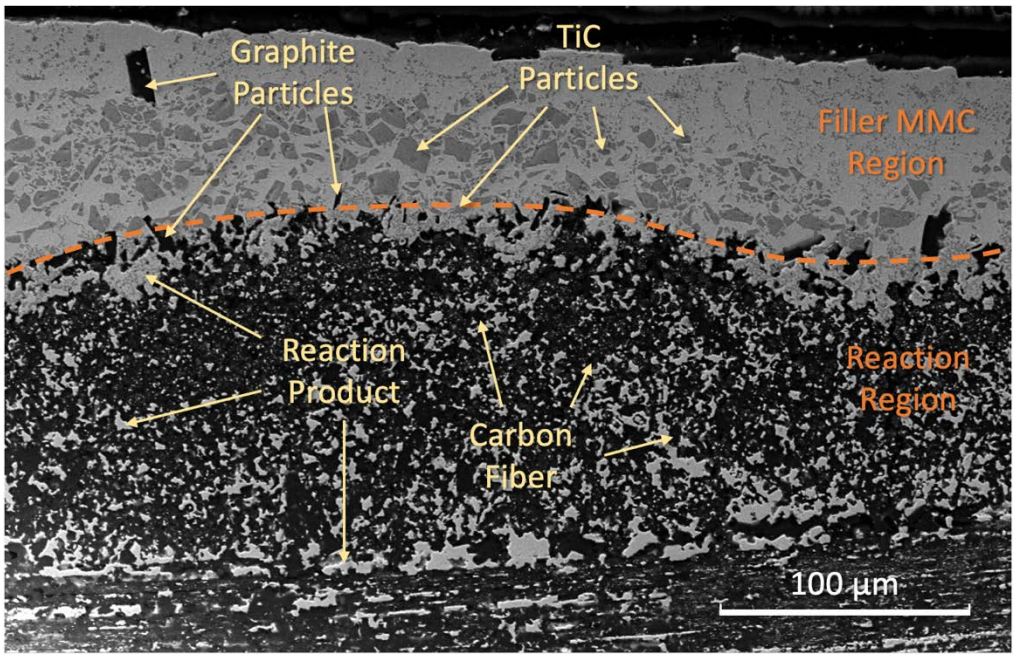

Figure 52. Micrograph filler and reaction regions of the MMC sample, highlighting TiC particles, reaction product morphology, graphite particles, and unreacted carbon fiber

Figure 52 shows that above the reaction region, there was a less significantly affected filler region that was available to bond with a metallic substrate such as Inconel 740H. This region contained the MPEA matrix phase, TiC particles, and some graphite particles that evolved from the dissociation of SiC in the reaction region. Most of the graphite particles were near the edge of the reaction region, but some migrated up to the top of the filler. This migration was likely because graphite is significantly less dense than the MPEA, and the graphite islands floated away from the interface while the MPEA was molten. Finally, although the TiC particles started at less than 4 µm in diameter, TiC particles on the order of 10–20 µm in diameter were observed in the middle of the filler MMC region, which was evidence of significant coarsening. The introduction of carbon to the MMC via the dissociation of SiC and the breakdown of carbon fiber may have been combined with the presence of Ti in the MPEA to contribute to TiC coarsening. However, as shown more clearly in Figure 53, the coarsening was nonuniform.

The fine particles near the interface may be the direct product of the interface reaction, rather than pre-existing TiC introduced in the applied paste. Pre-existing TiC particles could float in the molten MPEA due to density differences, drawing them away from the interface, and this filler was designed to form new TiC through the dissociation of SiC. Therefore, these small particles may be newly precipitated rather than pre-existing, whereas the pre-existing particles were found further from the interface. The fine TiC particles at the top of the MPEA region were likely pre-existing particles that did not coarsen. These may have been the first particles to float in the matrix during melting and thus were transported furthest from the interface, where the availability of introduced carbon from SiC dissociation was lower.

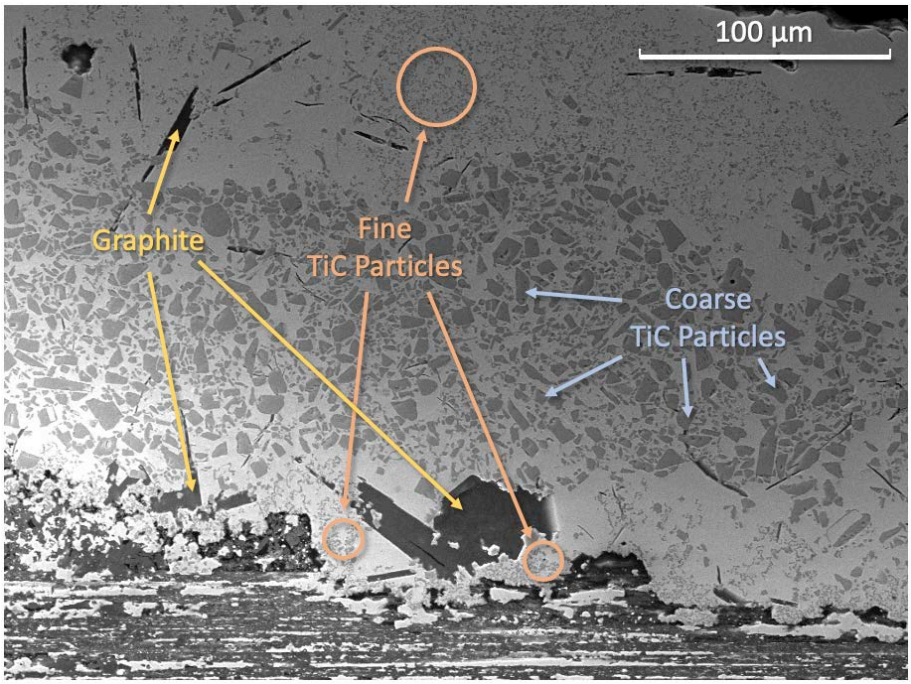

Figure 53. Micrograph of the MMC sample, distinguishing between the locations of fine TiC, coarse TiC, and graphite

Although the initial work with TiC particles was promising, it would be beneficial to use ceramic powders that are less likely to coarsen during brazing and are less reactive with the matrix material, such as WC. WC has been used in tooling in concentrations as high as 97% in cobalt matrices, and it has also been known to be successfully used in nickel and copper matrices, which indicates potential chemical compatibility with the current MPEA filler [79,80]. Additionally, WC is extremely stable below 1,500°C and has a lower CTE than TiC, which could further reduce the effective CTE of the MMC to control deflection and residual stress [81].

2.4.4.2 Simulation of Metal Matrix Composite Joints

Via image thresholding and analysis of the filler MMC region of Figure 52, we determined that the volume fraction of TiC particles in the MPEA matrix was only 26%–30%. This was a relatively low volume fraction that nonetheless demonstrated tangible improvements over the control sample without TiC particles. More carbide particles could be added to the filler, offering further opportunity for improvement. FEA was used to evaluate the effectiveness of stress reduction as a function of the volume fraction of ceramic particles introduced into the MPEA filler matrix. Note that the In740H substrate was not included in this model.

The temperature-dependent properties of SiC and WC were obtained from the literature and input into the FEA. However, due to the novelty of the MPEA filler used, there was no detailed data on its thermophysical properties. Therefore, the material data for the metal was based on an approximation from the individual MPEA components. Additionally, we assumed that the ceramic substrate was monolithic SiC, while the composite filler region was assumed to be a monolithic material with a varying CTE depending on the added volume fraction of WC. The CTE of pure MPEA filler was assumed to be 15.78×10^{-6} K^{-1}. Figure 54 shows the relative reduction in the

predicted maximum thermal-mismatch stress, which occurs in the ceramic substrate, as a function of the volume fraction of WC.

Figure 54 shows that both the von Mises and peak stresses normal to the joint plane could be decreased by as much as 80% by increasing the fraction of WC in the filler to 90 vol.%. Note that the peak stress values were observed within the ceramic substrate immediately adjacent to the dissimilar joint interface. Because all previous experiments used no more than 30 vol.% of ceramic particles, there was significant room for further exploration of this solution. Additionally, because the degree of stress mitigation could be very effective, fiber-reinforced ceramic composites that aim to provide compliance and reduce stresses may no longer be necessary. Although the carbon-fiber reinforcement seemed help mitigate cracking of the SiC substrate, the carbon fiber also allowed easier delamination of the substrate during joining. Both monolithic SiC and fiber-reinforced SiC should be evaluated next for cracking susceptibility in brazing experiments using the MMC filler. Should it prove feasible with the WC-MPEA MMC, reverting to monolithic SiC as the substrate should result in silicide formation in the reaction region without the presence of a significant amount of broken graphite pieces. The joint's sensitivity to silicide formation would be reduced as the residual stress was minimized by the ceramic powder additions to the filler.

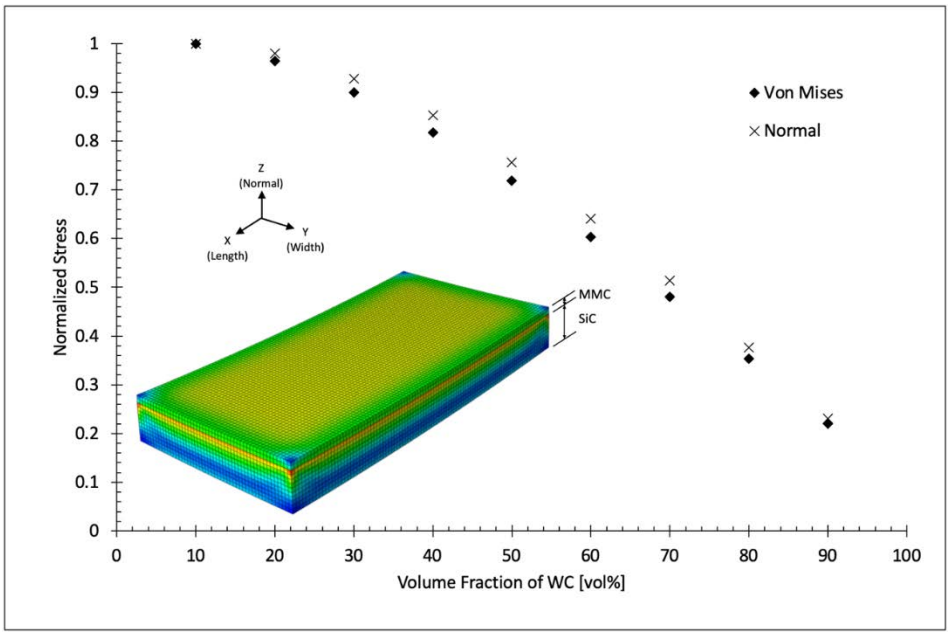

Figure 54. Plot of the normalized von Mises and normal direction (delaminating) stress as a function of WC volume fraction

2.4.4.3 WC and TiC Metal Matrix Composite Filler Trials

Following the initial trial of adding up to 30 vol.% of TiC powders to the MPEA filler to produce an MPEA-carbide MMC, we undertook further investigation to expand the experimental parameter matrix for optimization of braze joint design and fabrication to control stress-induced cracking in the ceramic substrate. As shown in Table 15, trials were performed on both C-SiC and monolithic SiC (M-SiC) ceramic substrates using WC and TiC particles. The as-cast composition of the MPEA foil used was the same as the one detailed in Table 14.

Table 15. MMC Brazing Experimental Matrix

MMC Braze	Ceramic Substrate	Metal Carbide	Designed Carbide Content (Vol.%)
VB20	M-SiC	TiC	28
VB21	C-SiC	TiC	28
VB22	M-SiC	WC	28
VB23	C-SiC	WC	28

Both M-SiC substrate samples from Table 15 (VB20 and VB22) successfully formed the MMC and were metallurgically bonded after the braze cycle. Although a chemical bond was developed in VB20 and VB22, cracks developed in the substrate and filler regions in both samples, possibly due to an insufficient volume fraction of carbide powders in the MMC filler. In the C-SiC substrate samples (VB21 and VB23), the MPEA did not melt, which prevented the formation of the MMC.

Figure 55(a) provides the SEM image of VB20 and indicates that the interactions between the TiC powder and the MPEA filler material were in agreement with what was seen previously. As TiC is a chemical reaction product between the Ti-containing MPEA and SiC, adding 28 vol.% of TiC particles increased the fraction of TiC in the matrix relative to the case where only a metallic MPEA was used as the filler. Furthermore, similar to previous observations, there was significant coarsening of the TiC particles throughout the filler region relative to the initial TiC particle size. This coarsening was hypothesized to result from the reaction byproduct TiC conglomerating with the introduced TiC particles. Other notable microstructural features included a continuous interaction layer that formed at the filler/M-SiC interface and a relatively homogeneous distribution of TiC powder particles, as shown in Figure 55(b). This figure also highlighted the MMC, reaction zone, and M-SiC. The distribution of particles was slightly biased to the middle region of the filler rather than being evenly distributed from the top to the bottom of the filler region. There were areas of lower TiC concentrations, with microcracks localized within these regions, indicating that an increasing volume fraction of MMC powers could effectively control cracking near the joint interface. However, the current mixing method may not be optimal to achieve a uniform mixing ratio across the entire joint interface.

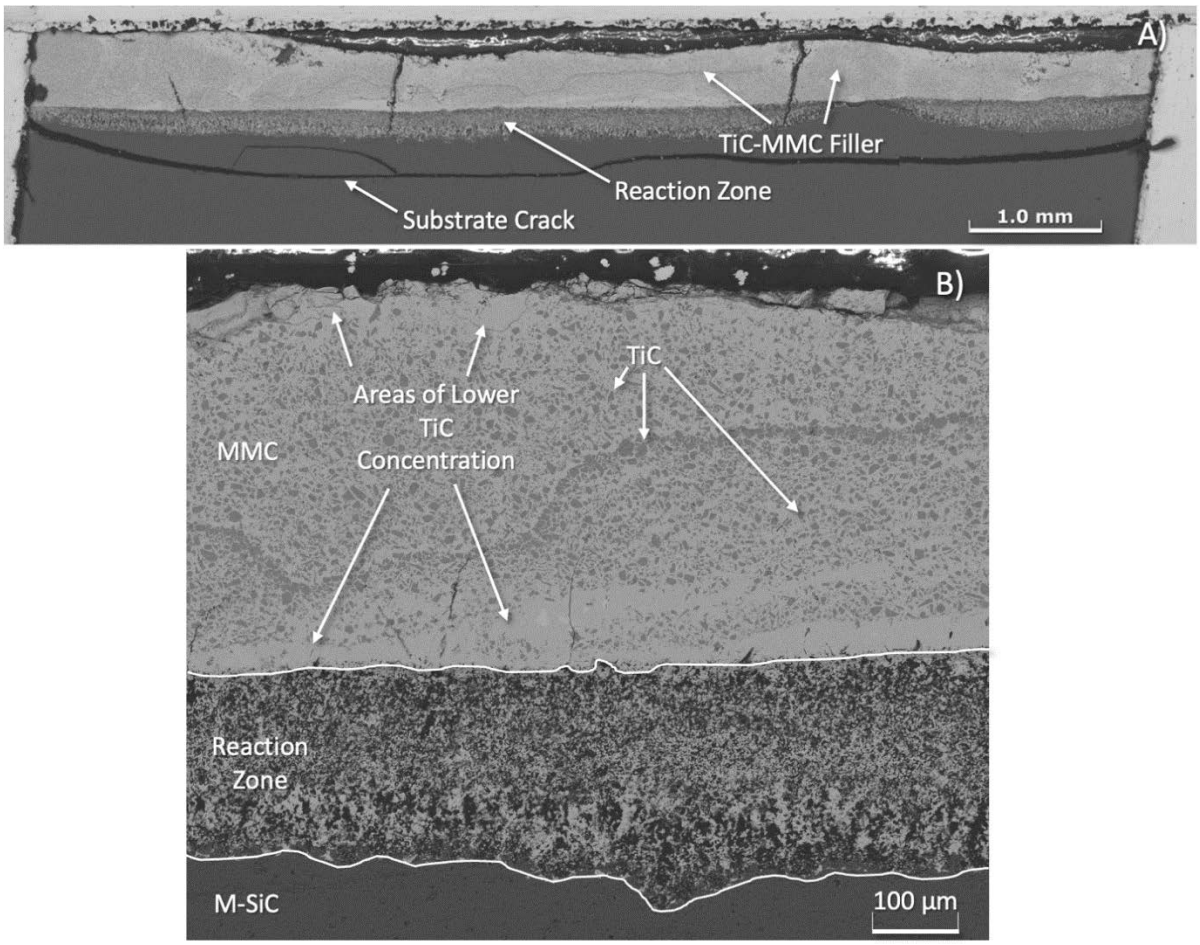

Figure 55. SEM images of (a) the MPEA-TiC MMC braze sample on M-SiC (VB20), and (b) the braze interface at higher magnification

Figure 56(a) shows a macroscopic image of the VB22 sample employing WC particles. By comparing the high-magnification SEM images in Figure 55(b) to Figure 56(b), it was evident that the MPEA and WC reactions were more complex than the those between the MPEA and TiC particles. Most importantly, the WC exhibited better control in terms of the formation of microcracks at the MMC/M-SiC interface due to its lower thermal expansion than TiC. In the MMC filler region of Figure 56(b), there were light particles mixed with darker particles, surrounded by the matrix material. The SEM image in Figure 57(a) highlights the $(W,Ti)_xC_y$ clusters, WC clusters, and MPEA matrix. EDS mapping in Figure 57(b) shows that the lighter, more polygonal particles were unreacted WC, whereas the darker, ring-like structures were likely a mixed Ti-/W-carbide microconstituent. The loop-like 2D morphology of this phase was consistent with the 3D spherical shell structures throughout the MMC, where the composition inside and outside the shell was that of the matrix. It is possible that the $(W,Ti)_xC_y$ microconstituent was a nonequilibrium phase caused by the partial dissolution of WC in the presence of a Ti-rich matrix at high temperatures; this is plausible considering their similar affinity for C under these conditions. However, further study is required to understand the exact stoichiometry and structure of this microconstituent. At the top of the filler region in Figure 56(b), a high concentration of the unreacted WC particles can be seen without the presence of the $(W,Ti)_xC_y$ microconstituent. It is possible that because the WC powder was placed atop the MPEA filler, the MPEA was depleted

of Ti before the particles near the top of the MMC had entered the molten pool. However, this would also require further characterization to verify. Adjacent to the MMC/SiC interface, there was a band of material that did not contain WC or the $(W,Ti)_xC_y$ microconstituent. In this W-free zone, there were TiC particles precipitated from the matrix. These likely precipitated directly from the unbound Ti in the MPEA, combining with the carbon that dissociated from SiC during joining. Finally, graphite islands were previously seen in all examined joining experiments, whereas in both the WC-MMC and TiC-MMC samples, no graphite islands were present in the microstructure. The exact mechanism causing this difference is uncertain, because Ti was present in the same concentrations in previous experiments.

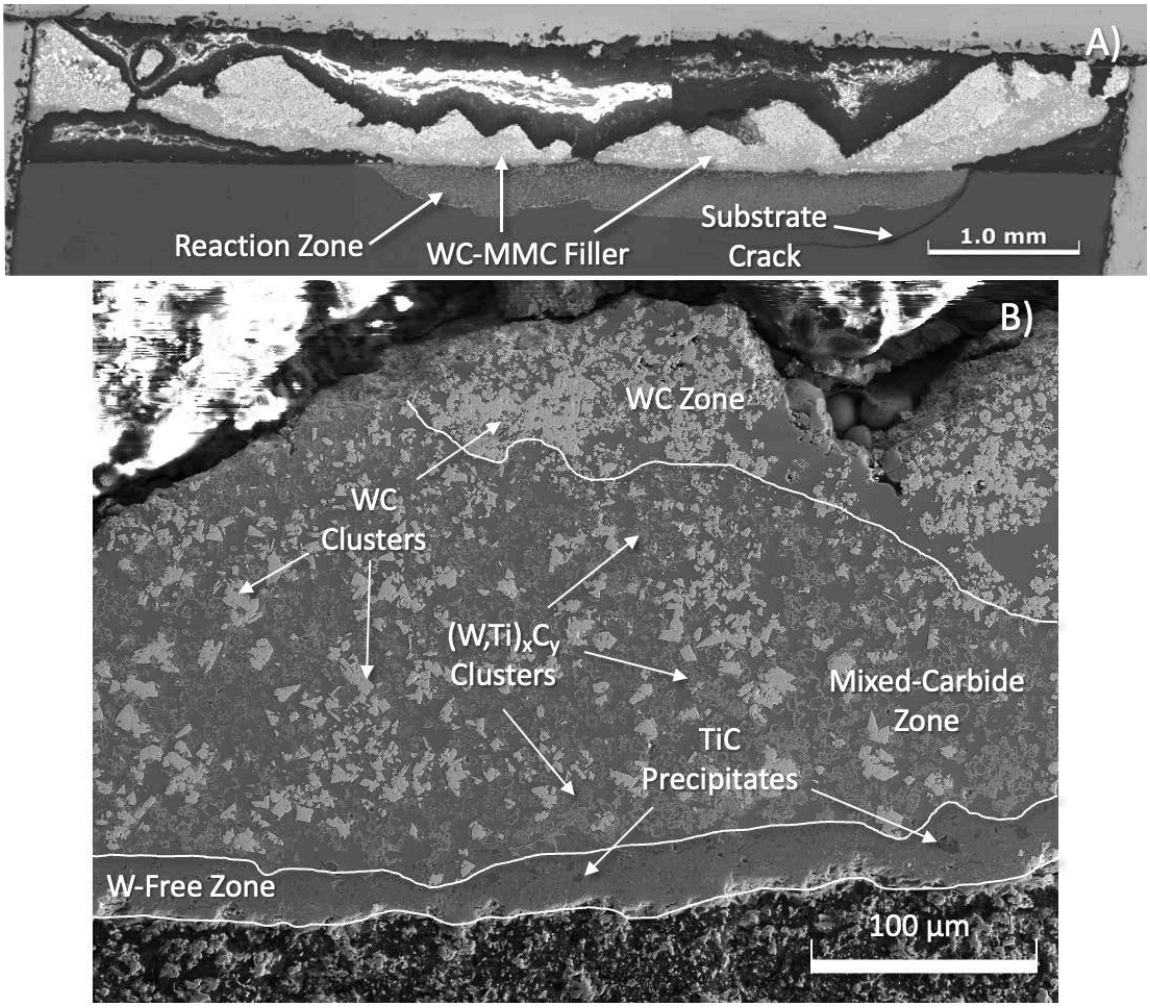

Figure 56. SEM Images of (a) the MPEA-WC MMC braze sample on M-SiC (VB22), and (b) the braze interface at higher magnification

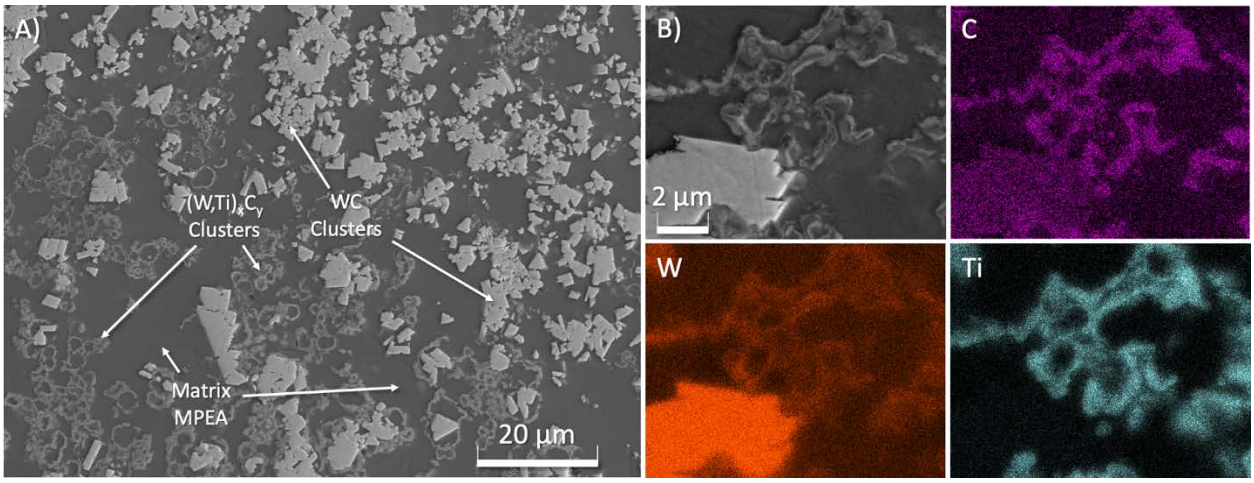

Figure 57. (a) Left panel: SEM image of the mixed-carbide zone within VB22, and (b) Right four panels: high-magnification SEM image and EDS maps for C, W and Ti of a region containing both WC and $(W,Ti)_xC_y$ particles

Using image threshold analysis, we determined that the carbide powders were somewhat nonuniformly dispersed along the length of the M-SiC samples (parallel to the joint interface). The local volume fraction of WC and TiC powders in the M-SiC samples ranged from 19 to 25 vol.%, consistently lower than the designed 28 vol.%. This inconsistency was inevitable due to the method of applying the MPEA/powder paste to the joint surface and the difficulty in containing the powders prior to joining. Strategies for achieving more homogeneity and consistency in the application of filler and carbide particles will be discussed in the next section.

Earlier brazing attempts were made with samples using C-SiC substrates, but these samples did not exhibit any substrate-filler adherence during the experiments, despite a partial earlier success. In the latest MPEA-carbide MMC experiments, the MPEA foil failed to melt adequately to percolate the carbide particles, form the MMC in situ, and bond with the C-SiC substrate. The vacuum capabilities of the furnace were increased recently from 10^{-4}–10^{-5} torr to nearly 10^{-6} torr, which might have caused a greater propensity for off-gassing of the Mn in the MPEA during brazing due to its high vapor pressure at the brazing temperatures. Because Mn served as a melting point depressant in these alloys, this vaporization caused the melting point of the filler to increase. If the higher vacuum levels significantly increased the Mn volatilization rate, the melting point depression by Si and C may not have been able to adequately compensate. At the same time, because the surfaces of the C-SiC samples were not smooth (caused by the fiber texture on the surface), the contact between the solid filler and the substrate was relatively low, limiting diffusion of Si and C into the MPEA. Therefore, it is likely that the compounding effects of increased Mn vaporization and limited surface contact between the C-SiC and the filler foil accounted for the lack of melting in the latest MPEA-carbide MMC experiments with C-SiC.

2.4.4.4 Spark Plasma Sintering for MMC Fabrication

After fabrication of the initial MPEA-carbide MMC test pieces, we determined that, though these samples had provided proof-of-concept scale results, the method used to introduce carbide powder into the joint was not ideal for further testing because of the inconsistency of powder distribution and the difficulty of fabricating repeatable samples. Specifically, applying the carbide particles

manually in paste form, and relying on percolation of the particles by the molten MPEA to form the MMC, was not conducive to repeatability. Additionally, there was a need for a high concentration of carbide particles near the SiC interface, but having a homogeneous mixture with a high volume fraction of carbides would likely induce significantly higher stresses in the joint at the In740H interface. We hypothesize that an MMC material with a graded carbide fraction is necessary to appropriately address the CTE mismatch concerns. Therefore, we conceptualized alternative fabrication methods. First, the entire MMC filler should be in powder form in its as-applied state, which would allow for a more homogeneous mixing prior to joining than a foil format. Second, the joint should be fabricated in some form of die that would prevent the powders from spilling and allow the materials to be green compacted prior to joining. Green compaction ensures good contact between the powders prior to sintering and limits the amount of mixing between layers of differing carbide-to-MPEA powder ratios, preserving the designed concentration gradient. Finally, because the materials being used are effectively hard metals, which are typically produced using solid-state sintering, solid-state sintering techniques should be considered for this process.

There are two processing routes to manufacture metallic MPEA powders. The first consists of casting the MPEA in the vacuum furnace using the previously developed methods, cutting the cast slug into small pieces, and using high-energy ball milling to break the pieces down into a particle size suitable for joining. Although this method guarantees that the alloy is well mixed prior to milling, the large, fabricated pieces are difficult to mill into a powder without using expensive milling containers and media. The second method for manufacturing the MPEA uses mechanical alloying of fine powder feedstock materials to mechanochemically combine the elements in a medium-energy planetary ball mill at temperatures between 25°C and 250°C. This process begins with elemental powder feedstock. The individual powders are combined and subsequently milled for 20–50 hours. This amount of time and methodology is predicted to be sufficient for thorough mixing and mechanochemical alloying. The metallic powders would then be blended with the correct ratios of carbide powders and thoroughly mixed to homogeneity. This method of powder fabrication is common in powder metallurgy applications. Nonetheless, chemical homogeneity will be evaluated before and after any joining trials to verify its effectiveness.

To join and sinter the materials, two sintering techniques were explored. The first was conventional hot pressing under vacuum in a graphite hot press using radiative heating for temperature control and a hydraulic ram for applying pressure. An alternative sintering method often used for powder metallurgy applications—spark plasma sintering (SPS), or field-assisted sintering—was also able to accommodate the desired sample geometry. SPS uses Joule heating and hydraulic pressure to sinter the powders, which allows for high final densities (>98%) with short sintering time (e.g., less than an hour). Because previous diffusion bonding experiments provided successful metallurgical bonds between SiC and this MPEA in the solid state at 30 MPa and 950°C, we expected that the temperatures and pressures suitable for SPS (600°C–850°C and 30–60 MPa) would be sufficient to establish a metallurgical bond between the powders and each ceramic substrate. The SPS process was therefore conceptualized to both form the MPEA-carbide MMC with the desired composition gradient and effectuate joining of the multi-material structure.

Finally, we determined that a tight-fitting graphite die is likely to be most effective for joining these samples. Although graphite may cause some carburization of the outermost edges of the joint when in full contact, it is a common material for SPS and conventional sintering dies because of

its impressive high-temperature mechanical properties, electrical and thermal conductivity, and machinability. Additionally, graphene foil is readily available and can be wrapped around the circumference of the joint to prevent the MPEA from bonding to the die. A schematic of this proposed setup can be seen in Figure 58, which shows the die and exemplary sample layers with MPEA-xMC designating an MMC layer fabricated with x vol.% of metal carbides and the MPEA being the balance.

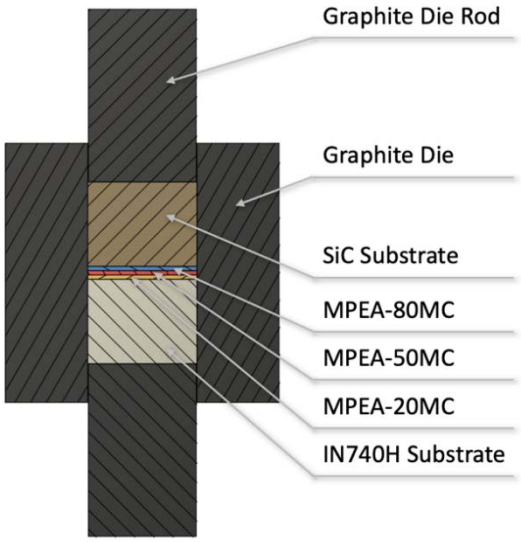

Figure 58. Schematic of the cylindrical SPS die setup for MPEA-carbide MMC joining between In740H and SiC

We determined that TiC may be more stable than WC at the MMC brazing temperatures. This was evidenced by the evolution of a $(W,Ti)_xC_y$ microconstituent in the sample containing WC, while no additional phases were developed with the addition of TiC particles to MPEA samples. For the solid-state sintering experiments, WC continued to be evaluated, as unreacted WC was expected to provide greater CTE control than TiC and may be nonreactive at the lower joining temperatures. The experimental campaign proceeded to investigate the feasibility of using the ball milling method to manufacture the powder MMC feedstock material and evaluating SPS as a feasible joining technique with powder MMC feedstock.

2.5 Development of Glass Ceramics for Ceramic-End Joining

The project team pursued low-temperature joining materials/techniques (mostly below the annealing temperature of In740H, about 1,200°C) for preliminary SiC-to-SiC joining. The purpose was to protect the In740H alloy from exposure to too-high temperatures in a single-step joining process. However, the efforts were not successful, which raised the question of whether higher-temperature processing was needed. Therefore, the project team started pursuing higher-temperature joining materials/techniques for SiC.

Glass ceramics, as a group of high-temperature joining materials for SiC applications, were investigated extensively. Based on a recent review by Liu et al. [55], an oxide system made of rare-earth oxide (e.g., Y_2O_3), Al_2O_3, and SiO_2 at various compositions could be promising. Depending on the processing temperature, joining has been reported using a binary Y_2O_3 and

Al_2O_3 at relatively high temperatures of 1,600°C–1,900°C with minor additions of other additives, such as SiO_2 and C [56–61]. When SiO_2 is added as a major constituent, the processing temperature can be significantly lower, about 1,400°C [62–66]. Because the overall constituents were similar in both approaches, we investigated both experimentally.

2.5.1 High-Temperature Al-Y-O Glass Ceramics for SiC Joining

2.5.1.1 Synthesis and SEM-EDS Characterization

NREL first synthesized the Al-Y-O glass ceramics. Reagent-grade chemicals were used. The raw chemical powders were mixed by ultrasonication in isopropyl alcohol (IPA) for 15–30 minutes before drying off the IPA at 90°C–100°C in a drying oven. The dried powders were uniaxially pressed in a steel die at about 200 MPa for 2 minutes before high-temperature treatment at up to 1,650°C (the highest temperature NREL's furnace can achieve). After 1,650°C for 1–2 hours, the samples generally had a weight loss of <0.5 wt.%. The lower-temperature end of the Y_2O_3-Al_2O_3 phase diagram (see Reference [82]) was targeted, i.e., above 62.5 mol.% Al_2O_3, to have a lower processing temperature. The goal was to synthesize a composition with a lower liquid formation temperature to aid the liquid phase sintering of SiC. There are three distinct Al-Y-O compounds relevant to the application: (1) $3Y_2O_3{\cdot}5Al_2O_3$, or YAG, with an overall Al-to-Y atomic ratio of 5:3, (2) $3Y_2O_3{\cdot}5Al_2O_3$, or YAP, with an overall Al-to-Y atomic ratio of 1:1, and (3) $2Y_2O_3{\cdot}Al_2O_3$, or YAM, with an overall Al-to-Y atomic ratio of 1:2. The compositions investigated were all around YAG or above the Al_2O_3 content of YAG to take advantage of the lower liquid formation temperature. Because NREL's furnace was limited to about 1,650°C, complete liquid formation was not anticipated, and some deviations in behavior may be expected.

Figure 59 is the back-scattered SEM image of the synthesized YAG glass (at 1,650°C), showing three different phases based on their relative brightness. The majority was the darkest phase, such as Scan 2 and Scan 5. Scans 1, 3, and 6 indicated the mid-brightness regions. Scan 4 was the brightest region with the lowest concentration (only a few spots could be found throughout the scans). EDS was performed to measure the Al-to-Y atomic ratios at these scan locations.

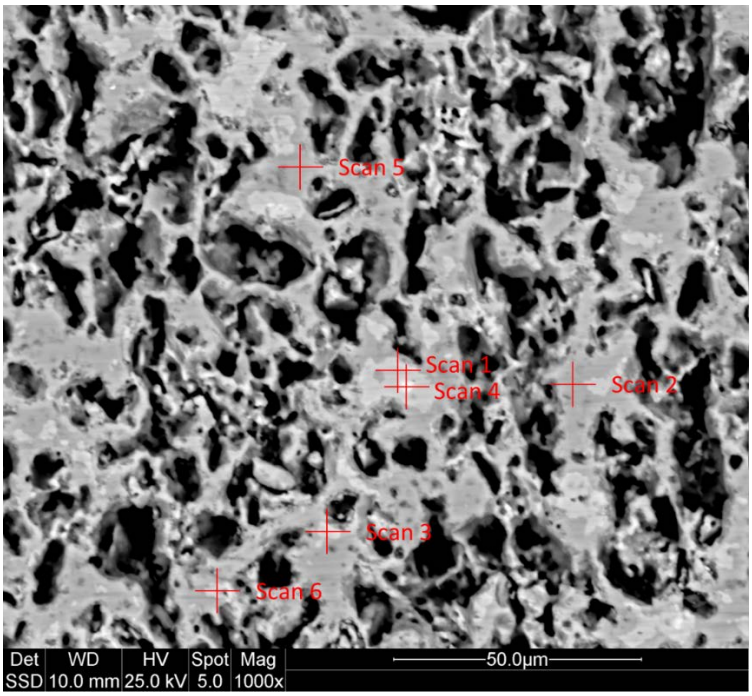

Figure 59. Back-scattered SEM image of the synthesized YAG glass (at 1,650°C)

Table 16 shows the EDS scans with the measured Al-to-Y atomic ratios of the phases in the synthesized Al-Y-O glass ceramic. The scans confirmed that the majority of the phases in the synthesized glass ceramic were the YAG phase, with occasional inclusion of the YAP phase at a higher Y content and rarely any YAM phase. The EDS analysis was supported by a powder XRD measurement, which exhibited major peaks from YAG, YAP, Al_2O_3, and Y_2O_3.The findings corroborated the initial added amounts of Al_2O_3 and Y_2O_3 and the <0.5 wt.% total weight loss during synthesis. However, the findings also confirmed that the 1,650°C heat treatment temperature was not able to fully melt the glass, based on the porous structure of the synthesized glass. If the glass ceramic were to be used for joining, a higher processing temperature would certainly be needed, which may damage the SiC-fiber-reinforced SiC CMC transition tube (see Figure ES1), as the CMCs were known to start gradually losing their stability above the 1,400°C–1500°C range. This was a major reason we did not pursue the high-temperature Al-Y-O glass ceramic as the joining material for the ceramic end.

Table 16. EDS Scans Showing the Al-to-Y Atomic Ratios of the Phases in the Al-Y-O Glass Ceramic

Scan	Al-to-Y Atomic Ratio
1	1.04
2	1.65
3	1.03
4	0.41
5	1.64
6	1.04
Reference Compositions	
YAG ($Y_3Al_5O_{12}$)	1.67
YAP ($YAlO_3$)	1
YAM ($Y_4Al_2O_9$)	0.5

2.5.2 Low-Temperature Si-Al-Y-O Glass Ceramics for SiC Joining

2.5.2.1 Synthesis and SEM-EDS Characterization

A lower-temperature Si-Al-Y-O glass ceramic was synthesized at 1,500°C with an overall composition of 25.1 wt.% Al_2O_3, 30.7 wt.% Y_2O_3, and 44.2 wt.% SiO_2 near the eutectic composition. The powder preparation method was similar to that used before for the Al-Y-O glass ceramics. The powders or pressed pellets were put into an alumina crucible for heat treatment at 1,500°C with furnace cooling or air quench. This near-eutectic composition has a melting point of around 1,375°C [83], as shown by the ternary phase diagram [65]. For simplicity, this composition is referred to as SAY. It was of interest for a few reasons:

- The reported average CTE of the SAY glass up to 700°C (i.e., near the expected operating temperature) is about 4.36×10^{-6} [83], which matches closely to that of SiC (about 4.45×10^{-6}) [84] in the same temperature range.
- The wetting angle of a few ternary Al_2O_3-Y_2O_3-SiO_2 compositions has been reported [62]. The composition closest to the SAY glass has a wetting angle of around 10° on SiC, which suggests promising adhesion properties.
- The SAY glass, along with other Re_2O_3-Al_2O_3-SiO_2 systems (Re indicating a rare earth element), has been reported to successfully form an interlayer between SiC plates for joining applications at processing temperatures of about 1,400°C [66].
- The reported glass transition temperature T_g and recrystallization temperature T_c of glass ceramics similar to the SAY glass are 916°C and 1,224°C [66], respectively, indicating a low chance of mechanical degradation at the desired operating temperature of the joint at up to 800°C.
- The helium leak rate of the glass-ceramic-joined SiC-to-SiC has been reported by [66] to be on the order of 1×10^{-10} mbar·L/s at 900°C for up to 300 hours. This leak rate indicates good hermiticity.
- A few similar ternary Al_2O_3-Y_2O_3-SiO_2 compositions have been tested for thermal shock resistance by air quenching the joint from 1,200°C to room temperature [62]. The results suggest promising resistance to thermal shock that may be experienced by the joint in concentrating solar applications.

Figure 60 is the back-scattered SEM image of the SAY glass synthesized at 1,500°C, showing two different phases. The EDS measurements summarized in Table 17 revealed that the compositions at Scans 1–4 were almost the same as the starting composition of the powder mixture (excluding the contribution from oxygen). Scans 5–9 had a distinct composition of about 72.3 wt.% Al_2O_3 and 27.7 wt.% SiO_2, which was very close to the mullite composition ($3Al_2O_3 \cdot 2SiO_2$). Mullite formation was possible based on the phase diagram [65], which shows the proximity of the eutectic composition to the phase field labeled "MUL." Given the fact that this specific sample for EDS analysis was slowly cooled after heat treatment at 1,500°C (1°C/min above 1,400°C and 2°C/min between 1,200°C and 1,400°C), it could have experienced recrystallization above its recrystallization temperature of 1,224°C and/or phase separation during the slow cooling. In addition, Figure 60 proved that 1,500°C heat treatment was able to completely melt the SAY glass, and the actual joining temperature could be lower than 1,500°C, as reported by [66].

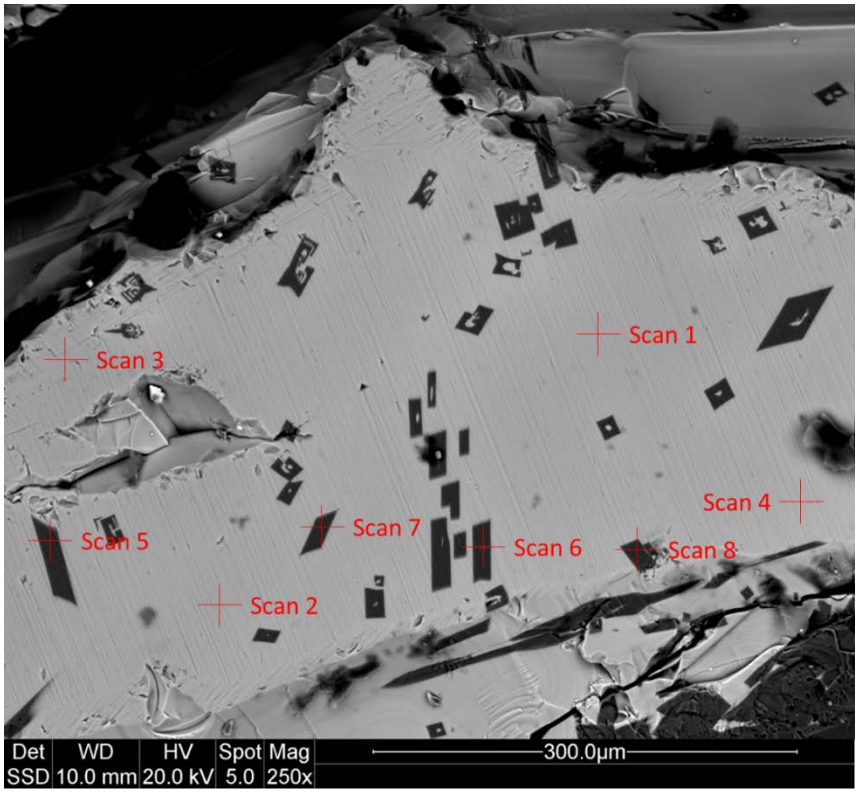

Figure 60. Back-scattered scanning electron microscope image of the synthesized SAY glass

Table 17. EDS Scans Showing the Compositions of the Phases in the SAY Glass Ceramic

Point Scan #	Wt.%		
	Al	Si	Y
1–4	22.3 ± 0.5%	35.0 ± 0.7%	42.7 ± 1.1%
5–9	72.3 ± 0.7%	27.7 ± 0.7%	0.0%
Reference Compositions			
Starting Composition	22.8%	35.5%	41.6%
Mullite ($3Al_2O_3 \cdot 2SiO_2$)	74.2%	25.8%	0.0%

A few preliminary joining experiments were performed with the synthesized SAY glass at 1,300°C and 1,400°C in both air and Ar atmosphere. The SAY glass powder was dispersed in an IPA/water mixture and ultrasonicated for 2 minutes before applying the mixture to the joint area. The SAY glass/liquid suspension was applied to two pieces of SiC plates to form a joint sample for heat treatment. No significant pressure was applied to the joint during heat treatment; a large alumina plate was placed on top of the joint to ensure no relative movement of the SiC plates during heating and cooling. The heating program was set at 10°C/min to 1,000°C, 5°C/min to 1,200°C, and 2°C/min to the final heat treatment temperature. The dwell time at the final heat treatment temperature was 1 hour. A controlled cooling of 5°C/min was used.

Figure 61 shows the optical microscope images of the SAY joint samples (heat treated at 1,400°C in air and Ar). The thickness of the SAY interlayer was about 50–100 μm.[11]

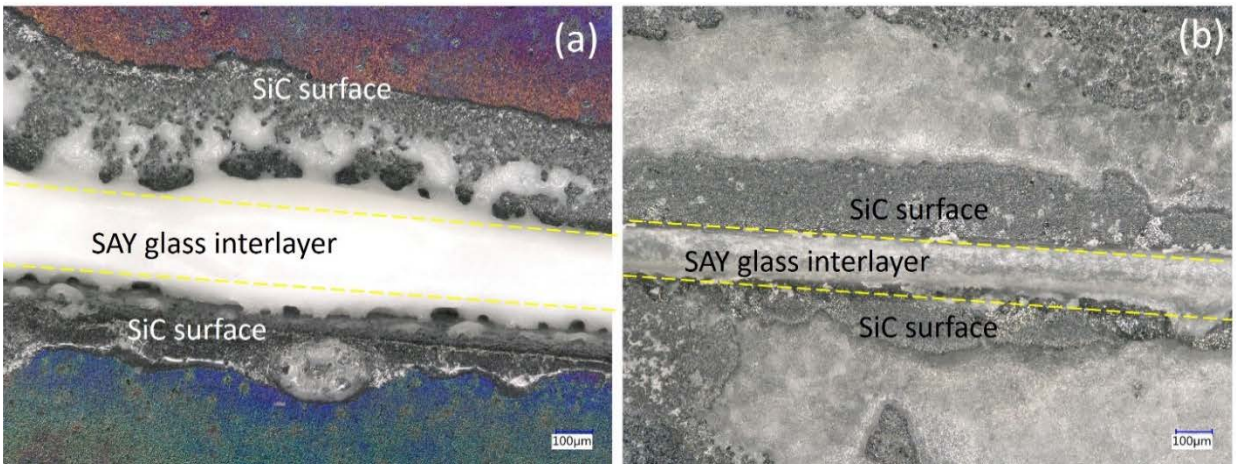

Figure 61. Optical microscope images of SAY joints heat treated at 1,400°C in (a) air and (b) Ar

We made additional samples with heat treatment at 1,400°C in Ar atmosphere where the SiC-SAY interface was polished and better characterized, as shown by Figure 62. The smooth interface, despite some bubble formations, indicated good overall wetting of the SAY glass ceramic interlayer on the SiC plates. No observation of cracking at the interface suggested a good CTE match between the SAY glass ceramic interlayer and the SiC plates.

[11] The microscope images may suggest an interlayer thickness of over 100 μm, but the actual interlayer thickness was lower because some SAY glass was squeezed out of the interlayer slightly, leading to a seemingly thicker interlayer.

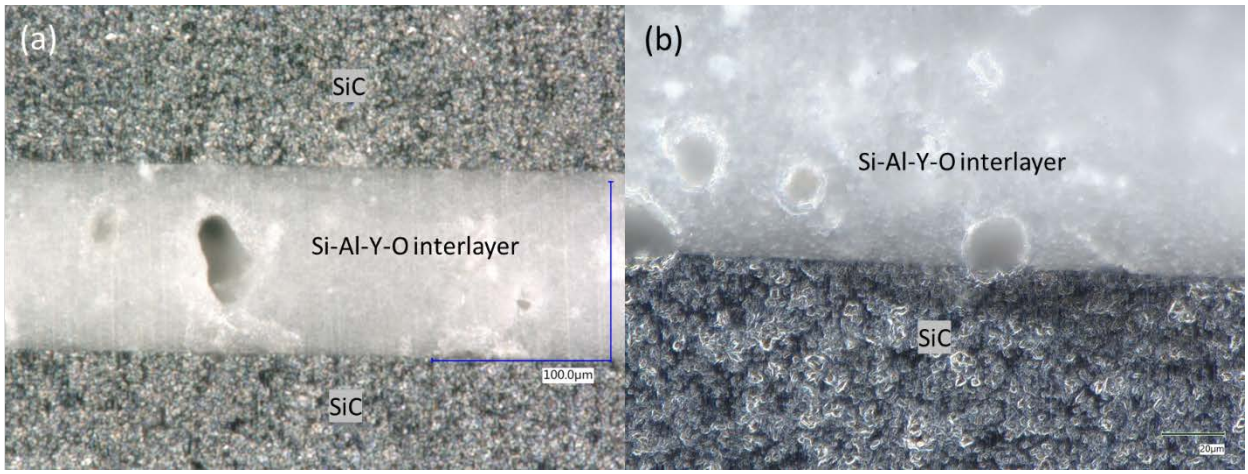

Figure 62. Optical microscope images of a polished SAY joint heat treated at 1,400°C in Ar at (a) 1,000x and (b) 1,500x magnifications

Figure 63 shows the back-scattered SEM images of the joint interface between SiC plates and the SAY glass ceramic at (a) 500x and (b) 1,000x magnifications, with EDS point scan locations. The joint sample was heat treated at 1,400°C in Ar atmosphere. The microstructure was similar to the reported structure of Si-Al-Y-O glass ceramics used for SiC joining [62–64,66,83], where crystalline yttrium disilicate and mullite and an amorphous glass phase were identified [66,83]. Table 18 summarizes the EDS scans, showing the compositions of the phases in the SAY glass ceramic interlayer. The scan numbers correspond to the scan locations in Figure 63. Although the measured compositions were, to some extent, different from the reference yttrium disilicate ($Y_2Si_2O_7$) and mullite ($3Al_2O_3 \cdot 2SiO_2$), we believed that the bright phase at Scans 2–4 was very close to yttrium disilicate (with some additional aluminum) and the dark phase at Scans 8–10 was very close to mullite. The medium bright phase (Scans 5–7) was not easily identified based on the overall measured compositions. The literature suggested a glassy phase from which the yttrium disilicate and mullite precipitated out.

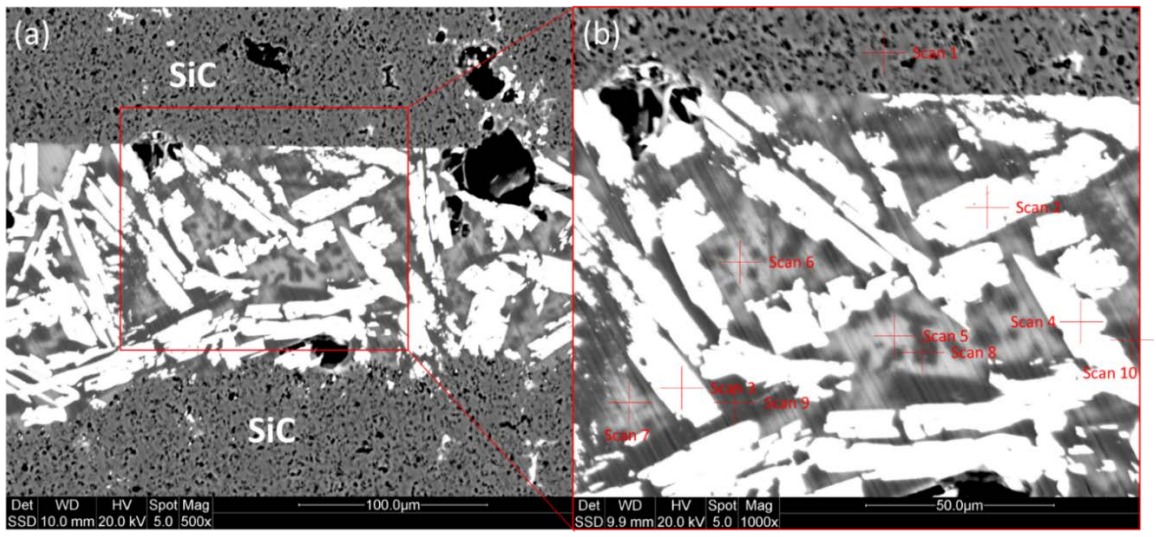

Figure 63. Back-scattered SEM images of the joint interface between SiC plates and the SAY glass ceramic at (a) 500x and (b) 1,000x magnifications, with EDS point scan locations

Table 18. EDS Scans Showing the Compositions of the Phases in the SAY Glass Ceramic Interface for a Joint Sample Heat Treated at 1,400°C in Ar Atmosphere

Point Scan #	Wt.%		
	Al	Si	Y
2–4	3.88 ± 1.68%	26.74 ± 0.49%	69.39 ± 2.16%
5–7	27.55 ± 5.28%	55.61 ± 3.23%	16.85 ± 2.05%
8–10	70.04 ± 0.39%	29.96 ± 0.39%	0.00%
Reference Compositions			
SAY Starting Comp.	22.83%	35.53%	41.64%
Mullite ($3Al_2O_3 \cdot 2SiO_2$)	74.24%	25.76%	0.00%
Yttrium disilicate ($Y_2Si_2O_7$)	N/A	21.02%	78.98%

2.5.2.2 Preliminary Mechanical Strength Measurement at Room Temperature

Preliminary shear tests were performed on the first few SAY glass ceramic joint samples. Table 19 summarizes the mechanical testing results for the preliminary shear testing samples using the SAY glass ceramic interlayer. The samples heat treated in Ar were significantly better than those treated in air. The improvement was not only reflected by the shear strength, but also by the failure mode. For Samples 1 and 2, the failure was clearly due to the detachment of the SAY interlayer from the SiC plates. For Sample 3, pre-mature SiC cracking occurred at about 10 MPa stress due to misalignment of the SiC plates when making the shear sample. Samples 4 and 5 had a very different failure mode, where failure within the SiC plates, rather than a detachment of the interlayer from the SiC plates, was observed. This suggested that the adhesion between the SAY glass ceramic and the SiC plates may have exceeded the stress experienced by the SiC plates themselves.

Table 19. Summary of the Preliminary Mechanical Testing Results for the SAY Glass Ceramic Joint Samples

Name	Sample 1	Sample 2	Sample 3	Sample 4	Sample 5
Heat Treatment	1,400°C for 1 hour in Air		1,400°C for 1 hour in Ar		
Joint Dimension (mm^2)	160.3	150.1	144.4	131.0	75.3
Failure Force (N)	1590	1255	2445	4500	3410
Failure Stress (MPa)	9.92	8.36	16.93	34.35	45.29
Failure Mode	Detachment of the interlayer from the SiC plates			Delamination-like behaviors within the SiC plates	

Figure 64 shows the optical microscope images of the failure interface for Sample 4.[12] It is clear that at some locations of the SAY glass/SiC interface, large areas of SiC were pulled apart from its original SiC plate. The rest of the surface was covered by a thin layer of SAY glass, with

[12] Optical microscopy analysis of Sample 5 showed very similar failure interface to that of Sample 4.

composition confirmed by EDS measurements. These behaviors suggested the possibility that the adhesion was stronger than the SiC itself at certain locations.

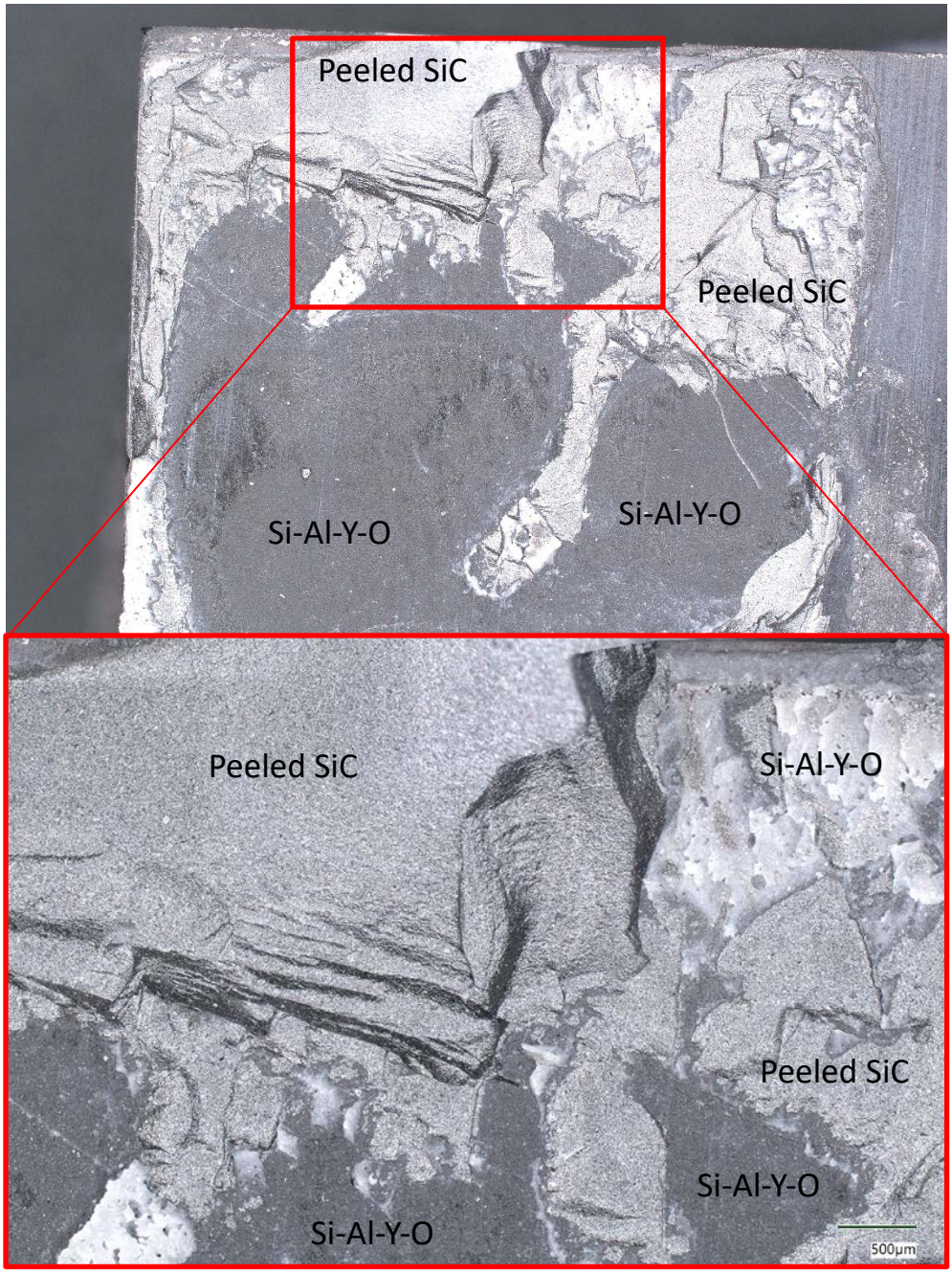

Figure 64. Optical microscope images of the post-shearing interface showing sections of peeled SiC and Si-Al-Y-O glass ceramics covering the original SiC joining surface

Figure 65 shows the back-scattered electron SEM image and secondary electron SEM image of the post-shearing surface of the SAY glass ceramic joint. Combined with EDS measurements, it was easy to identify the bright regions as areas covered by an Si-Al-Y-O composition and the darker regions as areas with some peeled-off SiC. There were significant variations in the

measured compositions for the Si-Al-Y-O regions (i.e., 44.8 ± 8.2 wt.% Al, 31.4 ± 5.7 wt.% Si, and 23.9 ± 7.8 wt.% Y) based on three point scans and three area scans. This measured composition was significantly different from the starting composition of the SAY glass ceramic (as shown in Table 17). It was also different from any of the compositions measured in Table 18, which represented the phases in the bulk of the interlayer (rather than locations near the SiC/interlayer interface), so certain chemical reactions might have happened.

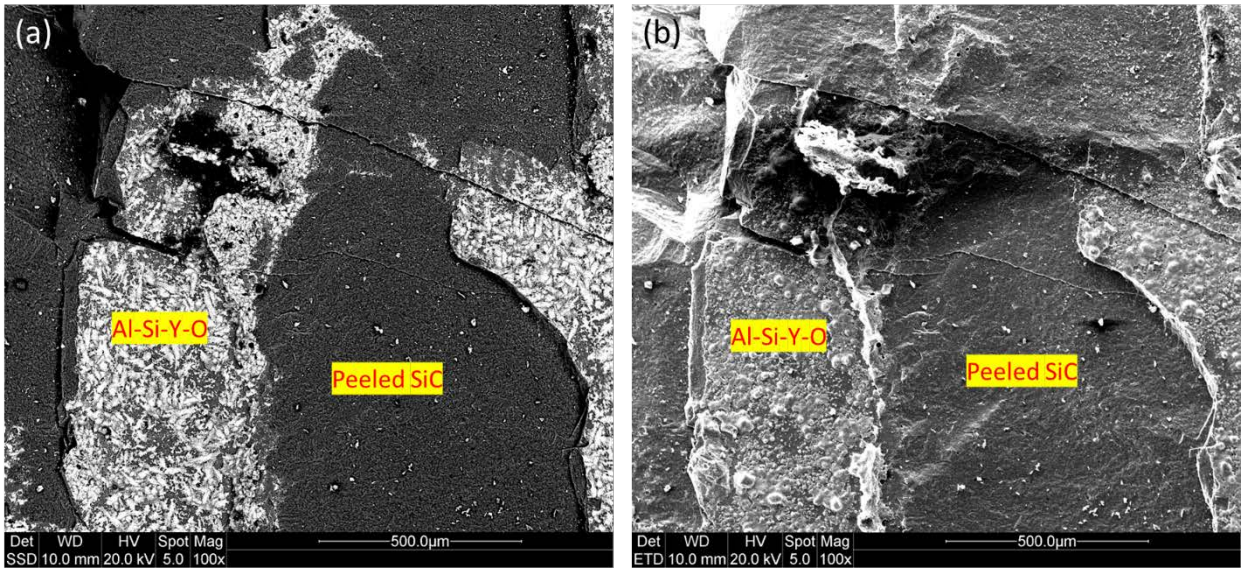

Figure 65. (a) Back-scattered electron SEM image and (b) secondary electron SEM image of the post-shearing surface of the SAY glass ceramic joint

Figure 66 is the back-scattered SEM image at a lower magnification, showing the relatively uniform coverage of the Si-Al-Y-O glass ceramic.

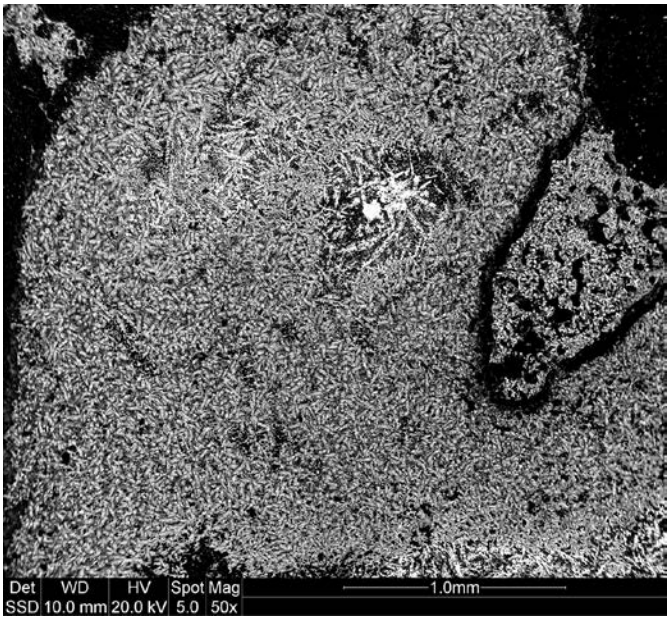

Figure 66. Back-scattered electron SEM image at a lower magnification, showing the relatively uniform coverage of the Si-Al-Y-O glass ceramic on the post-shearing surface

The preliminary room-temperature mechanical testing results were encouraging. A few parameters were of interest for the next step:

- No quantitative optimization was performed for the preliminary joint samples. Hence, the solid-to-liquid ratio of the SAY glass powder and IPA/water mixture could be optimized to enhance the SAY coverage.
- Pre-oxidation of the SiC plates to form the SiO_2 scale may have an effect on the joining to the SAY glass ceramic.
- Due to the lower processing temperature at ~1,400°C, other joining techniques may be considered. For example, hot pressing in this temperature range may provide additional benefits when a thinner interlayer than 50 µm is preferred.
- A better mechanical testing setup should be considered. The testing setup used may introduce bending and/or buckling of the SiC plates, especially when the loading reaches >3,000 N.

2.5.2.3 Process Optimization of Joining Conditions

2.5.2.3.1 Effect of Processing Time

The preliminary mechanical testing results encouraged a longer processing time of 5 hours at 1,400°C. Figure 67 shows the optical microscopy image of one SAY joint sample's joining interface with 5 hours of processing at 1,400°C. Note that the image was taken without any polishing to avoid damage to the joint interface for subsequent mechanical testing.

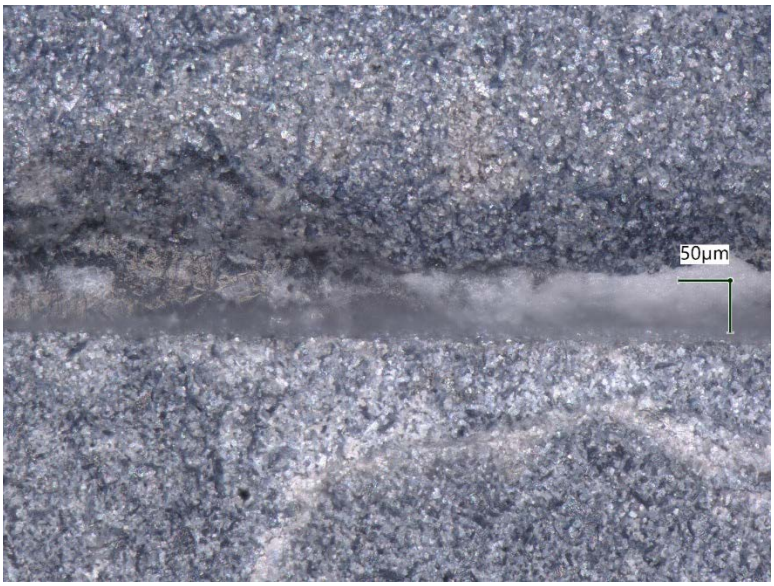

Figure 67. Optical microscopy image of a SAY glass ceramic joint interface with 5 hours of processing at 1,400°C

With a longer processing time of 5 hours at 1,400°C, the shear strength of the joint was improved to 48.9 MPa and 62.2 MPa for two samples. We hypothesized that the longer processing time allowed more time for the molten SAY glass to wet and interact with the SiC plates, which led to higher shear strength.

Figure 68 shows the image of a post-fracture shear sample with 5 hours of processing at 1,400°C (62.2 MPa of measured shear strength). The yellow lines indicate the fracture patterns. The symmetry of the fracture patterns suggests that some bending of the SiC plates might have caused the overall failure due to slight misalignment or plate buckling. The overall load was 4,705 N at failure, and the total displacement of the platens was about 1 mm, which roughly translates to ~2.5% strain for the entire joint sample. Reference [85] reported about 0.8% failure strain for SiC (grade N produced by Cercom) under a uniaxial compression test. Although the direct comparison with reference [85] (which tested a SiC sample under uniaxial compression) might not be appropriate, it at least suggested that ~2.5% strain in the test configuration is significant and may lead to buckling or bending failure of the SiC plates. Because of the high strain, we expected that a sudden, catastrophic failure of the brittle SiC plates could happen, leading to a violent release of energy that could subsequently fracture the nearby joint interface.

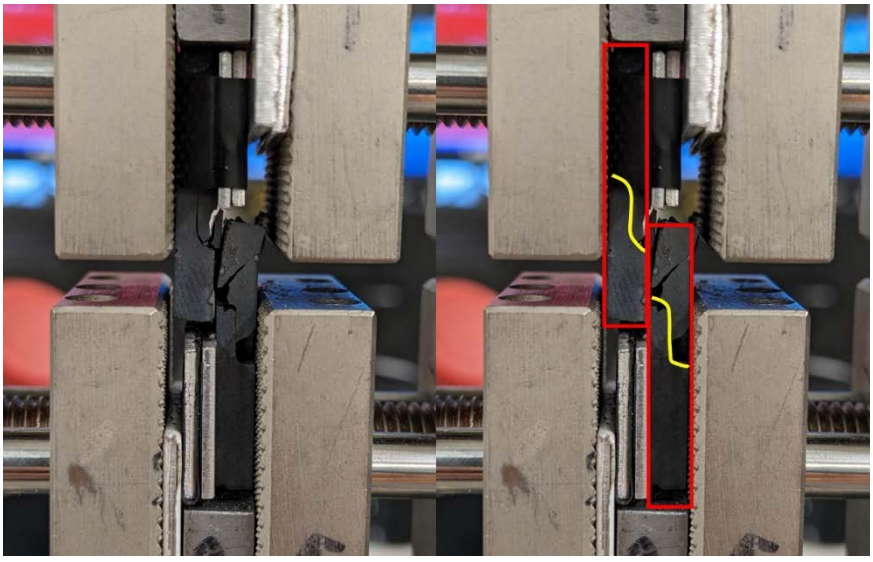

Figure 68. Image of a post-fracture shear sample with 5 hours of processing at 1,400°C

Therefore, we performed a simple mechanical simulation to estimate the stress level and stress distribution within the SiC due to the deformation caused by 0.5 mm and 1 mm of total displacement (Figure 69). The goal was to analyze the stress distribution, which helped explain the fracture patterns shown in Figure 68 and understand whether the observed loading and displacement could lead to buckling or bending failure of the SiC plates. As shown in Figure 69, there was a clear stress concentration near the locations indicated by the yellow circles in both cases, which corresponded to the observed fracture patterns in Figure 68, assuming that the symmetric cracks initiated from the stress concentration locations. In addition, the simulation assumed a perfect bond between the two SiC plates, which, to some extent, could roughly approximate the shear sample if the SAY joint interface were stronger than the SiC. The stress level predicted by the simulation showed that cracking at the circled locations was possible because the maximum stress (14 GPa and 28 GPa) was on a similar order of magnitude as the yield strength of SiC (21 GPa). Therefore, the simulation suggested that the cracking of the SiC plates could be triggered by sharp stress concentration, and the SAY joint interface indeed had a decent strength, which allowed the joint interface to survive the shear load until the SiC plates failed.

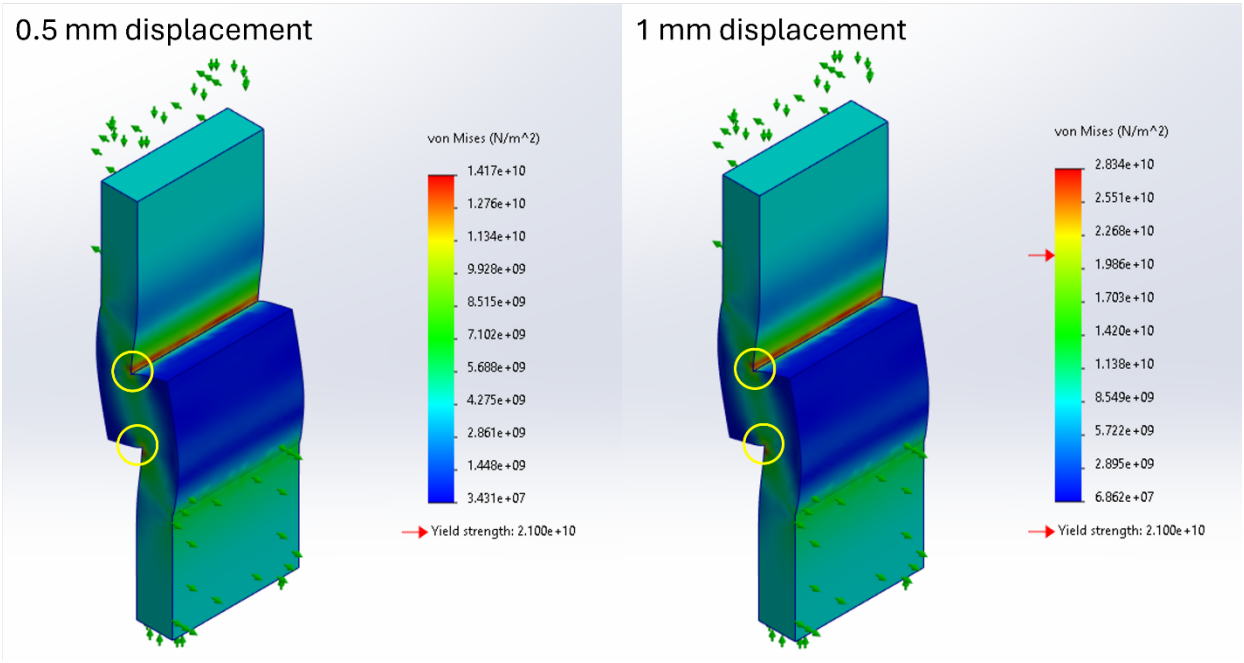

Figure 69. Mechanical simulation of the shear test sample assuming 0.5 mm and 1 mm of total displacement

Figure 70 shows the optical microscope images of the post-shear sample of the fracture surface and the cross section view of the fracture surface (after embedded in epoxy resin for polishing). The polished cross section shows a dense SAY interlayer with good wetting to the SiC plate, which may explain why this batch of shear test samples had improved shear strength, possibly due to longer processing time at 1,400°C.

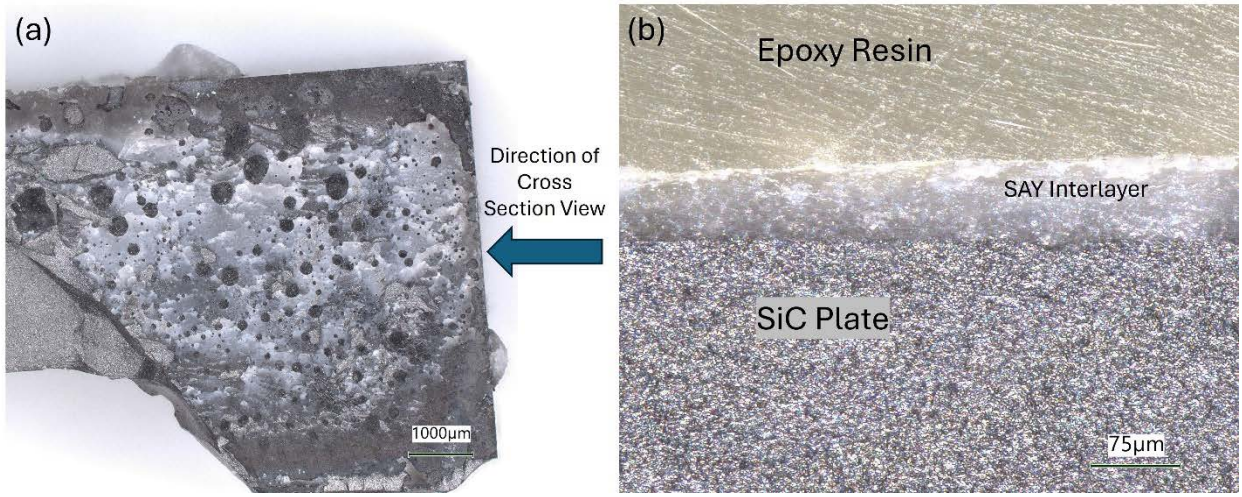

Figure 70. Optical microscope images of the post-shear sample showing (a) the surface view and (b) the cross section view of the fracture surface

Figure 71 shows the optical microscope images of the post-shear joint surface with extensive regions of peeled-off SiC (indicated by the red enclosed areas). This behavior was similar to the

previously reported samples with 1 hour of heat treatment at 1,400°C, which again suggested that the bonding interface was strong such that some SiC was peeled off during shear testing.

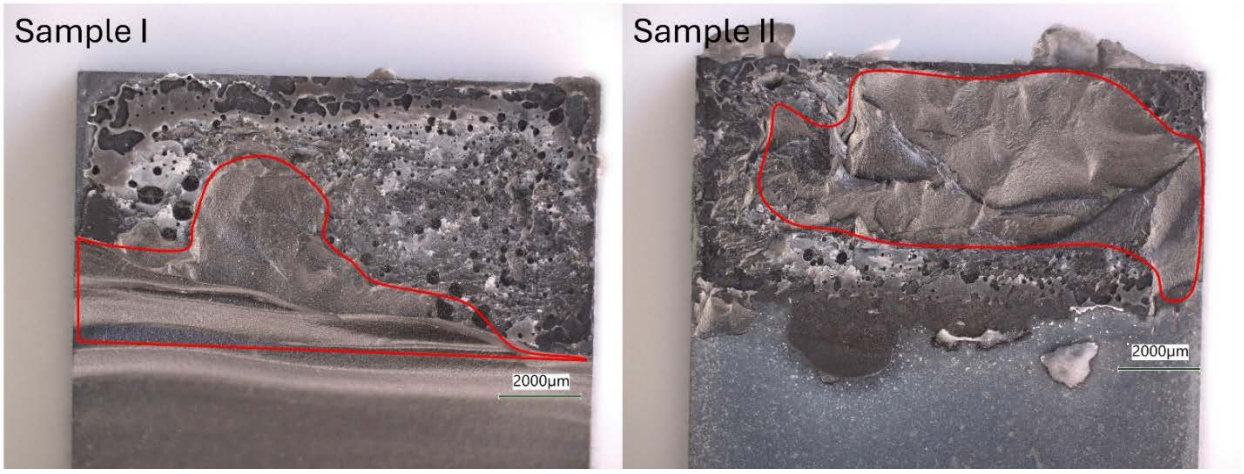

Figure 71. Optical microscope images of the post-shear joint surface with 5 hours of processing at 1,400°C

Although the shear strength was over 60 MPa, additional improvement routes were identified. Figure 70(a) showed that bubble or cavity formations were present within the SAY glass ceramic interlayer, which may serve as stress concentrators by reducing the effective bonding area. Figure 71(a) is a better representation of the typical coverage of the joint area by the glass ceramic. We estimated that the total coverage was about 80%, roughly in line with the coverage estimation based on SAY glass mass loading into the joint before heat treatment.

Figure 72 shows the SEM images of the same cross section interface as in Figure 70(b). This interface survived the shear test after the SiC plates suddenly fractured. Therefore, we believed that it represented one of the better bonded fractions of the entire interlayer. At up to 1,500x magnification, the image confirmed good wetting and bonding characteristics between the SAY glass ceramic interlayer and the SiC plate. The relatively smooth bonding interface without major gaps was observed along the entire length of the cross section (over 1 mm in length). Higher-magnification transmission electron microscopy analysis was also performed to further zoom into the bonding interface to understand the bonding behaviors at a smaller scale (discussed later).

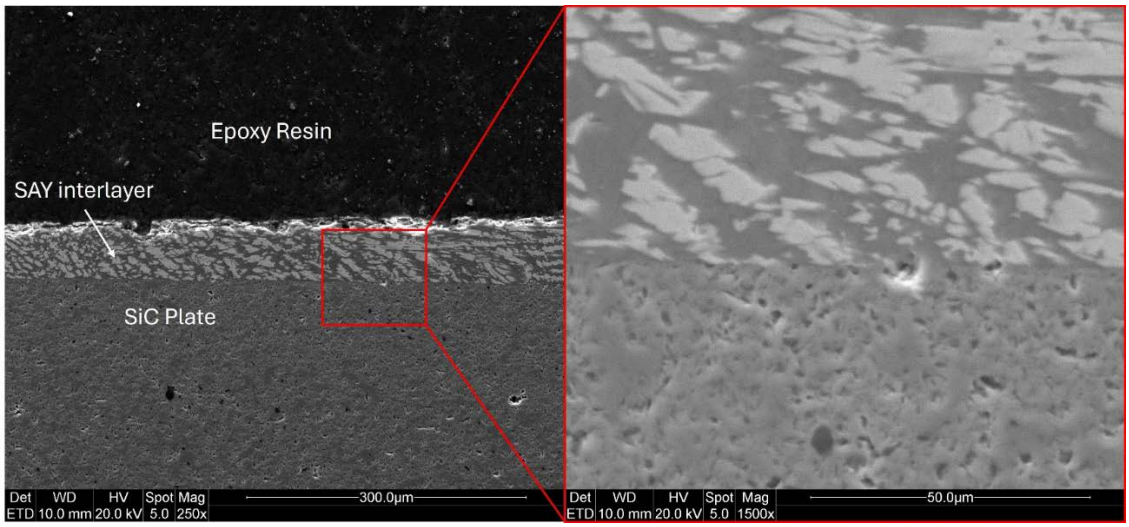

Figure 72. SEM images of the cross section of the post-shear SAY joint sample heat treated at 1,400°C for 5 hours

Table 20 summarizes the EDS spot scans for different phases and area scans in Figure 72. The composition of the bright phase was closest to the yttrium disilicate ($Y_2Si_2O_7$), which has been reported as a major precipitate phase for SAY glass ceramics [62–64,66,83]. The bright phase composition was also close (within one measured standard deviation) to that observed in previous SAY joint samples that were heat treated at 1,400°C for 1 hour within one measured standard deviation (see Table 18). Although the SEM images exhibited one dark phase, there were likely two distinct dark phases, based on random spot scans (dark phase I and dark phase II). One was similar to the mullite composition, and the other was believed to be a glassy phase. The area scans of the entire interlayer showed very close composition to the overall starting composition of the synthesized SAY glass. Such behavior is highly consistent with previous SAY glass ceramics heat treated at 1,400°C for 1 hour and cooled with the same method. Therefore, the consistent composition measurements indicated that the synthesis and processing were highly repeatable.

Table 20. Summary of EDS Spot Scans for Different Phases and Area Scans in the SAY Glass Ceramic Interlayer for a Joint Between Monolithic SiC Plates

Scan Locations	Wt.%		
	Al	Si	Y
Bright phase	2.98 ± 2.03%	28.04 ± 1.29%	68.99 ± 3.11%
Possible dark phase I	70.29 ± 3.63%	29.49 ± 3.94%	0.22 ± 0.30%
Possible dark phase II	21.67 ± 2.79%	60.60 ± 6.78%	17.74 ± 9.57%
Entire glass ceramic interface	22.78 ± 0.16%	37.22 ± 0.64%	39.99 ± 0.80%
Reference Compositions			
Starting Composition	22.83%	35.53%	41.64%
Mullite ($3Al_2O_3{\cdot}2SiO_2$)	74.24%	25.76%	N/A
Yttrium disilicate ($Y_2Si_2O_7$)	N/A	21.02%	78.98%

2.5.2.3.2 Effect of Processing Temperature

The results of higher shear strength due to longer processing time at 1,400°C also prompted investigation into higher processing temperatures. The hypothesis was based on the wetting behavior of molten SAY glass on SiC as well as the potential chemical reactions, both of which were believed to be a function of temperature. However, as reported by [66], a too-high processing temperature may have the negative effect of introducing bubbles on the SiC surface due to SiC reaction with the constituents in the glass ceramic. In fact, most literature studies were performed at ≤1,500°C [55,86]. Hence, we selected 1,500°C as the test limit. Two joint samples were made.

Figure 73 shows the SEM image of the joint interface of one SAY sample processed at 1,500°C for 1 hour in Ar atmosphere. Weak bonding characteristics were observed at the SiC-SAY interface. Unsurprisingly, the shear strength was measured to be only about 9.7 MPa with a joint area of about 90 mm^2.

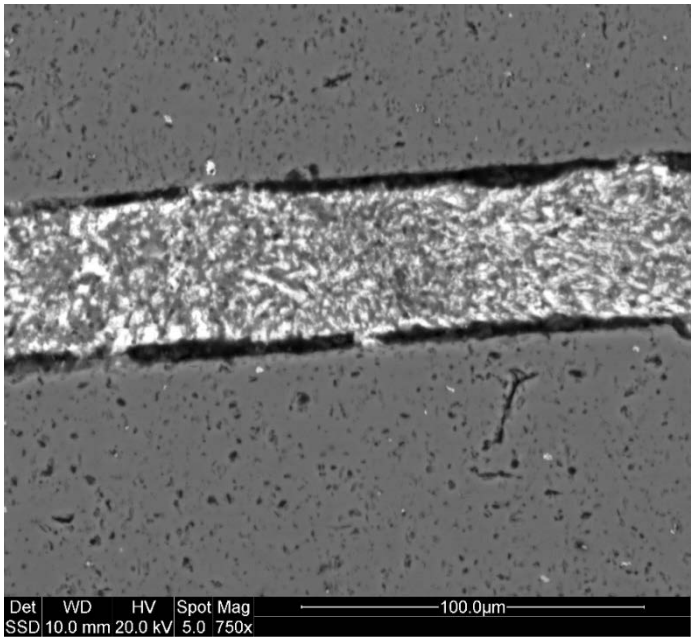

Figure 73. SEM image of a SAY joint interface processed at 1,500°C for 1 hour in Ar atmosphere

There were several possible reasons for the weak bonding behavior at the interface:

1. The wetting behavior of the SAY glass on SiC-SiC fiber composite was experimentally measured by Fan et al. [62]. However, due to the thermal instability of the SiC fibers, no temperature dependence of the wetting angle was measured. Hence, the wetting behavior at 1,500°C remained unknown. It may be negatively affected by several factors, such as increased evaporation of volatile constituents in the glass ceramic, increased oxidation of the SiC, or even changes in the surface properties of the SiC.
2. The higher processing temperature could lead to gas/bubble formation, preventing joining. The gas/bubble formation was hinted at by a reaction between SiC and the Al_2O_3 and SiO_2 constituents in the SAY glass by Baud et al., who suggested that the main possible gaseous species were $Al_2O(g)$, SiO(g), and CO(g) at these temperatures [57,87–89].

Experimental wetting angle measurements between the monolithic SiC plate and the SAY glass were later performed at various temperatures.

2.5.2.3.3 Effect of Hot Pressing

The bubble/cavity formation within the glass ceramic interlayer prompted the use of a hot press as the joining technique with the hope of reducing the bubble/cavity formation and facilitating better bonding. The hot-pressed samples were first formed at 1,400°C for 1 hour using the normal joining process in a conventional tube furnace. The reason was that the alignment of the two SiC plates needed to be almost perfect to avoid misalignment issues during the shear tests. Then the hot-pressing process reheated the joint sample to the final hot-press temperature at about 10°C/min, held the sample for 1 hour, and cooled the sample to room temperature at about 5°C/min. A pressure of 1–3 MPa was applied to the sample during the entire heating and cooling process. The varying pressure of 1–3 MPa was due to some technical issues with the hot press's control system that were not fully resolved at the time of the hot-pressing experiments. Table 21 summarizes the hot-pressing parameters and shear testing results of the two hot-pressed joint samples. Neither sample showed any strength improvement compared to the conventional joint samples, which suggested that the hot pressing was not beneficial.

Table 21. Summary of Hot-Pressed SAY Joint Samples

	HP Sample #1	HP Sample #2
First heat treatment before hot press	1,400°C for 1 hour in Ar	
Hot press temp. (°C)	1,400	1,200
Hot press time (hour)	1	
Hot press atmosphere	Ar	
Joint area (mm^2)	91.8	103.8
Shear strength (MPa)	23.2	5.2

The comparison between the hot-pressed samples at 1,400°C and 1,200°C provided more insights into the hot-pressing effect on the SAY interlayer. It was reported that the SAY glass composition has a glass transition temperature of 916°C, a recrystallization temperature of 1,224°C, and a melting point of 1,375°C [83]. The low strength of the 1,200°C sample was likely a result of mechanical damage from pressing on the interface at a temperature not high enough to allow molecular rearrangement.

Other reasons might be responsible for the lower strength of the 1,400°C hot-pressed sample. Because 1,400°C is higher than the melting point, hot pressing at this temperature should not introduce mechanical damage. The observation of squeezed-out SAY glass from the joint interface and a reduction of the joint thickness proved that the glass was fully melted during the 1,400°C hot-pressing process. It should be noted that the hot pressing was carried out in a graphite furnace, with graphite platens and graphite sheets as the pressing hardware. Baud et al. have reported that graphite can complicate the SiC-Al_2O_3-SiO_2-Y_2O_3 system [57]. In addition, the reducing environment of the graphite furnace may also reduce SiO_2 and form additional SiO(g) and CO(g) [90]. Therefore, carbon contamination from graphite may have prompted more formation of gaseous species, according to Baud et al., leading to weaker joining strength. Second, although the 1,400°C hot-pressed sample had a fully molten SAY glass interlayer at temperature, it still needed to cool down and form the solid SAY glass interlayer. Because the load was on for the entire hot-

pressing process, some mechanical damage may have happened during the cooling process (similar to what happened to the hot press sample at 1,200°C).

Before ruling out hot pressing as a processing technique, a few changes could be investigated:

1. Alumina hardware could be used to avoid potential complications from carbon.
2. The loading/unloading schedule could be redesigned to avoid potential mechanical damage during the cooling process (i.e., reduce the load during cooldown).

2.5.2.4 Pre-Oxidation of SiC plates

2.5.2.4.1 Wetting Angle Measurements

The literature of using glass ceramic to join SiC materials indicates that the formation of a strong native SiO_2 scale on the SiC is beneficial for the joining [91–95]. The leading explanation is that the native SiO_2 scale dissolves in the glass ceramic during the joining process and forms a strong bond to the underlying SiC upon cooling. It should be noted that although the idea of having a native SiO_2 surface to aid bonding with a chemically similar glass may sound attractive, the presence of SiC and its potential reaction with SiO_2 may generate gaseous species of SiO(g) and CO(g) at the interface with the SiC plate [57,87–89]. In addition, for the joining of ceramics using an interlayer material, substrate wetting is critically important. Good wetting behavior is expected to lead to higher strength of the joint [94]. Therefore, the wetting behaviors of the SAY glass ceramic ($12Y_2O_3$-$22Al_2O_3$-$66SiO_2$, mol%) on SiC surfaces with different surface treatments were studied experimentally.

For the wetting experiments, sintered SiC substrates were polished to 30 μm and subsequently placed on an alumina support located within the uniform hot zone of an alumina tube furnace. The SiC specimens were pre-oxidized by heating to a maximum temperature of 1,300°C and held for 3 hours, in accordance with the results from reference [94], which demonstrated that pre-oxidization of the SiC surface at 1,300°C for 3 hours in air decreased the wetting angle of calcium lithium aluminosilicate from 62° to 33°. This enhanced wetting due to pre-oxidation of the SiC surface and resulted in a 119% increase in the shear strength of resulting joints. For subsequent wetting experiments, non-oxidized and pre-oxidized SiC specimens were heated at 10°C/min to a maximum temperature between 1200°C–1450°C in flowing Ar or air. Imaging of the SAY glass ceramic droplet was done by a Sony Cyber-shot DSC-HX400V camera with Carl Zeiss lens (Vario-Sonnar T* F-number (Maximum Aperture): F2.8 (W)–6.3 (T); Focal length: f = 4.3–215 mm). Pictures were processed in ImageJ and analyzed with the DropSnake plugin[13] to calculate the left and right wetting angles, as shown in the schematic in Figure 74. The average of the right and left wetting angles was calculated along with standard deviation (95% confidence interval) to represent error bars.

[13] Rasband, W.S., ImageJ, U. S. National Institutes of Health, Bethesda, Maryland, USA, https://imagej.net/ij/, 1997-2018.

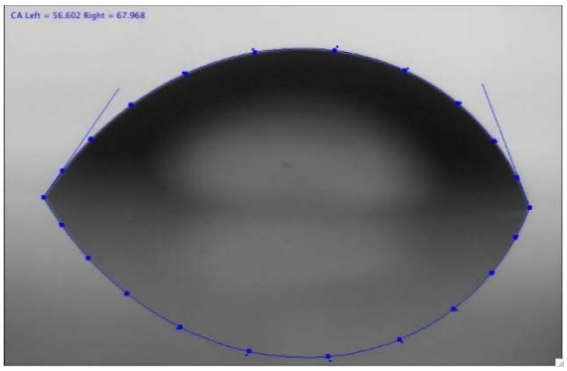

Figure 74. Schematic representing the output of the DropSnake plugin in ImageJ, showing the left and right contact angle (CA) of a droplet on a substrate

Figure 75 shows the actual images captured during the series of wetting experiments to confirm the effect of SiC surface pre-oxidation as well as the processing atmosphere. It is clear that a >90° wetting angle persisted throughout the wetting experiment for a polished (non-oxidized) SiC in Ar atmosphere. The high wetting angle was correlated to the formation of a large air bubble trapped inside the droplet. Thus, the apparent wetting angle from the images in Figure 75 might not be sufficient to describe the actual wetting behavior of the SAY glass ceramic on non-oxidized SiC in Ar. On the contrary, the same polished (non-oxidized) SiC in air atmosphere exhibited completely different behavior. The wetting angle decreased consistently with increasing temperature to a final value of about 20°–40° with large variances (the exact angle was difficult to measure due to the image quality). The pre-oxidized SiC in air atmosphere showed a decreasing wetting angle as a function of temperature, with a final wetting angle of about 20°–30° (average of left and right angles). Note that a wetting angle of about 10° was observed on the right side of the SAY molten droplet. The left side of the molten droplet was constrained by the small size of the SiC substrate, which rendered the measurement much less useful. The range of wetting angles for the latter two cases roughly agreed with the literature [62]. Note that the non-oxidized SiC was likely oxidized by the air environment prior to the full melting of the SAY glass ceramic. Thus, the latter two cases likely converged to a similar category of oxidized SiC substrate in contact with molten SAY glass ceramic. Additional wetting experiments with pre-oxidized SiC in Ar atmosphere should provide more insight into the source of good wetting behavior, i.e., due to SiO_2 scale formed during pre-oxidation or during heat treatment inside an air atmosphere. Figure 76 summarizes the average wetting angles as a function of temperature in air atmosphere. The wetting angle apparently decreased from just above 60° at 1,175°C to 30° at 1,400°C for pre-oxidized SiC substrate. For non-oxidized SiC, no trend of wetting angle with temperature was observed. The final wetting angles at 1,450°C were 29° ± 9° and 41° ± 2° for pre-oxidized and unoxidized SiC surfaces, respectively. The dwelling at 1,450°C for 1 hour resulted in the lowest wetting angle of 6° for pre-oxidized SiC surface. This result may indicate a time-dependent wetting phenomenon (e.g., transport-limited reactive wetting). This sample also displayed the highest shear strength among tested specimens, in agreement with expectation that low wetting angles result in stronger bonds.

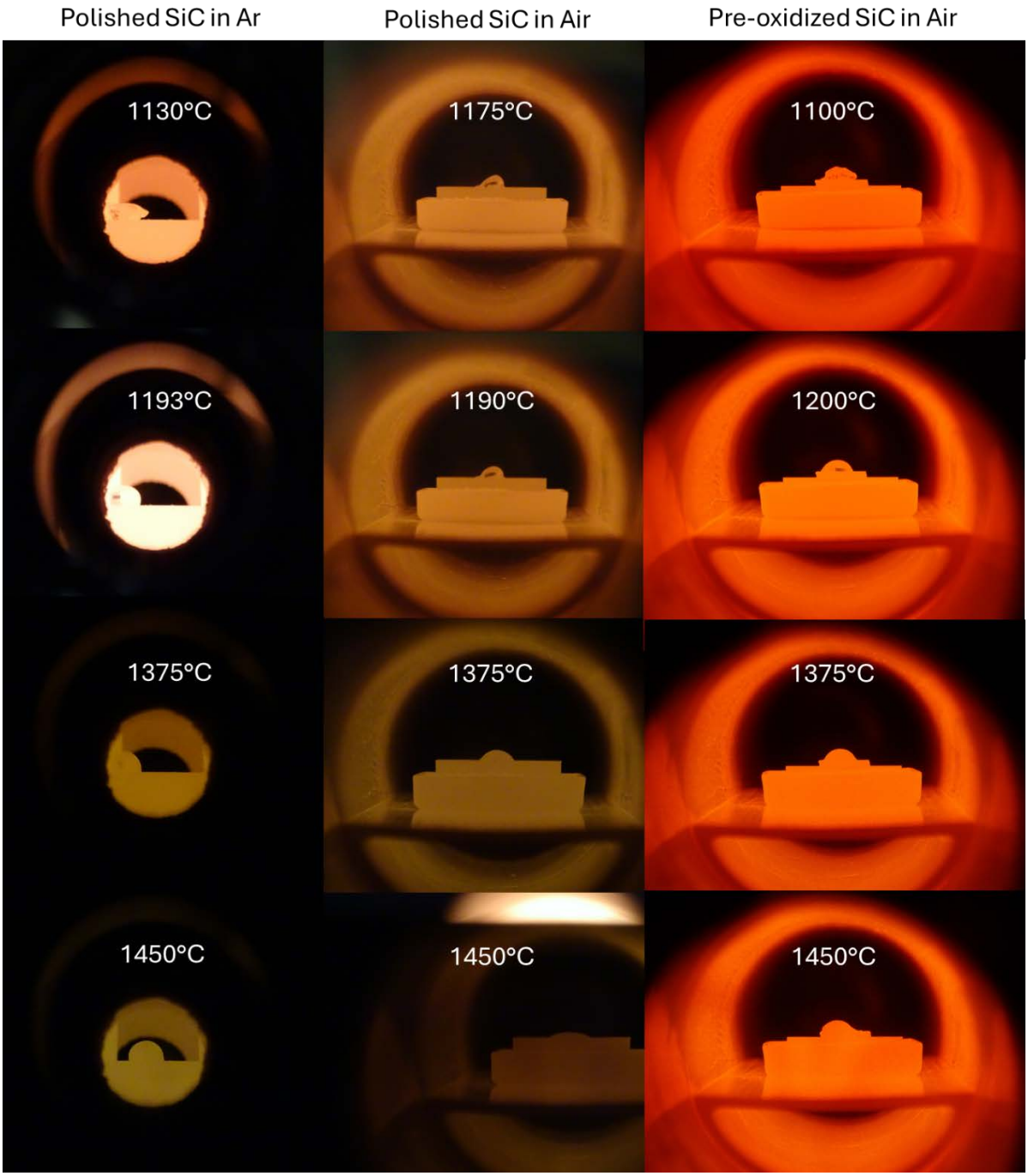

Figure 75. Images of the molten droplets of SAY glass ceramic on polished and pre-oxidized SiC during the wetting angle measurements in Ar and air atmosphere

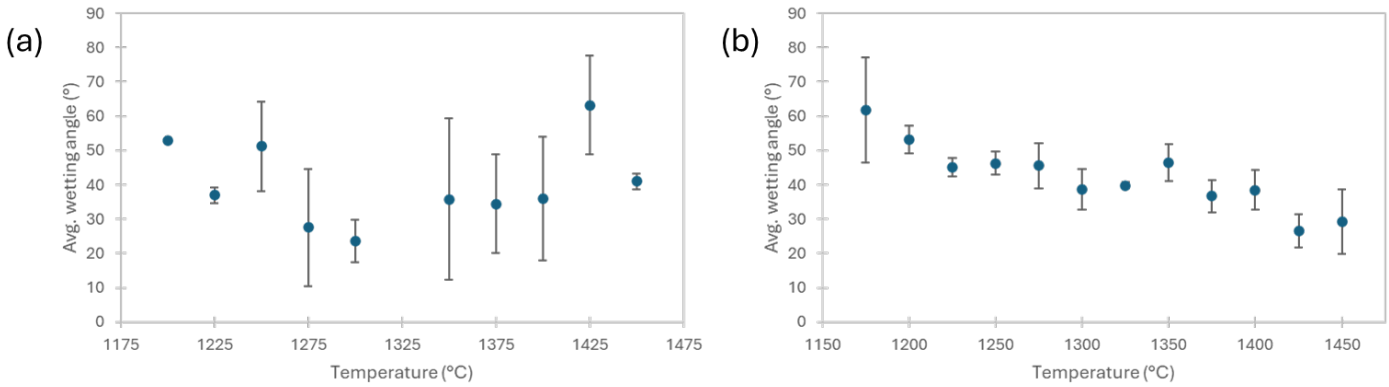

Figure 76. Average wetting angle of the SAY glass ceramic on (a) non-oxidized and (b) pre-oxidized SiC surface in air as a function of temperature

Figure 77 shows non-oxidized and pre-oxidized SiC substrates after the wetting experiments with the SAY glass ceramic in air. In Figure 77(a), Region 1 denotes SAY glass bead after the wetting experiment on the non-oxidized SiC substrate (Region 2). The white coloration in the middle was due to possible crystallization of the SAY glass melts, as determined by the XRD analysis shown in Figure 78 (left), where mullite and high-temperature cristobalite phases were observed. However, no evidence of $Y_2Si_2O_7$ phase was observed by XRD, although it was found by earlier SEM analysis on similar SAY samples as well as by Ahmad et al. [83]. As shown by Figure 78 (right), the remaining area of SiC surface (Region 2) had "cristobalite (low)" phase along with quartz as a minor phase on SiC surface, possibly due to migration of the silicon oxide species from the SAY droplet.

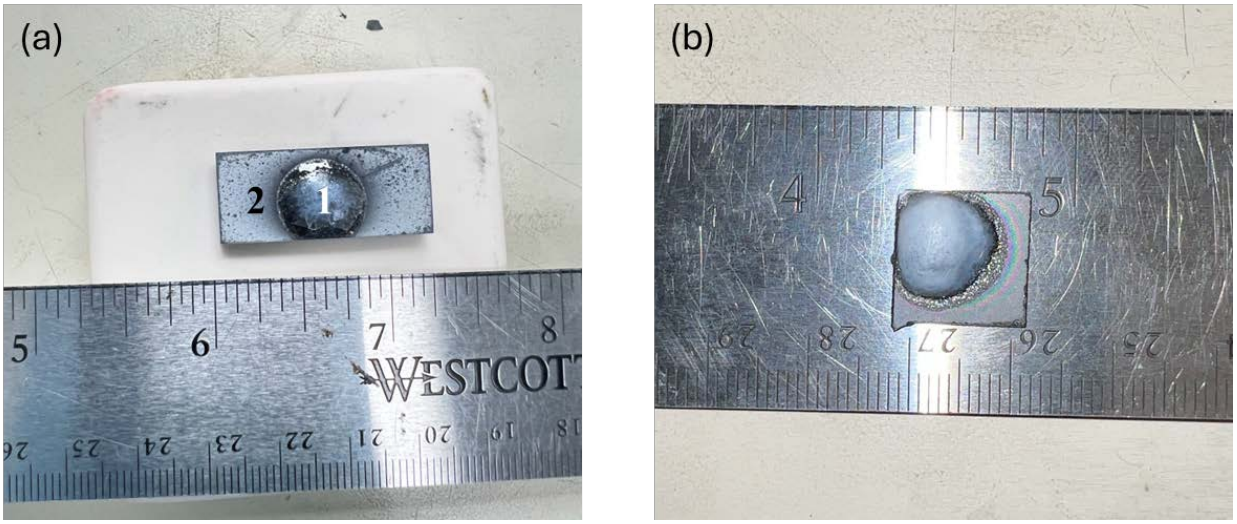

Figure 77. SAY glass on (a) non-oxidized and (b) pre-oxidized SiC substrates after the wetting experiment in air at 1,450°C for 1 hour

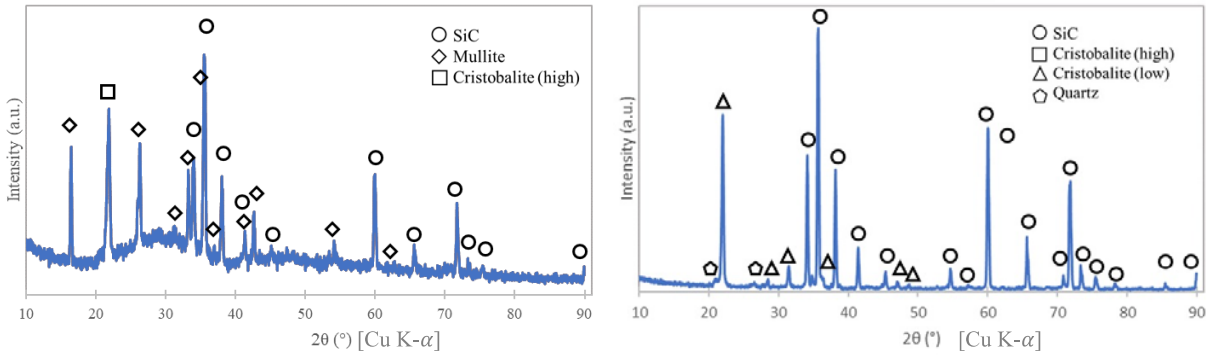

Figure 78. XRD data of Region 1 (left) and Region 2 (right) in Figure 77(a)

In summary, we are optimistic that surface pre-oxidation of the polished SiC could contribute to a stronger joint between SiC substrates, based on the literature and our own investigation. In addition, the non-oxidized SiC in Ar atmosphere confirmed a persistent issue with previous joining efforts, where some gaseous species formed during the joining process, likely from reaction between SiC and the constituents in the SAY glass (such as SiO_2 and Al_2O_3) based on the following chemical equations:

$$SiC(s) + 2SiO_2(l) \rightarrow 3SiO(g) + CO(g) \quad (4)$$

$$SiC(s) + Al_2O_3(l) \rightarrow Al_2O(g) + SiO(g) + CO(g) \quad (5)$$

The formation of air bubbles could compromise the strength of the joint. This leads to the investigation of the next processing parameter, i.e., the vacuum effect. We conducted additional thermodynamic investigation along with experimentation in Ar and vacuum atmosphere will be conducted to understand the source of the bubble formation.

2.5.2.4.2 Effect of Vacuum

We performed a few joining experiments where the non-oxidized and pre-oxidized SiC plates were joined in vacuum. The process used Ar atmosphere during heating until the temperature reached about 1,350°C (i.e., about 25°C below the reported melting point of the SAY glass ceramic) and pulled vacuum above 1,350°C. Vacuum was released and the process resumed in Ar atmosphere during cooling when the temperature dropped below 1350°C.

Because of the formation of surface SiO_2 on SiC during pre-oxidation, the pre-oxidized SiC plates were joined at a temperature of 1,425°C–1,450°C. The slightly higher temperature range than 1,400°C for non-oxidized SiC plate joining was used to compensate for the potential increase of the SAY glass ceramic's melting point at the joint interface due to the dissolution of the surface SiO_2 into the SAY glass melt. This has been noted in previous efforts, where a noticeable drop in joint strength from 50–60 MPa to <25 MPa was detected for pre-oxidized SiC processed at 1,400°C when compared to non-oxidized SiC processed under the same temperature condition. In contrast, no noticeable strength drop was detected when 1,450°C was used as a processing temperature.

The effect of the vacuum was observed in Figure 79. It is clear that the vacuum atmosphere was able to prevent large gas bubble formation. In the case of non-oxidized SiC, it was possible that

the large gas bubble initially formed below 1,350°C (i.e., when Ar atmosphere was used), which agreed with the wetting experiment results in Figure 75. Once vacuum was used at above 1,350°C, the large gas bubble collapsed, leading to the crater-like behavior. It was unknown why the crater-like behavior was not completely melted to form a smooth droplet. It is possible that the local melting point was not at 1,375°C. Hence, the processing temperature of 1,400°C was not sufficient to make the SAY glass ceramic fully molten. Similarly, vacuum atmosphere considerably changed the SAY glass droplet's behavior for pre-oxidized SiC at 1,425°C, where it formed a smooth glass droplet with a very low contact angle. Upon closer inspection by optical microscopy, there were still very small, trapped bubbles inside the glass ceramic, which could be the next focus of optimization. The findings from Figure 79 led to further investigation by mechanically testing joints made from pre-oxidized SiC processed at 1,425°C–1,450°C in vacuum.

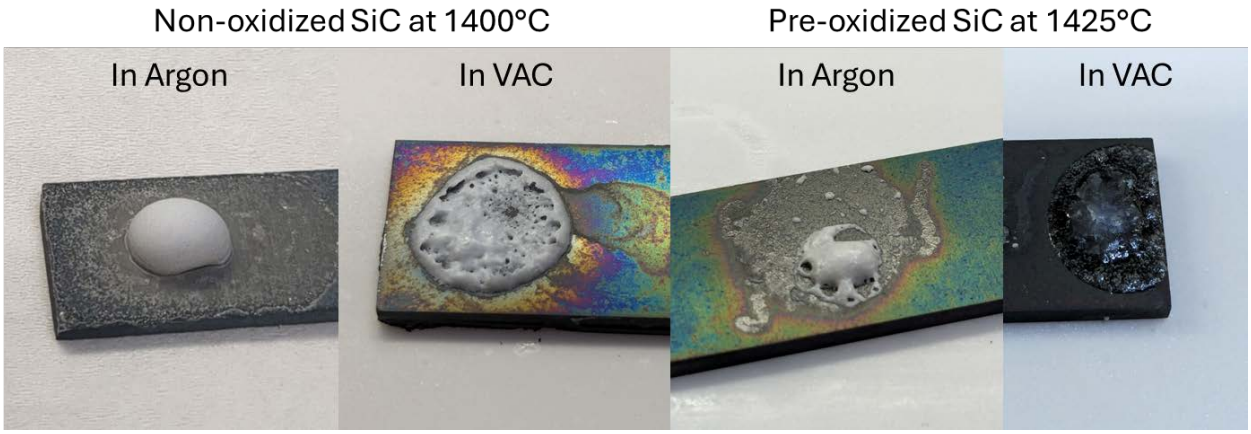

Figure 79. Comparison of gas bubble formation inside the SAY glass ceramic droplet on an SiC plate in Ar atmosphere versus in vacuum

2.5.2.5 Mechanical Strength Improvement for SAY Glass Ceramic

Table 22 summarizes the mechanical properties of the SAY joints as a function of the processing atmosphere and SiC surface treatment. The investigation in the previous section recommended surface pre-oxidation of SiC and a processing condition of 1,425°C in vacuum. The mechanical testing results agreed with the recommendation, as the highest shear strength of 106.2 MPa was obtained. Rigorous investigation would call for another measurement for pre-oxidized SiC in vacuum with a processing temperature of 1,450°C.

Table 22. Summary of Mechanical Properties of the SAY Joints as a Function of the Processing Atmosphere and SiC Surface Treatment

Processing Parameters				
Atmosphere	Ar		Vacuum	
Pre-oxidation	No	Yes	No	Yes
Mechanical Properties				
Processing temp. (°C)	Shear Strength (MPa)			
1,400	48.9, 62.2	23.1	68.5	N/A
1,425	N/A	N/A	N/A	106.2
1,450	40.0	43.2	77.0	TBD

The shear strength of about 106 MPa was competitive with other known SiC joining techniques. It was higher than the strength of most SiC-SiC joints made with glass ceramics reported in the literature. Only a few material systems had higher reported shear strengths, such as the Si-Cr and Si-Ti alloys via brazing (120–150 MPa) [96,97] and Mo and Ta-W alloys via diffusion bonding (120–130 MPa) [98,99]. Other material systems with higher reported shear strengths either used too-high joining temperatures (e.g., 1,800°C–1,900°C) that might damage the structure of the SiC_f-SiC CMCs or the reported strength will likely decrease considerably at high temperature based on the main joining phases (e.g., a low melting alloy). This was summarized by a recent review [55].

2.5.2.6 Scanning Transmission Electron Microscopy Analysis

The joint sample with 106 MPa shear strength was extensively characterized with scanning transmission electron microscopy (STEM). Figure 80 shows the rough location of the STEM sample prepared by focused ion beam (FIB) technique. The FIB sample included the bulk of the SiC, the bulk of the SAY glass ceramic, and the interface.

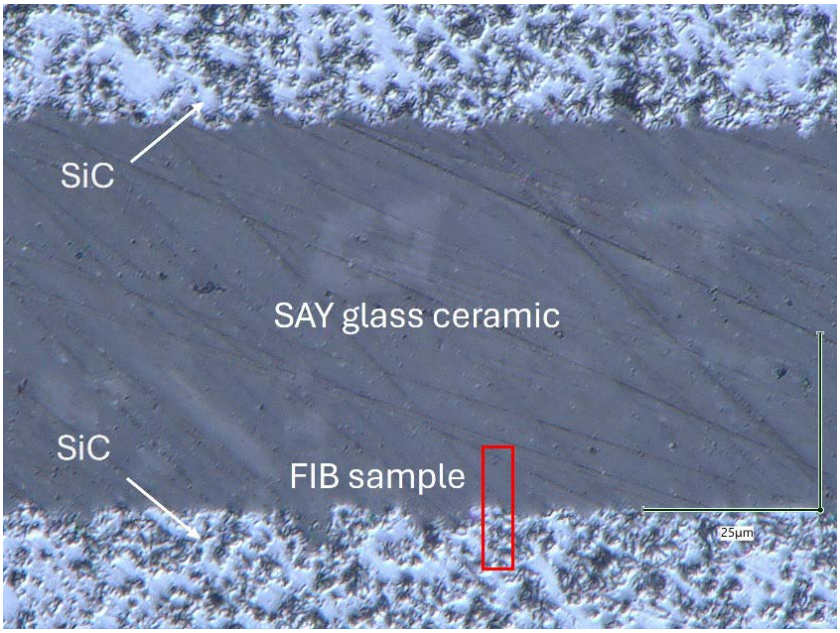

Figure 80. Optical microscopy image showing the rough location of the FIB sample for STEM analysis

Figure 81 shows the lower magnification (1,300x) darkfield TEM image at the interface between the SiC and SAY glass ceramic. It revealed an interface of about 200–250 nm in thickness, which confirmed that the SEM performed in the previous quarter did not have sufficient resolution to observe features of this magnitude.

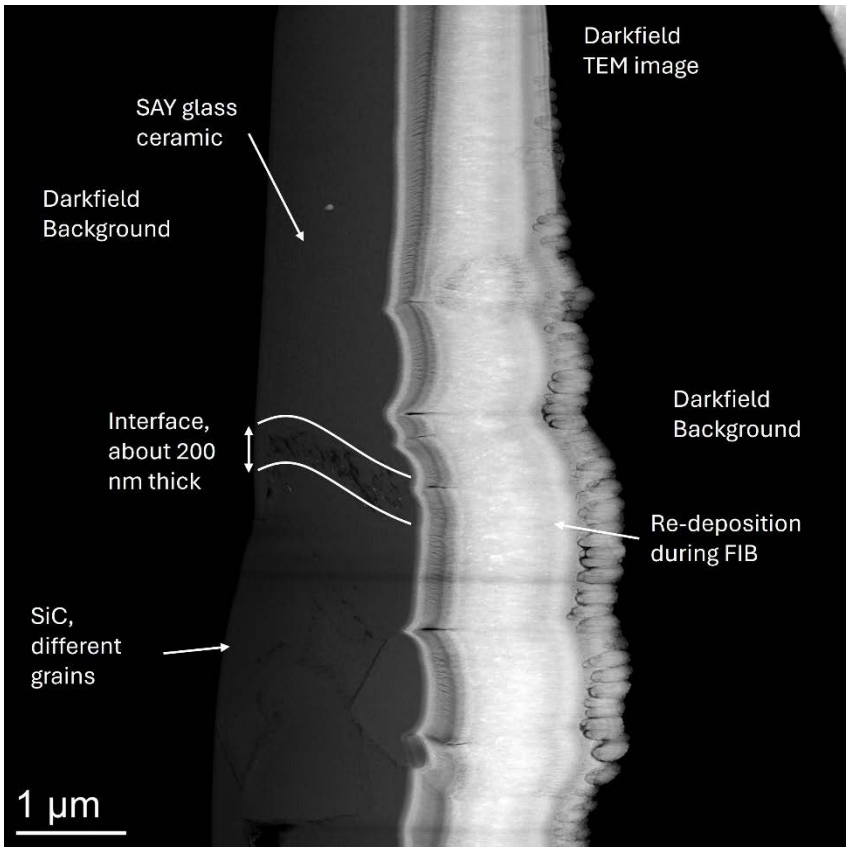

Figure 81. Darkfield TEM image at 1,300x at the interface between the SiC and SAY glass ceramic

Figure 82 (left) shows the higher magnification (17.5 kx) darkfield TEM image at the interface. Note that there might be a potential curtaining effect due to the FIB sample preparation [100], as shown by the spike-like features that were aligned at about 45°. This was likely due to the FIB's Ga ion beam hitting the interface region with a very different hardness from SAY glass ceramic to SiC. Figure 82 (right) shows the highest magnification (310 kx) darkfield TEM image at the interface.

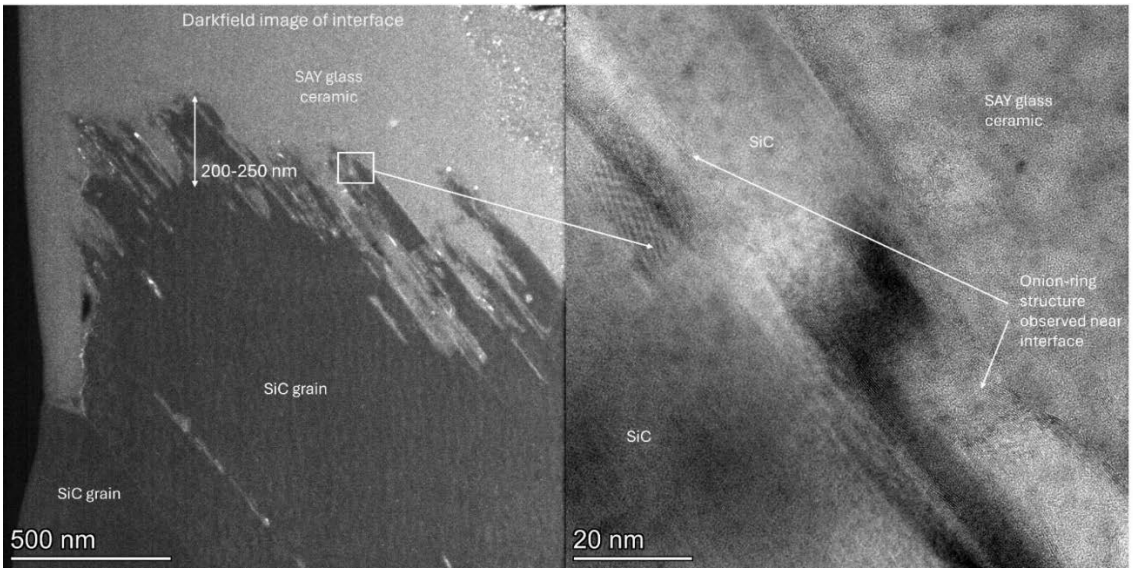

Figure 82. Darkfield TEM images at 17.5 kx (left) and 310 kx (right) at the SiC-SAY glass ceramic interface

A few observations are summarized below.

1. The transition from SAY glass ceramic to SiC was smooth and without obvious local defects such as porosities and cavities. The transition was within only a few nm, which agreed with the literature understanding.
2. Extensive onion-ring structures were observed throughout the SiC-SAY interface region. The onion-ring structures were typical of graphite and had been observed in oxidized SiC systems [101]. With electron diffraction and direct atomic spacing measurements, the lattice parameter was estimated to be about 0.34–0.35 nm, which was close to the interlayer distance of graphite (0.335 nm) [102].

We used EDS to confirm the chemical compositions of the interface regions. Figure 83 and Figure 84 show the elemental mapping from the EDS scans at 62 kx and 175 kx magnifications, respectively. It is clear that carbon concentrations existed at the SiC-SAY interface, and the transition from SAY glass ceramic to SiC was indeed at nm scale.

The origin of the carbon concentration has been investigated by the metal-oxide-semiconductor (MOS) field with extensive theory and supporting data. In summary, the oxidation of SiC into SiO_2 by O_2 (by breaking the Si-C bonds and forming Si-O bonds) is accompanied by the ejection of C atoms in the form of single C or CO interstitials. A fraction of the ejected C or CO can remain at the interface when oxidation stops [103–105]. Carbon/graphite clusters have been found [106–109]. The literature provides several theories regarding the origin of the carbon clusters, which concerns the surface treatment of the SiC before oxidation. Different experimental studies have shown the removal of the carbon clusters by a re-oxidation process at a lower temperature (e.g., 950°C) following the initial oxidation (at >1,100°C) in different atmospheres, including dry and moist oxygen/air [108, 113–116], N_2O [114,115] and H_2 [116], plasma cleaning [106,117], and ultraviolet treatment [109] of the SiC surface. Therefore, some of these methods were investigated to reduce the carbon concentration at the SiC-SAY interface.

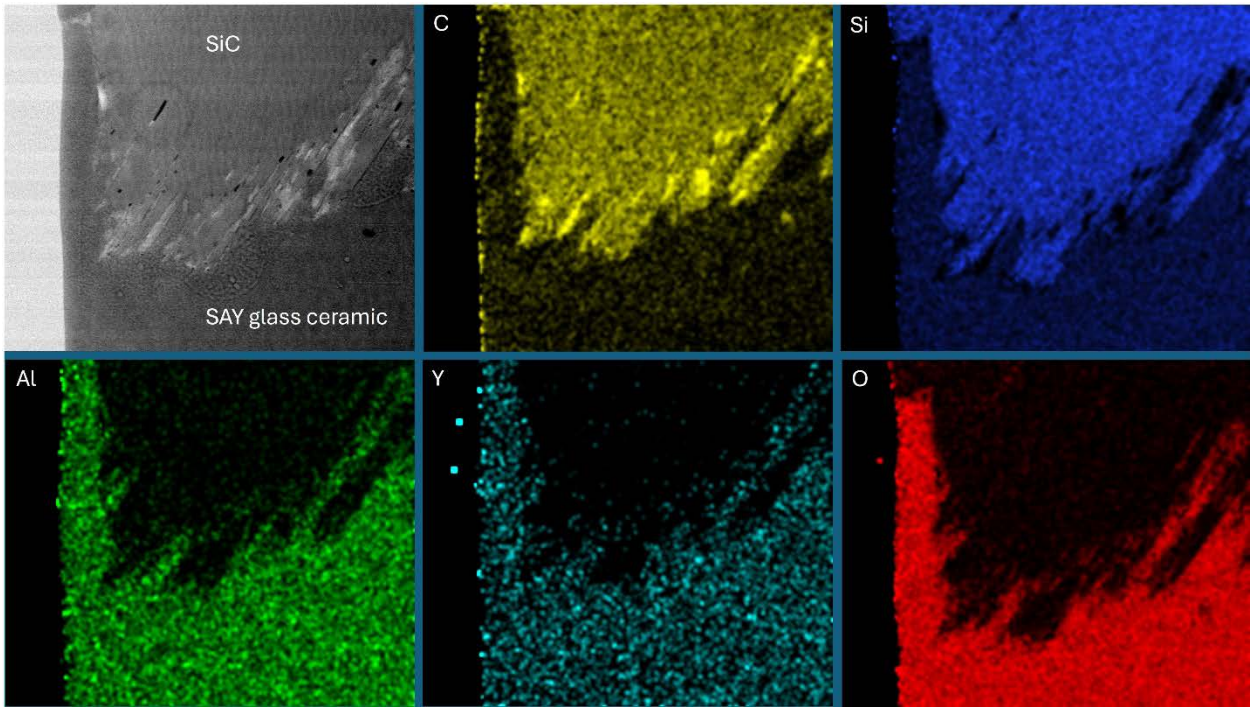

Figure 83. SEM image and EDS spectra for C, Si, Al, Y, and O at the SiC-SAY interface at 62 kx magnification

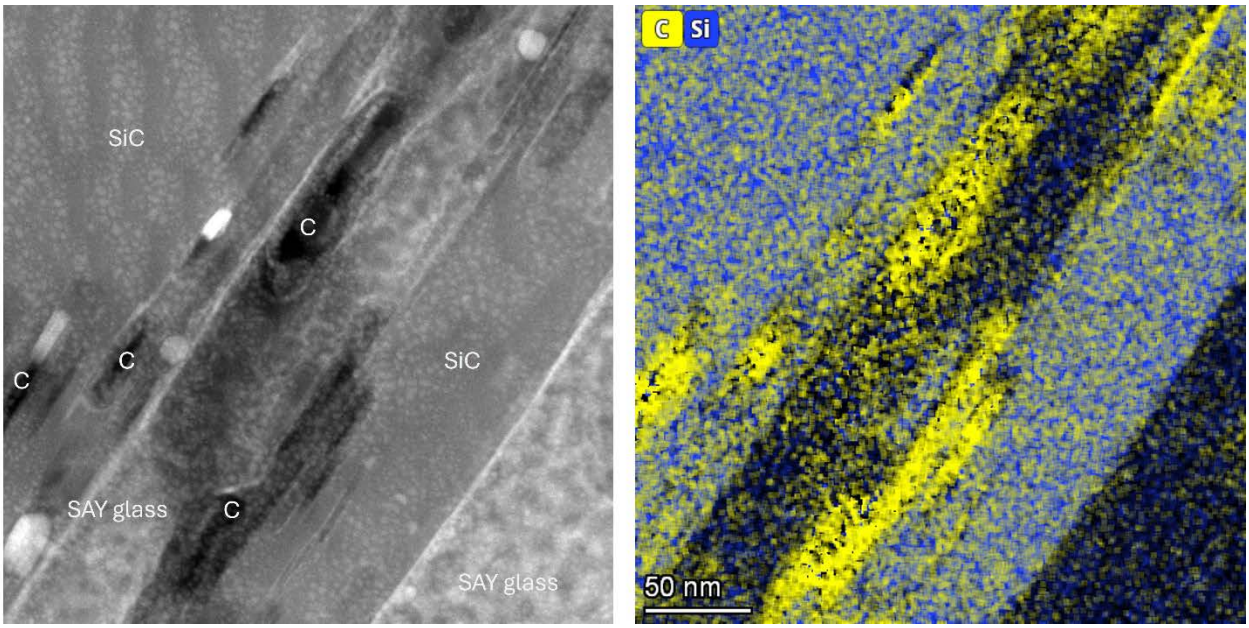

Figure 84. SEM image and EDS spectra for C and Si at the SiC-SAY interface at 175 kx magnification

The effect of carbon/graphite clusters on the bonding strength at the SiC-SAY interface was less known. Brennan and Nutt [101] investigated the crack propagation modes as a function of the carbon content at the interface between SiC whiskers and glass ceramics. An optimal carbon content was found to be correlated to the highest interfacial strength and fracture toughness due to

energy-dissipating processes such as interface debonding and crack bridging. On the other hand, if the carbon content was too high, the SiC-glass ceramic interface was expected to become too weak, affecting the overall interfacial strength. This was a main point of investigation next.

Figure 85 shows the compositions of the glassy phase in the SAY glass ceramic based on previous SEM and recent TEM characterizations. The compositions were reasonably consistent with each other, indicating consistent quality of the SAY glass ceramic and repeatable processing.

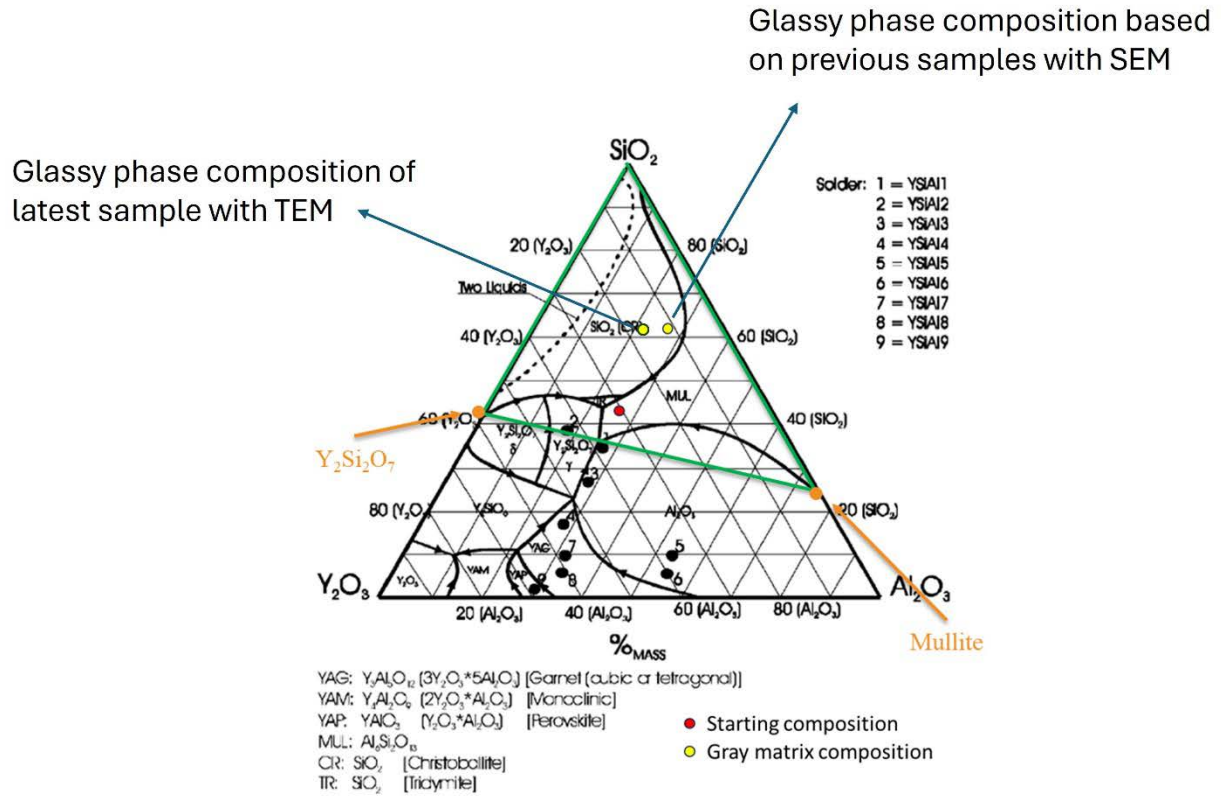

Figure 85. Compositions of the glassy phase in the SAY glass ceramic based on the EDS measurements from the SEM and TEM analyses

2.5.2.7 High-Temperature Hermiticity Tests

We performed hermiticity tests on a butt joint sample that was prepared under the same processing condition as the shear sample with 106 MPa strength (i.e., pre-oxidation of SiC plate at 1,300°C for 3 hours and joining at 1,425°C under vacuum atmosphere for 1 hour). The sample consisted of a ½-inch outer diameter Hexoloy SiC tube capped with a 1/16-inch-thick SiC plate. Given the nonstandard size of the SiC tubing (i.e., nominal ½-inch outer diameter but closer to 17/32–9/16 inches), standard tube connectors could not be directly used. Instead, a standard ½-inch Swagelok fitting was machined and modified to receive the nonstandard SiC tubing. A silicone O-ring was used to form the seal between the Swagelok fitting and the SiC tubing. Two thermocouples monitored the temperature of the joint (inside and outside of the SiC tubing). The outer thermocouple was also used to control the heating furnace. The experimental setup is shown in Figure 86.

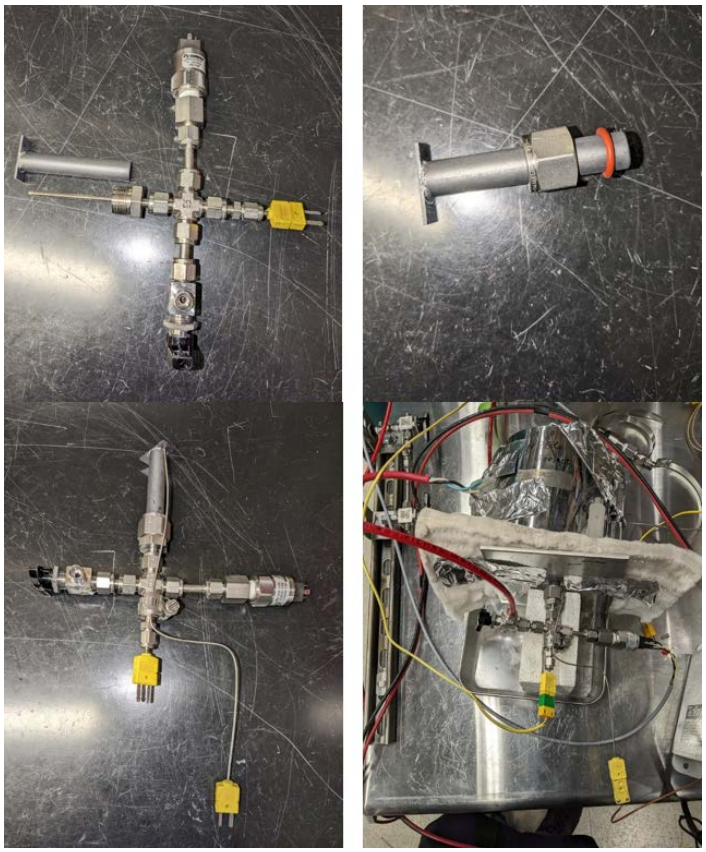

Figure 86. Experimental setup of the hermicity tests for the SAY glass ceramic butt joints

Pressure decay during the leak test indicates a gas leak, whereas a constant pressure (or a pressure increase) indicates gas hermiticity. It should be noted that because the gas was charged to the specimen at room temperature, whereas the SiC tube joint was at least partly at higher temperatures, pressure could increase if there was no leakage, simply because the temperature of the gas increased over time. The reading of the pressure transducers at temperatures up to 400°C is shown in Figure 87; the system exhibited slight pressure increase. Note that this test was performed at a pressure of 60 psia (or about 4 atm). The main finding was that the joint was gas-tight up to 400°C.

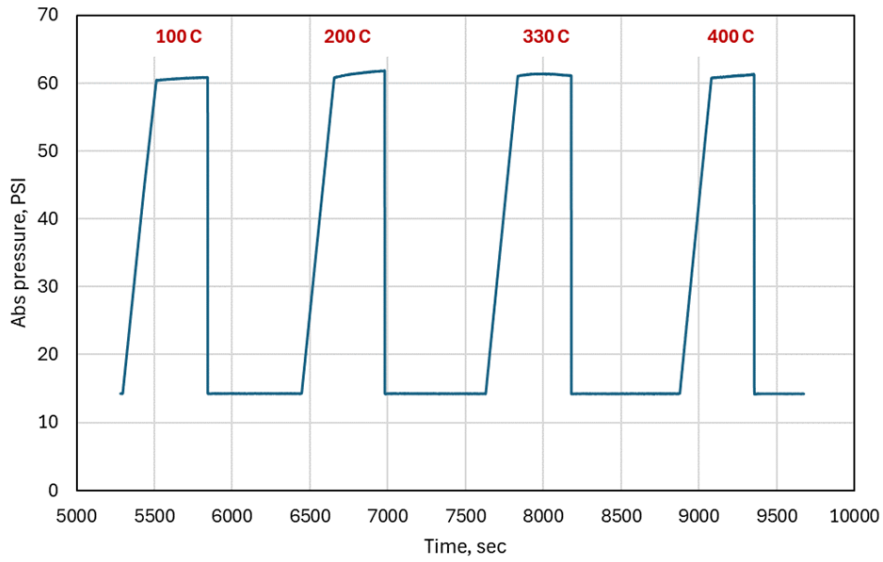

Figure 87. The pressure versus time relationship of the SAY glass butt joint during the hermiticity experiments up to 400°C

Figure 88 shows the pressure decay of higher-temperature hermiticity experiments for over 1 day of measurement time at each temperature. Given the 104-ml volume of the entire joint tube and its adjacent piping inside the hood, the leak rate was calculated to be less than 0.08 ml/min, which was considered very low, even for a full metallic piping system consisting of several Swagelok fittings. Note that the leak rate was not a function of joint temperature, confirming that the measured minimal leakage was likely related to the O-ring-sealed Swagelok fitting, which was always at room temperature, regardless of the measurement temperature.

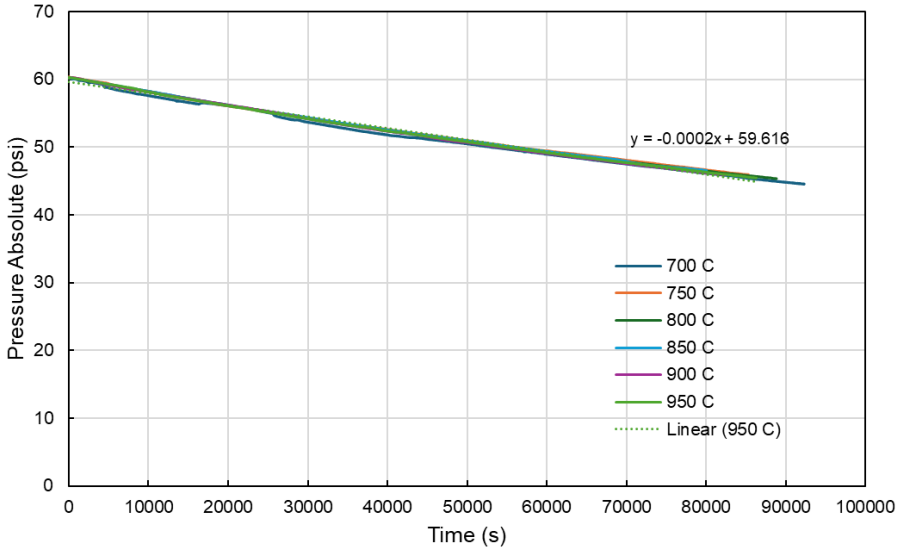

Figure 88. Pressure decay of higher-temperature hermiticity experiments for over 1 day of measurement time at each temperature

2.5.2.8 Joining Experiments Between Monolithic SiC and SiC_f-SiC CMC

As a key development step for the C2M joint concept, the joining between monolithic SiC and SiC-fiber-reinforced SiC (SiC_f-SiC) CMC must be demonstrated (see Figure ES1). A few SiC_f-SiC CMC tubes from Ceramic Tubular Products were sourced. These CMC tubes had a woven SiC fiber structure at ±45° angles, as shown by Figure 89. The ±45° angles were also suitable for future testing of the MPEA for bonding the SiC_f-SiC CMC transition tube to In740H, as the fibers at an angle (non-parallel) to the bonding interface were believed to provide stress relief.

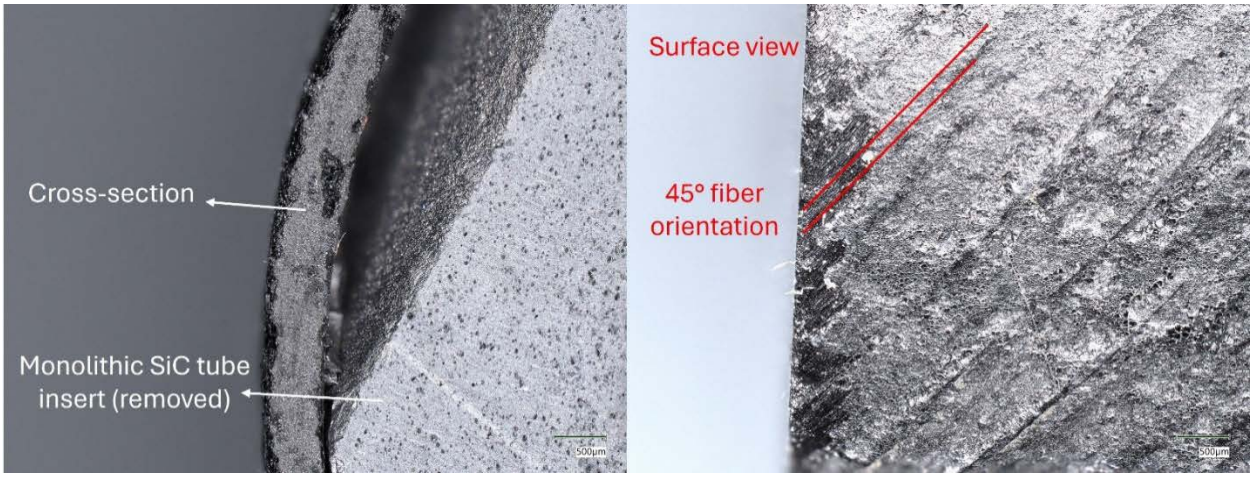

Figure 89. Cross section view and surface view of a SiC-fiber-reinforced SiC CMC tube

Figure 90 shows the schematic and a photo of the joint sample between the SiC_f-SiC CMC and a monolithic sintered SiC plate with a polished surface for characterization.

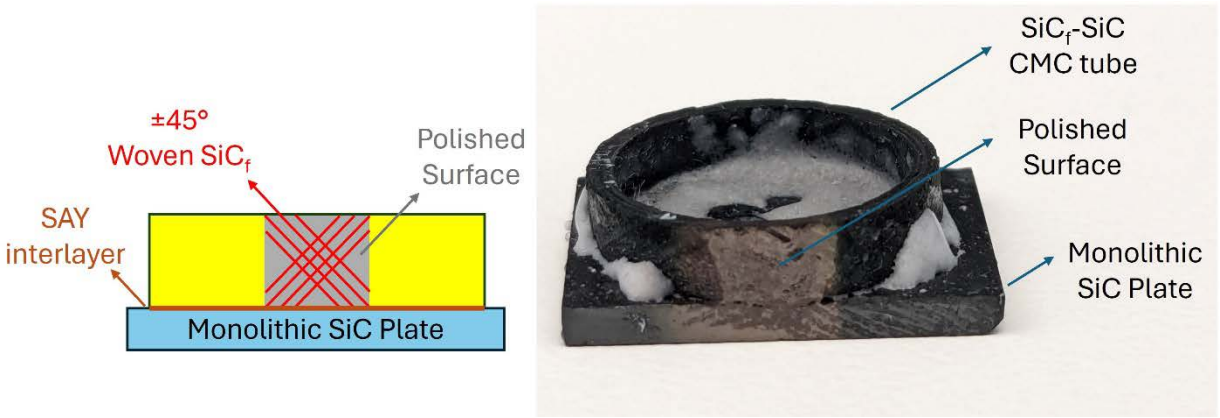

Figure 90. Schematic and photo of a joint between the SiC_f-SiC CMC and a monolithic sintered SiC plate

Figure 91 shows the SEM images of the cross section of the joint sample between a SiC_f-SiC CMC tube and a monolithic SiC plate heat treated at 1,400°C for 1 hour. It shows the ±45° woven SiC fiber orientation. Overall, the bonding between the SAY glass ceramic and the CMC was good. Some cavities near the bonding interface were observed. However, it was not clear whether they were caused by the polishing action, which might have caused some minor but noticeable damage to the interface. Also, as shown by Figure 89, the CMC was not 100% dense. Some cavities may

have been there prior to joining. Because these cavities were likely embedded inside the CMC, the SAY molten glass ceramic may not be able to reach them during the bonding process. However, wherever the SAY glass ceramic wetted the SiC fiber or the SiC matrix, the bonding seemed good (as shown by the 1,500x SEM image). The good bonding was consistent across most of the bonding interface with the CMC.

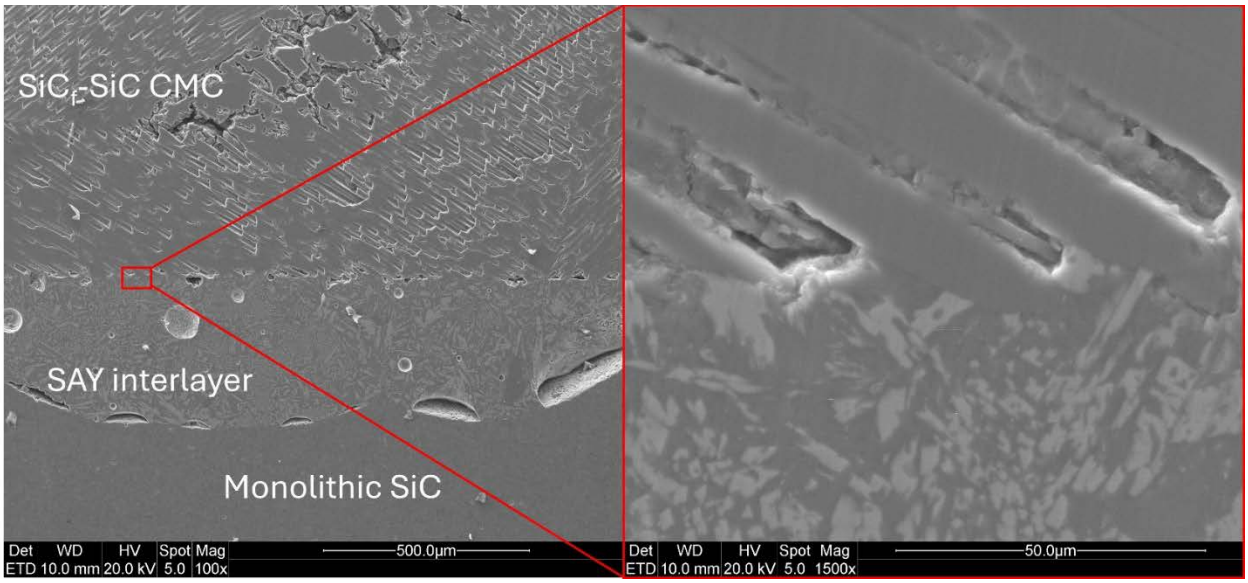

Figure 91. SEM images of the cross section of the joint sample between an SiC_f-SiC CMC and a monolithic SiC plate heat treated at 1,400°C for 1 hour

The phases within the SAY interlayer were very similar to those reported in Figure 72 and Table 20. The exception was that a few spot scans on the dark phases (dark phase I) did not match any known compositions. Because the SEM images could not adequtely distinguish subtle differences within the dark phases, other characterization techinques would be required.

Table 23. Summary of EDS Spot Scans for Different Phases and Area Scans in the SAY Glass Ceramic Interlayer for a Joint Between an SiC_f-SiC CMC and a Monolithic SiC Plate

Scan Locations	Wt.%		
	Al	Si	Y
Bright phase	1.96 ± 1.73%	29.36 ± 2.21%	68.68 ± 2.45%
Possible dark phase I	43.79 ± 4.20%	52.81 ± 4.04%	3.39 ± 0.17%
Possible dark phase II	25.66 ± 3.91%	63.92 ± 1.25%	10.43 ± 2.67%
Area scans	22.55 ± 0.37%	40.81 ± 0.08%	36.64 ± 0.29%
Reference Compositions			
Starting composition	22.83%	35.53%	41.64%
Mullite ($3Al_2O_3 \cdot 2SiO_2$)	74.24%	25.76%	N/A
Yttrium disilicate ($Y_2Si_2O_7$)	N/A	21.02%	78.98%

2.5.3 Liquid Phase Joining for SiC Ceramics Using Rare Earth Metals

When higher temperatures are required to make the SiC-end joint, a multi-step manufacturing process to create joints between heat exchangers and balance of plant may be used. We envisioned a two-step process, whereby the SiC CMC transition tube was first joined to the SiC heat exchanger at a high temperature, followed by a lower-temperature joining step between the transition tube and the In740H alloy piping. The drawback of the added complexity of a second heat treatment would be offset by the flexibility of process conditions that may be selected for ceramic-ceramic joining.

Transition metal elements such as Ni, Mo, Cr, and Au have been used to join SiC [118]. However, these transition metal elements have a lower solubility of carbon in their liquid phase compared to Si, which results in incongruent dissolution of SiC and formation of complex multiphase joining microstructures. Along with low carbon solubility, these transition metals form brittle silicides that are detrimental to the high-temperature mechanical strength of the joint [119]. Recently, rare earth element-based materials based on Y, Yb, Pr, or Dy have been proposed for SiC joining [120–123]. These elements have high solubility of carbon along with silicon, which promotes congruent dissolution and formation of SiC during the sintering process [124,125].

2.5.3.1 Literature Understanding of Rare Earth Metals for SiC Joining

Shi et al. [123] joined SiC using a sputtered Yb coating followed by SPS at temperatures ranging from 1,100°C–1,700°C for a duration of 10–15 minutes. According to Shi et al. [123], Yb reacted with the SiC substrate to form a $Yb_3Si_2C_2$ layer in accordance with Equation (6). The melting point of this carbide is about 1,275°C (based on the Yb-Si-C pseudo binary phase diagram from Reference [123]), and more thermodynamically stable SiC forms and precipitates out in the form of nanograins by decomposition of the $Yb_3Si_2C_2$ phase above its melting point.

$$Re + SiC \rightarrow Re_3Si_2C_2 \quad (6)$$

The excess liquid containing the Yb could react with the impurity oxygen content in the Ar atmosphere and/or oxygen from the silica surface layer of the silicon carbide to form YbO_x as well as YbO_xC_y as residual phases.

Shi et al. [123]. shows the back-scattered electron image of the cross section of the Yb joint interface and the low-magnification and high-magnification SEM images at temperatures between 1,200°C and 1,700°C. At 1,200°C, the joining layer was visible, as depicted by the bright region resulting from the higher atomic number of Yb-containing species compared to the SiC substrates. As the joining temperature increased to 1,500°C and 1,700°C, the joining interface became seamless. A thin and seamless joint could potentially reduce the residual thermal stress from the CTE mismatch.

The SEM analysis showed that a seamless joint was observed as the joining temperature increased. However, the four-point bending strength of the joint increased with temperature until 1,500°C and decreased at high temperatures. The joint was not established at 1,100°C, as the $Yb_3Si_2C_2$ did not form below 1,200°C. The higher temperature produced more liquid phases at the interlayer, which aided sintering via liquid phase sintering. In addition, higher temperatures resulted in larger grain size of the precipitated SiC from $Yb_3Si_2C_2$ melt, which affected the bending strength above 1,600°C. The joint processed at 1,500°C for 15 minutes resulted in a bending strength of 257 ±

31.1 MPa, which failed in the substrate region, while other lower temperature joints failed at the interface or between the interlayers.

Xu et al. [122] used Pr as a rare-earth metallic interlayer to join SiC substrates. The thickness of the Pr thin film was 100 nm. This thin film formed the $Pr_3Si_2C_2$ phase by in situ reaction with SiC at temperatures greater than 1,200°C. A four-point bend strength of 227 ± 12 MPa was achieved with a 1,400°C processing temperature. In the same study, different thicknesses of the metal thin film and their effect on the four-point strength were investigated at 1,500°C. For film thicknesses of 1 um, 300 nm, and 100 nm, the resulting four-point bend strengths were 186 ± 11 MPa, 201 ± 10 MPa, and 218 ± 13 MPa, respectively, with failure occurring at the interface or in the substrates. The increased mechanical strength was due to the smaller number of residual phases containing rare-earth metal after nano-SiC grain precipitation.

Alternative rare-earth elements were also reported for joining SiC. Similar to Yb-based joining, Y (melting point 1,526°C) reacts with SiC upon melting to form $Y_3Si_2C_2$ (melting point ~1,590°C). Liquid phase sintering of precipitated nanograin SiC and grains of SiC from the joining substrates establish the joint. Zhou et al. [121] explored SiC joining temperatures ranging from 1,300°C–1,900°C in Ar atmosphere with a heating and cooling rate of 100°C/min and a dwell time of 10 minutes. XRD analysis along with SEM images showed that the $Y_3Si_2C_2$ phase was stable at joining temperatures of 1,400°C and 1,500°C. This resulted in a reaction diffusion bonded joint. The joint strength increased from 1,400°C to 1,500°C owing to additional formation of the $Y_3Si_2C_2$ phase. Due to the presence of liquid at 1,600°C, the grain growth of the $Y_3Si_2C_2$ phase occurred, which reduced the joint. Further increasing the joining temperature to 1,800°C and 1,900°C resulted in additional strength increases from 113.9 ± 12.7 MPa and 134.8 ± 2.1 MPa, respectively.

2.5.3.2 Liquid Phase Joining for SiC Ceramics with Yb

Hot-pressing was first performed to form the SiC joint with a thin Yb interlayer (coated onto the SiC substrates via sputtering). However, due to the high vapor pressure of Yb at the hot-pressing temperature, a typical heating schedule resulted in significant Yb evaporation prior to the formation of a sound metallurgical bond. More rapid heating using SPS may be needed. However, the high electrical resistance of sintered SiC was a major challenge for the SPS technique.

We conducted experiments using 250-µm Y foil (99% purity) to verify literature reports of liquid phase formation with SiC. As-received Y foil was cut into 0.5-inch × 0.5-inch dimensions in a glove box to avoid oxidation. The Y foil was then sandwiched between polished surfaces of two SiC plates and loaded into a graphite hot press. A constant uniaxial load of 4 MPa was applied, and a joining temperature of 1,900°C with a heating and cooling rate of 100°C/min and a dwell time of 20 minutes was used. Two samples were retrieved from the hot press and visually examined. Evidence of liquid formation in the form of excess liquid squeezed from the joint interface is shown in Figure 92. The solidified excess Y was removed before mechanical strength measurement. A second sample processed under identical conditions was cross-sectioned using a low-speed diamond saw for SEM analysis. During cutting, water interacted with the solidified joint interface, which decomposed into powder after one day of subsequent exposure to air. Figure 93 shows the

joint surface after shear strength testing. The measured shear strength of the joint was 8.68 MPa, which was too low to produce a dense and strong joint.

Figure 92. SiC/Y-foil/SiC joint showing excess Y that was squeezed out of the joint interface

Figure 93. Joint surface of SiC/Y-foil/SiC after mechanical testing

To explain the low mechanical strength compared to the reported literature values, the working hypothesis was that the use of a graphite hot press allowed adequate diffusion of carbon to the joint region, perhaps before the reactions to establish the joint. The carbon diffusion promoted the formation of yttrium carbides, whose melting point exceeded that of elemental yttrium. The formation of the high-melting-point carbides prevented full melting and the formation of an SiC-rich liquid. Although limited solid-state interaction with SiC may have occurred, it did not provide enough bonding. To circumvent this issue, we proposed the following approaches:

1. Isolating the rare-earth elements and SiC joint region from excess carbon during hot pressing by using spacers (e.g., SiC plates) and/or a diffusion barrier (e.g., Mo foil).
2. Minimizing carbon transfer to the joint region by rapid sintering techniques. The application of SPS will require a shift from sintered SiC to a SiC with higher electrical conductivity (e.g., reaction-bonded SiC). The latter better reflects the chemistry of CMCs via melt infiltration, whereas the former reflects the chemistry of CMCs via chemical vapor infiltration.

The project team also planned to investigate the compositional design of rare-earth metals that can serve as transient liquid formers with goals to (1) maximize SiC congruent dissolution capacity at a maximum process temperature of 1,900°C, (2) minimize chemical sensitivity to moisture (i.e., via passivation with the addition of Si, Cr, Al, Nb, or Ta), and (3) minimize the tendency to form brittle precipitates during primary processing and cooling. Approaches to identify promising candidates were to be assessed, including machine-learning-based techniques informed by thermochemical CALPHAD databases.

3 Conclusions

The project aims to design a joining scheme where a SiC component is bonded to a transitional SiC-fiber-reinforced SiC CMC, which is subsequently bonded to the In740H component. The CMC is intended to mitigate the thermal stresses across the joint given its higher compliance.

With 2.5 years of research effort, the project suggests that:

- A TiMnFeNiCu-based MPEA filler has good chemical compatibility with SiC and In740H, and can potentially serve as the bonding agent.
- The most promising method to mitigate cracking in the SiC ceramic substrate when joined to In740H is to reduce the CTE mismatch between the filler and ceramic substrate with a graded MPEA-metal carbide MMC, where the metal carbide particles are used to tune the effective CTE at the bonding interface.
- A SiO_2-Al_2O_3-Y_2O_3 glass ceramic is a potential candidate for bonding the SiC component to the SiC-fiber-reinforced SiC CMC, as its processing temperature of about 1,400°C could avoid damage to the CMC structure.

Although this project made substantial progress on joining techniques for SiC-to-SiC bonds and SiC-to-In740H bonds, the ability of creating a reliable and robust C2M bond is yet to be demonstrated. First, a proper fabrication and joining technique for the MPEA-metal carbide MMC should be developed and validated. The technique should allow for mixing a changing ratio of carbide powders in the filler to form the MMC without compromising the bonding characteristics and mechanical properties. SPS is considered a top candidate technique because it can simultaneously sinter the MPEA-carbide MMC filler and join to SiC and In740H substrates in the solid state. Second, the complex chemistry at the SiC/glass ceramic interface needs further investigation to understand the effect of surface chemistry and treatment on the bonding qualities. In particular, the elimination of gaseous-species release during bonding (which may be responsible for porosity/cavity formation at the bonding interface), the transition from the Si-C bonds in the SiC substrate to the Si-O bonds in the glass ceramic, and the role of carbon species (as evidenced by the presence of graphitic carbon from the TEM analysis) at the bonding interface should be more thoroughly studied. Last but not least, the concept of using the CMC transition tube to mitigate thermal and mechanical stresses between the SiC and In740H components at bench scale must be successfully demonstrated.

References

[1] M.B. Uday, M.N. Ahmad-Fauzi, A.M. Noor, S. Rajoo, Current Issues and Problems in the Joining of Ceramic to Metal, in: Joining Technologies, InTech, 2016. https://doi.org/10.5772/64524.

[2] X. Yue, P. He, J.C. Feng, J.H. Zhang, F.Q. Zhu, Microstructure and interfacial reactions of vacuum brazing titanium alloy to stainless steel using an AgCuTi filler metal, Materials Characterization 59 (2008) 1721–1727. https://doi.org/10.1016/j.matchar.2008.03.014.

[3] W.S. Liu, Q.S. Cai, Y.Z. Ma, Y.Y. Wang, H.Y. Liu, D.X. Li, Microstructure and mechanical properties of diffusion bonded W/steel joint using V/Ni composite interlayer, Materials Characterization 86 (2013) 212–220. https://doi.org/10.1016/j.matchar.2013.10.013.

[4] Y. Zhu, D. Qi, W. Guo, H. Kang, P. Qu, The braze joint between Al_2O_3 to 1Cr18Ni9Ti using a nickel foam, Welding in the World 59 (2015) 491–496. https://doi.org/10.1007/s40194-015-0224-5.

[5] D.-H. Kuo, K.-T. Yeh, R.-K. Shiue, M.-H. Wei, Joining of Al_2O_3 to 316SS Using Braze-infiltrated Ni Net, ISIJ International 51 (2011) 1017–1019.

[6] W. Yang, P. He, T. Lin, C. Song, R. Li, D. Jia, Diffusion bonding of ZrB_2-SiC and Nb using dynamic compressed Ni foam interlayer, Materials Science and Engineering A 573 (2013) 1–6. https://doi.org/10.1016/j.msea.2013.02.047.

[7] M.L. Hattali, S. Valette, F. Ropital, G. Stremsdoerfer, N. Mesrati, D. Tréheux, Study of SiC-nickel alloy bonding for high temperature applications, Journal of the European Ceramic Society 29 (2009) 813–819. https://doi.org/10.1016/j.jeurceramsoc.2008.06.035.

[8] A.K. Jadoon, B. Ralph, P.R. Hornsby, Metal to ceramic joining via a metallic interlayer bonding technique, Journal of Materials Processing Technology 152 (2004) 257–265. https://doi.org/10.1016/j.jmatprotec.2003.10.005.

[9] M.G. Nicholas, R.M. Crispin, Diffusion bonding stainless steel to alumina using aluminium interlayers, Journal of Materials Science 17 (1982) 3347–3360. https://doi.org/10.1007/BF01203505.

[10] D. Travessa, M. Ferrante, G. den Ouden, Diffusion bonding of aluminium oxide to stainless steel using stress relief interlayers, Materials Science and Engineering A 337 (2002) 287–296. https://doi.org/10.1016/S0921-5093(02)00046-1.

[11] A.M. Kliauga, D. Travessa, M. Ferrante, Al_2O_3/Ti interlayer/AISI 304 diffusion bonded joint: Microstructural characterization of the two interfaces, Materials Characterization 46 (2001) 65–74. https://doi.org/10.1016/S1044-5803(00)00095-4.

[12] A.N. Winter, B.A. Corff, I.E. Reimanis, B.H. Rabin, Processing, Deformation, and Fracture of Ni- Al_2O_3 composites with and without Graded Microstructures, Ceramic Engineering and Science Proceedings 19 (1998) 379–386.

[13] A.N. Winter, B.A. Corff, I.E. Reimanis, B.H. Rabin, Fabrication of graded nickel-alumina composites with a thermal-behavior-matching process, Journal of the American Ceramic Society 83 (2000) 2147–2154. https://doi.org/10.1111/j.1151-2916.2000.tb01528.x.

[14] W.H. Tuan, H.H. Wu, R.Z. Chen, Effect of sintering atmosphere on the mechanical properties of Ni/ Al_2O_3 composites, Journal of the European Ceramic Society 17 (1997) 735–741. https://doi.org/10.1016/s0955-2219(96)00083-0.

[15] M. Bhattacharyya, A.N. Kumar, S. Kapuria, Synthesis and characterization of Al/SiC and Ni/ Al_2O_3 functionally graded materials, Materials Science and Engineering A 487 (2008) 524–535. https://doi.org/10.1016/j.msea.2007.10.040.

[16] T. Sekino, T. Nakajima, K. Niihara, Mechanical and magnetic properties of nickel dispersed alumina-based nanocomposite, Materials Letters 29 (1996) 165–169. https://doi.org/10.1016/S0167-577X(96)00136-X.
[17] V.G. Karayannis, A.K. Moutsatsou, Synthesis and characterization of nickel-alumina composites from recycled nickel powder, Advances in Materials Science and Engineering 2012 (2012). https://doi.org/10.1155/2012/395612.
[18] T. Sekino, J.-H. Yu, Y.-H. Choa, J.-S. Lee, K. Niihara, Reduction and Sintering of Alumina / Tungsten Nanocomposites, Journal of the Ceramic Society of Japan 547 (2000) 541–547.
[19] T. Sekino, K. Niihara, Fabrication and Mechanical Properties fo Fine-Tungsten-dispersed Alumina-based Composites, Journal of Materials Science 32 (1997) 3943–3949.
[20] T. Sekino, K. Niihara, Microstructural Characteristics and Mechanical Properties for Al_2O_3/Metal Nanocomposites, NanoStructured Materials 6 (1995) 663–666.
[21] R. Loehman, K. Ewsuk, A.P. Tomsia, Synthesis of Al_2O_3-Al Composites by Reactive Metal Penetration, Journal of American Ceramic Society 79 (1996) 27–32.
[22] M. Nawa, T. Sekino, K. Niihara, Fabrication and mechanical behaviour of Al_2O_3/Mo nanocomposites, Journal of Materials Science 29 (1994) 3185–3192. https://doi.org/10.1007/BF00356661.
[23] D.T. Rankin, J.J. Stiglicht, Hot-Pressing and Mechanical Properties of Al_2O_3 with an Mo-Dispersed Phase, (1971) 277–281.
[24] C.O. McHugh, T.J. Whalen, M.J. Humenik, Dispersion-Strengthened Aluminum Oxide, Journal of American Ceramic Society 49 (1966) 486–491.
[25] J.F. Bartolomé, M. Díaz, J. Requena, J.S. Moya, A.P. Tomsia, Mullite/molybdenum ceramic-metal composites, Acta Materialia 47 (1999) 3891–3899. https://doi.org/10.1016/S1359-6454(99)00220-7.
[26] I.W.M. Brown, W.R. Owers, Fabrication, microstructure and properties of Fe-TiC ceramic-metal composites, Current Applied Physics 4 (2004) 171–174. https://doi.org/10.1016/j.cap.2003.11.001.
[27] K.B. Panda, K.S. Ravi Chandran, Titanium-titanium boride (Ti-TiB) functionally graded materials through reaction sintering: Synthesis, microstructure, and properties, Metallurgical and Materials Transactions A: Physical Metallurgy and Materials Science 34 A (2003) 1993–2003. https://doi.org/10.1007/s11661-003-0164-3.
[28] A.A. Khan, J.C. Labbe, Aluminium nitride-molybdenum ceramic matrix composites: Influence of molybdenum concentration on the mechanical properties, Journal of Materials Science 32 (1997) 3829–3833. https://doi.org/10.1023/A:1018636025842.
[29] J.L. Huang, C.H. Li, Microstructure and mechanical properties of aluminum nitride—aluminum composite, Journal of Materials Research 9 (1994) 3153–3159. https://doi.org/10.1557/JMR.1994.3153.
[30] B.K. Deuser, Process planning and control of functionally graded parts using freeze-form extrusion fabrication, Missouri University of Science and Technology, 2012.
[31] L. Yang, H. Miyanaji, D.J. Ram, A. Zandinejad, S. Zhang, Functionally Graded Ceramic Based Materials using Additive Manufacturing: Review and Progress, in: Additive Manufacturing and Strategic Technologies in Advanced Ceramics: Ceramic Transactions, Volume 258, CCLVIII, 2016.
[32] W. Li, A.J. Martin, B. Kroehler, A. Henderson, T. Huang, J. Watts, G.E. Hilmas, M.C. Leu, Fabricating Functionally Graded Materials by Ceramic On-Demand Extrusion with

Dynamic Mixing, in: Proceedings of the 29th Annual International Solid Freeform Fabrication Symposium – An Additive Manufacturing Conference, 2018: pp. 1087–1099.
[33] W. Li, A. Armani, A. Martin, B. Kroehler, A. Henderson, T. Huang, J. Watts, G. Hilmas, M. Leu, Extrusion-based additive manufacturing of functionally graded ceramics, Journal of the European Ceramic Society 41 (2021) 2049–2057. https://doi.org/10.1016/j.jeurceramsoc.2020.10.029.
[34] M.C. Leu, B.K. Deuser, L. Tang, R.G. Landers, G.E. Hilmas, J.L. Watts, Freeze-form extrusion fabrication of functionally graded materials, CIRP Annals - Manufacturing Technology 61 (2012) 223–226. https://doi.org/10.1016/j.cirp.2012.03.050.
[35] N. Travitzky, A. Bonet, B. Dermeik, T. Fey, I. Filbert-Demut, L. Schlier, T. Schlordt, P. Greil, Additive Manufacturing of Ceramic-Based Materials, Advanced Engineering Materials 16 (2014) 729–754. https://doi.org/10.1002/adem.201400097.
[36] C. Ainsley, N. Reis, B. Derby, Freeform fabrication by controlled droplet deposition of powder filled melts, Journal of Materials Science 37 (2002) 3155–3161. https://doi.org/10.1023/A:1016106311185.
[37] Z. Fu, L. Schlier, N. Travitzky, P. Greil, Three-dimensional printing of SiSiC lattice truss structures, Materials Science and Engineering A 560 (2013) 851–856. https://doi.org/10.1016/j.msea.2012.09.107.
[38] L. Schlier, W. Zhang, N. Travitzky, P. Greil, J. Cypris, M. Weclas, Macro-cellular silicon carbide reactors for nonstationary combustion under piston engine-like conditions, International Journal of Applied Ceramic Technology 8 (2011) 1237–1245. https://doi.org/10.1111/j.1744-7402.2010.02591.x.
[39] X. Zhao, J.R.G. Evans, M.J. Edirisinghe, J.H. Song, Ink-jet printing of ceramic pillar arrays, Journal of Materials Science 37 (2002) 1987–1992. https://doi.org/10.1023/A:1015247131016.
[40] X. Zhao, J.R.G. Evans, M.J. Edirisinghe, J.H. Song, Direct ink-jet printing of vertical walls, Journal of the American Ceramic Society 85 (2002) 2113–2115. https://doi.org/10.1111/j.1151-2916.2002.tb00414.x.
[41] R. Melcher, N. Travitzky, C. Zollfrank, P. Greil, 3D printing of Al_2O_3/Cu-O interpenetrating phase composite, Journal of Materials Science 46 (2011) 1203–1210. https://doi.org/10.1007/s10853-010-4896-3.
[42] R. Melcher, S. Martins, N. Travitzky, P. Greil, Fabrication of Al_2O_3-based composites by indirect 3D-printing, Materials Letters 60 (2006) 572–575. https://doi.org/10.1016/j.matlet.2005.09.059.
[43] M. Mott, J.R.G. Evans, Zirconia/alumina functionally graded material made by ceramic ink jet printing, Materials Science and Engineering A 271 (1999) 344–352. https://doi.org/10.1016/s0921-5093(99)00266-x.
[44] P. Gingter, A.M. Wätjen, M. Kramer, R. Telle, Functionally graded ceramic structures by direct thermal inkjet printing, Journal of Ceramic Science and Technology 6 (2015) 119–124. https://doi.org/10.4416/JCST2014-00033.
[45] C. Kaya, Al_2O_3-Y-TZP/ Al_2O_3 functionally graded composites of tubular shape from nano-sols using double-step electrophoretic deposition, Journal of the European Ceramic Society 23 (2003) 1655–1660. https://doi.org/10.1016/S0955-2219(02)00370-9.
[46] J. Kastyl, Z. Chlup, F. Clemens, M. Trunec, Mechanical properties of zirconia core-shell rods with porous core and dense shell prepared by thermoplastic co-extrusion, Journal of

the European Ceramic Society 37 (2017) 2439–2447. https://doi.org/10.1016/j.jeurceramsoc.2017.02.006.
[47] PCC Energy Group, Inconel Alloy 740H - A Superalloy Specially Designed for Advanced Ultra Supercritical Power Generation, (n.d.).
[48] C.F. Zhe, Silicon Carbid - Materials, Processing & Devices, 1st ed., CRC Press, Boca Raton, 2003.
[49] B. Coddington, Joining Silicon Carbide to Metals Using Advanced Vacuum Brazing Technology, Journal of Student Research (1996) 30–42.
[50] J.W. Park, P.F. Mendez, T.W. Eagar, Strain energy release in ceramic-to-metal joints by ductile metal interlayers, Scripta Materialia 53 (2005) 857–861. https://doi.org/10.1016/j.scriptamat.2005.06.001.
[51] J.W. Park, P.F. Mendez, T.W. Eagar, Strain energy distribution in ceramic-to-metal joints, Acta Materialia 50 (2002) 883–899. https://doi.org/10.1016/S1359-6454(01)00352-4.
[52] C. duo Dai, R. na Ma, W. Wang, X. ming Cao, Y. Yu, Microstructure and properties of an Al–Ti–Cu–Si brazing alloy for SiC–metal joining, International Journal of Minerals, Metallurgy and Materials 24 (2017) 557–565. https://doi.org/10.1007/s12613-017-1437-y.
[53] M.C. Halbig, B.P. Coddington, R. Asthana, M. Singh, Characterization of silicon carbide joints fabricated using SiC particulate-reinforced Ag-Cu-Ti alloys, Ceramics International 39 (2013) 4151–4162. https://doi.org/10.1016/j.ceramint.2012.10.271.
[54] S. Kang, H.J. Kim, Design of High-Temperature Brazing Alloys for Ceramic-Metal Joints, Welding Journal 74 (1995) 289–295.
[55] G. Liu, X. Zhang, J. Yang, G. Qiao, Recent advances in joining of SiC-based materials (monolithic SiC and SiCf/SiC composites): Joining processes, joint strength, and interfacial behavior, Journal of Advanced Ceramics 8 (2019) 19–38. https://doi.org/10.1007/s40145-018-0297-x.
[56] E. Gomez, J. Echeberria, I. Iturriza, F. Castro, Liquid phase sintering of SiC with additions of Y_2O_3, Al_2O_3 and SiO_2, Journal of the European Ceramic Society 24 (2004) 2895–2903. https://doi.org/10.1016/j.jeurceramsoc.2003.09.002.
[57] S. Baud, F. Thévenot, A. Pisch, C. Chatillon, High temperature sintering of SiC with oxide additives: I. Analysis in the SiC– Al_2O_3 and SiC– Al_2O_3–Y_2O_3 systems, Journal of the European Ceramic Society 23 (2003) 1–8. https://doi.org/10.1016/S0955-2219(02)00067-5.
[58] A. Noviyanto, D.-H. Yoon, Rare-earth oxide additives for the sintering of silicon carbide, Diamond and Related Materials 38 (2013) 124–130. https://doi.org/10.1016/j.diamond.2013.07.003.
[59] Y. Jiang, L. Wu, Z. Wei, Z. Huang, Phase relations in the SiC– Al_2O_3–Y_2O_3 system, Materials Letters 165 (2016) 26–28. https://doi.org/10.1016/j.matlet.2015.11.101.
[60] F.K. van Dijen, E. Mayer, Liquid phase sintering of silicon carbide, Journal of the European Ceramic Society 16 (1996) 413–420. https://doi.org/10.1016/0955-2219(95)00129-8.
[61] S.N. Perevislov, A.S. Lysenkov, D.D. Titov, M.V. Tomkovich, Hot-pressed ceramic SiC–YAG materials, Inorg Mater 53 (2017) 220–225. https://doi.org/10.1134/S0020168517020091.
[62] S. Fan, J. Liu, X. Ma, Y. Wang, J. Hu, J. Deng, L. Cheng, L. Zhang, Microstructure and properties of SiCf/SiC joint brazed by Y-Al-Si-O glass, Ceramics International 44 (2018) 8656–8663. https://doi.org/10.1016/j.ceramint.2018.02.092.

[63] M. Ferraris, M. Salvo, V. Casalegno, A. Ciampichetti, F. Smeacetto, M. Zucchetti, Joining of machined SiC/SiC composites for thermonuclear fusion reactors, Journal of Nuclear Materials 375 (2008) 410–415. https://doi.org/10.1016/j.jnucmat.2008.02.020.
[64] M. Ferraris, V. Casalegno, S. Rizzo, M. Salvo, T.O. Van Staveren, J. Matejicek, Effects of neutron irradiation on glass ceramics as pressure-less joining materials for SiC based components for nuclear applications, Journal of Nuclear Materials 429 (2012) 166–172. https://doi.org/10.1016/j.jnucmat.2012.05.035.
[65] W. Lippmann, J. Knorr, R. Wolf, R. Rasper, H. Exner, A.-M. Reinecke, M. Nieher, R. Schreiber, Laser joining of silicon carbide—a new technology for ultra-high temperature resistant joints, Nuclear Engineering and Design 231 (2004) 151–161. https://doi.org/10.1016/j.nucengdes.2004.03.002.
[66] M. Herrmann, S. Ahmad, W. Lippmann, H.-J. Seifert, A. Hurtado, Rare earth (RE: Nd, Dy, Ho, Y, Yb, and Sc) aluminosilicates for joining silicon carbide components, International Journal of Applied Ceramic Technology 14 (2017) 675–691. https://doi.org/10.1111/ijac.12692.
[67] M. Gao, B. Schneiderman, S.M. Gilbert, Z. Yu, Microstructural Evolution and Mechanical Properties of Nickel-Base Superalloy Brazed Joints Using a MPCA Filler, Metallurgical and Materials Transactions A: Physical Metallurgy and Materials Science 50 (2019) 5117–5127. https://doi.org/10.1007/s11661-019-05386-8.
[68] A. McKinley, R.H. Williams, A.W. Parke, An investigation of thin silver films on cleaved silicon surfaces, Journal of Physics C: Solid State Physics 12 (1979) 2447–2463. https://doi.org/10.1088/0022-3719/12/12/030.
[69] T. Telmasre, Development of MPEA filler for dissimilar joining of steel to titanium alloy and evaluation of strength of brazed joints, Colorado School of Mines, 2021.
[70] J. Belan, GCP and TCP Phases Presented in Nickel-base Superalloys, Materials Today: Proceedings 3 (2016) 936–941. https://doi.org/10.1016/j.matpr.2016.03.024.
[71] M. Gao, Development of New High Entropy Alloys, Colorado School of Mines, 2017.
[72] P. Nikolopoulos, S. Agatho Pou Los, G.N. Angelopoulos, A. Naoumidis, H. Grübmeier, Wettability and interfacial energies in SiC-liquid metal systems, Journal of Materials Science 27 (1992) 139–145. https://doi.org/10.1007/BF02403656.
[73] R. Asthana, M. Singh, Active metal brazing of advanced ceramic composites to metallic systems, in: Advances in Brazing - Science, Technology and Applications, Woodhead Publishing Limited, 2013: pp. 323–360.
[74] K. Suganuma, T. Okamoto, K. Kamachi, Influence of shape and size on residual stress in ceramic/metal joining, J Mater Sci 22 (1987) 2702–2706. https://doi.org/10.1007/BF01086460.
[75] W. Wang, Y. Wang, J. Huang, Z. Ye, J. Yang, S. Chen, X. Zhao, Reaction-composite diffusion brazing of C-SiC composite and Ni-based superalloy using mixed (Cu-Ti)+C powder as an interlayer, Journal of Materials Processing Technology 300 (2022) 117419. https://doi.org/10.1016/j.jmatprotec.2021.117419.
[76] A. Takeuchi, A. Inoue, Classification of Bulk Metallic Glasses by Atomic Size Difference, Heat of Mixing and Period of Constituent Elements and Its Application to Characterization of the Main Alloying Element, Materials Transactions 46 (2005) 2817–2829. https://doi.org/10.2320/matertrans.46.2817.
[77] H.J.T. Ellingham, Reducibility of oxides and sulphides in metallurgical processes., Society of Chemical Industry, 1944.

[78] W. Acchar, U.U. Gomes, W.A. Kaysser, J. Goring, Strength Degradation of a Tungsten Carbide-Cobalt Composite at Elevated Temperatures, Materials Characterization 43 (1999) 27–32. https://doi.org/10.1016/S1044-5803(98)00056-4.
[79] V.L. Silva, C.M. Fernandes, A.M.R. Senos, Copper wettability on tungsten carbide surfaces, Ceramics International 42 (2016) 1191–1196. https://doi.org/10.1016/j.ceramint.2015.09.050.
[80] P. Wu, C.Z. Zhou, X.N. Tang, Microstructural characterization and wear behavior of laser cladded nickel-based and tungsten carbide composite coatings, Surface and Coatings Technology 166 (2003) 84–88. https://doi.org/10.1016/S0257-8972(02)00730-2.
[81] R.R. Reeber, K. Wang, Thermophysical Properties of α-Tungsten Carbide, Journal of the American Ceramic Society 82 (1999) 129–135. https://doi.org/10.1111/j.1151-2916.1999.tb01732.x.
[82] R. Bouaita, Impact des conditions de cristallisation sur les défauts et les contraintes résiduelles dans le saphir et cristallisation par µ-PD de fibres de grenats YAG-dopées Ce pour la physique des hautes énergies, phdthesis, Université de Lyon ; Université Badji Mokhtar-Annaba, 2019. https://theses.hal.science/tel-02440657 (accessed July 16, 2024).
[83] S. Ahmad, M. Herrmann, M.M. Mahmoud, H. Leiste, W. Lippmann, H.J. Seifert, Crystallisation studies of RE_2O_3–Al_2O_3–SiO_2 glasses under long heat-treatment conditions, Journal of Alloys and Compounds 688 (2016) 762–774. https://doi.org/10.1016/j.jallcom.2016.07.267.
[84] Z. Li, R.C. Bradt, Thermal expansion of the cubic (3C) polytype of SiC, J Mater Sci 21 (1986) 4366–4368. https://doi.org/10.1007/BF01106557.
[85] R.M. Brannon, M.Y. Lee, D.R. Bronowski, Uniaxial and triaxial compression tests of silicon carbide ceramics under quasi-static loading condition., Sandia National Laboratories (SNL), Albuquerque, NM, and Livermore, CA (United States), 2005. https://doi.org/10.2172/920770.
[86] F.A. Mir, N.Z. Khan, S. Parvez, Recent advances and development in joining ceramics to metals, Materials Today: Proceedings 46 (2020) 6570–6575. https://doi.org/10.1016/j.matpr.2021.04.047.
[87] S. Baud, F. Thévenot, C. Chatillon, High temperature sintering of SiC with oxide additives: II. Vaporization processes in powder beds and gas-phase analysis by mass spectrometry, Journal of the European Ceramic Society 23 (2003) 9–18. https://doi.org/10.1016/S0955-2219(02)00068-7.
[88] S. Baud, F. Thévenot, C. Chatillon, High temperature sintering of SiC with oxide additives: III. Quantitative vaporization of SiC– Al_2O_3 powder beds as revealed by mass spectrometry, Journal of the European Ceramic Society 23 (2003) 19–27. https://doi.org/10.1016/S0955-2219(02)00069-9.
[89] S. Baud, F. Thévenot, C. Chatillon, High temperature sintering of SiC with oxide additives: IV. Powder beds and the influence of vaporization on the behaviour of SiC compacts, Journal of the European Ceramic Society 23 (2003) 29–36. https://doi.org/10.1016/S0955-2219(02)00070-5.
[90] H.-C. Lee, S. Dhage, M.S. Akhtar, D.H. Kwak, W.J. Lee, C.-Y. Kim, O.-B. Yang, A simulation study on the direct carbothermal reduction of SiO_2 for Si metal, Current Applied Physics 10 (2010) S218–S221. https://doi.org/10.1016/j.cap.2009.11.053.

[91] Z. Sun, X. Chen, Y. Mao, L.X. Zhang, J.C. Feng, Joining of SiC ceramics using CaO-Al_2O_3-SiO_2 (CAS) glass ceramics, Journal of the European Ceramic Society 40 (2020) 267–275. https://doi.org/10.1016/j.jeurceramsoc.2019.09.030.
[92] S.-J. He, J.-P. Chen, W.-M. Guo, X.-B. Chen, H. Zhou, C.-T. Zhan, S.-K. Sun, Y. Li, L.-X. Wu, J.-X. Xue, H.-T. Lin, Improvement of the shear strength of SiC joint with CaO–Al_2O_3–MgO–SiO_2 glass filler by surface etching, Ceramics International (2024). https://doi.org/10.1016/j.ceramint.2024.01.419.
[93] L. Sun, S. Wang, C. Hou, D. Wang, C. Liu, X. Zhang, J. Zhang, Microstructure, mechanical property and bonding mechanism of SiC ceramic joint using a novel $Y_2Si_2O_7$/Mullite glass-ceramic interlayer, Ceramics International 49 (2023) 17885–17893. https://doi.org/10.1016/j.ceramint.2023.02.155.
[94] J. Fang, L. Sun, S. Guo, T. Shan, Y. Wen, C. Liu, J. Zhang, Wetting and joining of surface-oxidized SiC ceramic with calcium lithium aluminosilicate glass filler, Applied Surface Science 568 (2021) 150951. https://doi.org/10.1016/j.apsusc.2021.150951.
[95] T. Shan, L. Sun, C. Liu, J. Fang, Z. Li, Y. Wen, B. Wang, S. Guo, J. Zhang, Microstructure and mechanical properties of SiC joint using anorthite based glass-ceramic and first principles calculation of joint interface, Ceramics International 49 (2023) 40149–40157. https://doi.org/10.1016/j.ceramint.2023.09.348.
[96] L.I. Jia-Ke, L.I.U. Lei, L.I.U. Xin, Joining of SiC Ceramic by 22Ti-78Si High-temperature Eutectic Brazing Alloy, Journal of Inorganic Materials 26 (2011) 1314.
[97] B. Riccardi, C. a. Nannetti, J. Woltersdorf, E. Pippel, T. Petrisor, Joining of SiC based ceramics and composites with Si-16Ti and Si-18Cr eutectic alloys, International Journal of Materials and Product Technology 20 (2004) 440–451. https://doi.org/10.1504/IJMPT.2004.004778.
[98] H.X. Li, Z.H. Zhong, H.B. Zhang, Z.X. Zhu, P. Hua, C. Chen, Y.C. Wu, Microstructure characteristic and its influence on the strength of SiC ceramic joints diffusion bonded by spark plasma sintering, Ceramics International 44 (2018) 3937–3946. https://doi.org/10.1016/j.ceramint.2017.11.185.
[99] B.V. Cockeram, Flexural strength and shear strength of silicon carbide to silicon carbide joints fabricated by a molybdenum diffusion bonding technique, Journal of the American Ceramic Society 88 (2005) 1892–1899. https://doi.org/10.1111/j.1551-2916.2005.00381.x.
[100] T.H. Loeber, B. Laegel, S. Wolff, S. Schuff, F. Balle, T. Beck, D. Eifler, J.H. Fitschen, G. Steidl, Reducing curtaining effects in FIB/SEM applications by a goniometer stage and an image processing method, Journal of Vacuum Science & Technology B 35 (2017) 06GK01. https://doi.org/10.1116/1.4991638.
[101] J.J. Brennan, S.R. Nutt, SiC-Whisker-Reinforced Glass-Ceramic Composites: Interfaces and Properties, Journal of the American Ceramic Society 75 (1992) 1205–1216. https://doi.org/10.1111/j.1151-2916.1992.tb05559.x.
[102] H. Tu, L. Ye, Thermal conductive PS/graphite composites, Polymers for Advanced Technologies 20 (2009) 21–27. https://doi.org/10.1002/pat.1236.
[103] S. Wang, S. Dhar, S. Wang, A.C. Ahyi, A. Franceschetti, J.R. Williams, L.C. Feldman, S.T. Pantelides, Bonding at the SiC−SiO_2Interface and the Effects of Nitrogen and Hydrogen, Phys. Rev. Lett. 98 (2007) 026101. https://doi.org/10.1103/PhysRevLett.98.026101.

[104] S. Wang, M. Di Ventra, S.G. Kim, S.T. Pantelides, Atomic-Scale Dynamics of the Formation and Dissolution of Carbon Clusters in SiO_2, Phys. Rev. Lett. 86 (2001) 5946–5949. https://doi.org/10.1103/PhysRevLett.86.5946.
[105] L.A. Lipkin, J.W. Palmour, Improved oxidation procedures for reduced SiO_2/SiC defects, J. Electron. Mater. 25 (1996) 909–915. https://doi.org/10.1007/BF02666657.
[106] V.V. Afanas'ev, A. Stesmans, M. Bassler, G. Pensl, M.J. Schulz, C.I. Harris, Elimination of SiC/SiO_2 interface states by preoxidation ultraviolet-ozone cleaning, Applied Physics Letters 68 (1996) 2141–2143. https://doi.org/10.1063/1.115611.
[107] V.V. Afanasev, M. Bassler, G. Pensl, M. Schulz, Intrinsic SiC/SiO_2 Interface States, Physica Status Solidi (a) 162 (1997) 321–337. https://doi.org/10.1002/1521-396X(199707)162:1<321::AID-PSSA321>3.0.CO;2-F.
[108] V.V. Afanas'ev, F. Ciobanu, S. Dimitrijev, G. Pensl, A. Stesmans, Band alignment and defect states at SiC/oxide interfaces, J. Phys.: Condens. Matter 16 (2004) S1839. https://doi.org/10.1088/0953-8984/16/17/019.
[109] C. Wang, J. Xu, S. Guo, Q. Kang, Y. Wang, Y. Wang, Y. Tian, A facile method for direct bonding of single-crystalline SiC to Si, SiO_2, and glass using VUV irradiation, Applied Surface Science 471 (2019) 196–204. https://doi.org/10.1016/j.apsusc.2018.11.239.
[110] C. Jeong, K. Kim, The Effects of Boron Passivation and Re-Oxidation on the Properties of the 4H-SiC/SiO_2 Interface, J. Korean Phys. Soc. 74 (2019) 679–683. https://doi.org/10.3938/jkps.74.679.
[111] H. Yan, R. Jia, X. Tang, Q. Song, Y. Zhang, Effect of re-oxidation annealing process on the SiO_2 /SiC interface characteristics, J. Semicond. 35 (2014) 066001. https://doi.org/10.1088/1674-4926/35/6/066001.
[112] T. Akiyama, S. Hori, K. Nakamura, T. Ito, H. Kageshima, M. Uematsu, K. Shiraishi, Reaction mechanisms at 4H-SiC/SiO_2 interface during wet SiC oxidation, Jpn. J. Appl. Phys. 57 (2018) 04FR08. https://doi.org/10.7567/JJAP.57.04FR08.
[113] D.A. Newsome, D. Sengupta, H. Foroutan, M.F. Russo, A.C.T. van Duin, Oxidation of Silicon Carbide by O_2 and H_2O: A ReaxFF Reactive Molecular Dynamics Study, Part I, J. Phys. Chem. C 116 (2012) 16111–16121. https://doi.org/10.1021/jp306391p.
[114] L.A. Lipkin, M.K. Das, J.W. Palmour, N2O Processing Improves the 4H-SiC:SiO_2 Interface, Materials Science Forum 389–393 (2002) 985–988. https://doi.org/10.4028/www.scientific.net/MSF.389-393.985.
[115] A.B. Renz, O.J. Vavasour, P.M. Gammon, F. Li, T. Dai, M. Antoniou, G.W.C. Baker, E. Bashar, N.E. Grant, J.D. Murphy, P.A. Mawby, V.A. Shah, The improvement of atomic layer deposited SiO_2/4H-SiC interfaces via a high temperature forming gas anneal, Materials Science in Semiconductor Processing 122 (2021) 105527. https://doi.org/10.1016/j.mssp.2020.105527.
[116] K. Fukuda, S. Suzuki, T. Tanaka, K. Arai, Reduction of interface-state density in 4H–SiC n-type metal–oxide–semiconductor structures using high-temperature hydrogen annealing, Applied Physics Letters 76 (2000) 1585–1587. https://doi.org/10.1063/1.126103.
[117] A. Gölz, G. Lucovsky, K. Koh, D. Wolfe, H. Niimi, H. Kurz, Plasma-assisted formation of low defect density SiC–SiO_2 interfaces, Journal of Vacuum Science & Technology B: Microelectronics and Nanometer Structures Processing, Measurement, and Phenomena 15 (1997) 1097–1104. https://doi.org/10.1116/1.589420.

[118] D.H. Yoon, I.E. Reimanis, A review on the joining of SiC for high-temperature applications, Journal of the Korean Ceramic Society 57 (2020) 246–270. https://doi.org/10.1007/s43207-020-00021-4.
[119] J.R. McDermid, M.D. Pugh, R.A.L. Drew, The interaction of reaction-bonded silicon carbide and inconel 600 with a nickel-based brazing alloy, Metall Trans A 20 (1989) 1803–1810. https://doi.org/10.1007/BF02663211.
[120] P. Wan, M. Li, K. Xu, H. Wu, K. Chang, X. Zhou, X. Ding, Z. Huang, H. Zong, Q. Huang, Seamless joining of silicon carbide ceramics through an sacrificial interlayer of $Dy_3Si_2C_2$, Journal of the European Ceramic Society 39 (2019) 5457–5462. https://doi.org/10.1016/j.jeurceramsoc.2019.09.002.
[121] X. Zhou, J. Liu, S. Zou, K. Xu, K. Chang, P. Li, F. Huang, Z. Huang, Q. Huang, Almost seamless joining of SiC using an in-situ reaction transition phase of $Y_3Si_2C_2$, Journal of the European Ceramic Society 40 (2020) 259–266. https://doi.org/10.1016/j.jeurceramsoc.2019.10.016.
[122] J. Xu, P. Tatarko, L. Chen, X. Shan, Q. Huang, X. Zhou, High-strength SiC joints fabricated at a low-temperature of 1400°C using a novel low activation filler of Praseodymium, Journal of the American Ceramic Society n/a (n.d.). https://doi.org/10.1111/jace.19229.
[123] L.K. Shi, X. Zhou, K. Xu, K. Chang, J.Q. Dai, Z. Huang, Q. Huang, Low temperature seamless joining of SiC using a Ytterbium film, Journal of the European Ceramic Society 41 (2021) 7507–7515. https://doi.org/10.1016/j.jeurceramsoc.2021.08.057.
[124] K. Xu, H. Zou, K. Chang, Z. Deng, X. Zhou, Y. Huang, L. Chen, F. Huang, Q. Huang, Thermodynamic description of the sintering aid system in silicon carbide ceramics with the addition of yttrium, Journal of the European Ceramic Society 39 (2019) 4510–4519. https://doi.org/10.1016/j.jeurceramsoc.2019.07.012.
[125] K. Xu, L. Chen, K. Chang, P. Wan, M. Li, Z. Deng, F. Huang, Q. Huang, Thermodynamic description of the Dy–Si–C system in silicon carbide ceramics, Calphad 68 (2020) 101738. https://doi.org/10.1016/j.calphad.2020.101738.